Core Restraint and Seismic Analysis of a Large Heterogeneous Free-Flowering Core Design

NP-1615
Research Project 620-25

Final Report, November 1980
Work Completed, June 1980

Prepared by

ARGONNE NATIONAL LABORATORY
Components Technology Division
9700 South Cass Avenue
Argonne, Illinois 60439

Principal Investigators
J. T. Madell
T. J. Moran
J. E. Ash
P. J. Fulford

Prepared for

Electric Power Research Institute
3412 Hillview Avenue
Palo Alto, California 94304

EPRI Project Manager
R. K. Winkleblack

Developing Applications and Technology Program
Nuclear Power Division

ORDERING INFORMATION

Requests for copies of this report should be directed to Research Reports Center (RRC), Box 50490, Palo Alto, CA 94303, (415) 965-4081. There is no charge for reports requested by EPRI member utilities and affiliates, contributing nonmembers, U.S. utility associations, U.S. government agencies (federal, state, and local), media, and foreign organizations with which EPRI has an information exchange agreement. On request, RRC will send a catalog of EPRI reports.

NOTICE

Prepared by
Argonne National Laboratory
Argonne, Illinois

EPRI PERSPECTIVE

PROJECT DESCRIPTION

Two major requirements of a core of a large liquid metal fast breeder reactor (LMFBR) power plant should be that: (1) the component of reactivity caused by bowing of the fuel and blanket subassemblies is tolerably small, i.e., not too large a positive reactivity effect, and (2) seismic forces during the maximum design earthquake do not result in core compaction that increases reactivity of the core beyond a tolerable level. Other major requirements of a core which is significantly affected by bowing and seismic excitation are the limitations of the force levels on load pads and of the top-end misalignment of control rods with drive lines. The analysis reported herein under RP620-25 is an early iteration to start toward a clear understanding of bowing and seismic response of large breeder cores.

The analysis is of a "free-flowering" concept, which is said to be different than the "limited-free bow." As used in the report, "free flowering" means that there are no restraint rings around the outside of the rows of removable reflector-shield subassemblies surrounding the radial blanket. There are such rings in the "limited-free bow" concept. Both concepts use two load pads as parts of the fuel and blanket subassemblies. These load pads limit compaction of the cluster of subassemblies when they touch and also influence the bowing of each subassembly. The stiffness of the subassemblies, and particularly the stiffness of the removable reflector-shield subassemblies, restrain the core blanket complex in the "free-flowering" concept. The same is true of the "limited-free bow," but the outside restrainer rings are one more factor. Actually, tolerances and allowances on hardware dimensions and gaps become important variables in both concepts.

PROJECT OBJECTIVES

The objective of this analysis is to assess the behavior of a large LMFBR core, regarding the net reactivity effect of the different bowings that will occur in the large number of individual fuel and blanket subassemblies. These subassemblies make up the total core and blanket assembly of a "low-energetics breeder

core," in which low energetics is approached by strategic placement of internal blanket subassemblies among the fuel subassemblies. The force levels on the load pads and the top-end misalignments are to be assessed. Also, the analysis is to assess the behavior of the core and blanket during an earthquake and see what reactivity effects can be expected.

PROJECT RESULTS

The core that was analyzed is a practical one. However, detailed drawings for the hardware were not available during the early stages of the analysis. As is normal practice, the numerical design and the hardware drawings are iterated as a core and blanket develops. The core that was analyzed is not engineered in final form, but it is sufficiently representative to give confidence that a low-energetics core and blanket can be built and operated safely. Bowing will contribute some small positive components to the overall power coefficient of reactivity, but the total coefficient will be negative over the power range. Seismic forces complicate the situation and introduce more uncertainties, but the indications are that a core and blanket can be designed which will behave satisfactorily.

This work will be of interest to analysts and designers of LMFBR cores.

R. K. Winkleblack, Project Manager
Nuclear Power Division

ABSTRACT

The core restraint and seismic performance of a large heterogeneous core was analyzed. A free-flowering core restraint system was selected for this study, as opposed to the limited-free bow system of the FFTF and CRBRP. The key features of the core restraint system, such as stiff reflector assemblies and load pad properties, were specified in this study. Other features--such as the fuel-assembly description, flux and temperature distributions, and clearances between the assembly nozzle and grid plate--were obtained from the other parts of a large, heterogeneous Core Study 11 and 12. Core restraint analysis was performed with NUBOW-3D over the first two cycles of operation. The SCRAP code was used to analyze the time-history seismic response of the core with the effects of fluid, impact, and bowed assemblies modeled in the code. The core restraint system design was assessed in terms of the predicted forces, impacts, displacements, and reactivity effects for different cycle times and power/flow ratios.

ACKNOWLEDGMENTS

The authors wish to thank the Electric Power Research Institute for their support of this study. The consultation of G. A. McLennan on the mysteries of the NUBOW-3D code was essential to the successful completion of the analysis. The valuable assistance of M. Shackelford in coordinating the overall effort, Science Applications, Inc., in providing core design data, and E. Hutter for his comments on mechanical design were greatly appreciated. We also express our thanks to Carolyn Dueweke for deciphering a variety of handwritings and converting them into a presentable document.

CONTENTS

ILLUSTRATIONS

TABLES

I. SUMMARY

This report contains the analysis and assessment of the core restraint and seismic performance of a large heterogeneous core. A free-flowering core restraint system design was chosen for the study. The key features of the design are long assembly inlet nozzles and stiff reflector assemblies surrounding the core. The long inlet nozzle sits in the grid plate with small alterla clearances which permit a very small rotation of the assembly. The stiff reflector assemblies resist the lateral displacement of the fuel and blanket assemblies which deform due to temperature and fluence gradients. The reflector assemblies are designed sufficiently stiff to produce stresses in the restrained fuel and blanket assemblies which are then relaxed by irradiation creèp, placing an upper limit on the deformation of core assemblies.

Even though this and companion work 11 and 12 represent an extensive core design effort, additional details are still needed for a final core restraint and seismic analysis. Examples of data that were not available for this current analysis include the top-end misalignment requirements imposed by the control rod drive-line and by the refueling mechanism, time-history motion of the core support structure, manufacturing tolerances of the load pads, duct wall temperatures for the first several operating cycles (including the effect of interassembly heat transfer) and allowable impact on assembly load pads. In lieu of these data, values for misalignment requirements were assumed, sensitivity to the frequency and magnitude of support motion was investigated, generic affect of tolerances were studied and duct wall temperatures after the beginning of life were approximated. The acceptability of impact loads awaits detailed structural analysis and a study of material properties.

The core restraint calculations were performed with NUBOW-3D, which is now the standard core restraint code in the U.S. The three-dimensional analysis of

the core restraint performance, which is the first published on a large heterogeneous core with a free-flowering core restraint system, was carried out for the first two cycles of operation. The forces and displacement of assemblies in a 30° sector of the core were calculated at 10 day intervals and the reactivity level was obtained at the beginning and end of the two cycles. The major results on the performance are, (1) the top-end displacements fall within the values used in U.S. designs (e.g. CRBRP), (2) the bowing coefficient is quite small, although positive. The overall power coefficient is predicted to be negative over most or all of the power range, (3) the forces during refueling are acceptable, and (4) the forces during operation may be higher than desirable. Either detailed structural analysis should be performed on the load pad design or duct wall temperature calculations should be improved to reduce the conservatively high values of the temperature gradients.

The core restraint analyses also identified the key features of the system as, (1) stiff reflector assemblies and relatively flexible fuel and blanket assemblies, (2) the load pads with a stiffness between those of the thick full-circumferential design and the button spacer extruded from the duct wall, and (3) allowable top-end misalignments at least as great as the values used in other U.S. designs.

The SCRAP code, which has been developed at ANL for the last four years, was used to investigate the seismic response of the core. The performance quantities of displacement, bending stress, and impact load were calculated for a core arrangement of 17 clusters, excited by a 6 Hz, 1.0 g support motion. Additionally, the sensitivity of the performance quantities to the type of support motion and the models in the SCRAP codes were determined. An analysis was also performed for a narrow band support motion. The seismic study concluded that a free-flowering core restraint system can be designed to withstand seismic disturbances provided that, (1) the support motion has a peak acceleration no more than 1.0 g and little frequency content below 5 Hz, (2) the misalignment between a control rod drive-line and the control assembly can be as large as 25 mm (1 in) during a seismic event, (3) bending stresses can be as large as 50 MPa (7.24 ksi) and, (4) assemblies can withstand impacts with peak impacts of 50 kN (11,250 lb) on soft load pads and 200 kN (45,000 lb) on hard load pads.

1.0 INTRODUCTION

The purpose of this report is to present the core restraint and seismic analysis of a large heterogeneous LMFBR core of the "free-flowering" type of design and to assess the design in terms of its calculated performance. Core restraint analysis consists of determining the mechnical equilibrium forces and displacements in the core system due to assembly interaction during normal operation. Quantities of particular interest in this analysis are the forces at the load pad and nozzle contact points during power operation, the total lateral forces during refueling, top-end misalignment of control assemblies during power operation and of all assemblies during refueling, and the radial structural component of the power reactivity coefficient. The core seismic analysis predicts the assembly response to the core support structure motion. The analysis provides time histories of displacements, bending stresses, and impact forces at various locations on the assemblies, and the sensitivity of these quantities to the characteristics of the support motion and the modeling assumptions. The core restraint and seismic analyses are in concert with the neutronic, thermal hydraulic and other mechanical analysis of the same large heterogeneous core reported in the other voluems.

The report deals exclusively with the "free-flowering" design of a core restraint system. In this type of core restraint system, there is no core restraint ring or other lateral support at the core periphery. The inlet nozzle of the assemblies are long with little lateral clearance to the grid plate support. Because the nozzle fits so tightly in the grid plate the top end of the assembly can rotate freely (without contact at the nozzle) only a short distance, about 1 mm from one side to the other. Some lateral support is provided by very stiff reflector assemblies surrounding the radial blanket.

The essential feature of this core restraint system concept is the stiff reflector assemblies. Assembly bowing, due to temperature and fluence gradients, result in the displacement of the assemblies. Without some lateral restraint, the assembly displacement would produce unacceptable misalignments well before the assemblies reached their desired lifetime. Unacceptable misalignments are avoided

by some form of lateral restraint. In the "limited-free-bow" approach, rigid restraint rings are placed at the core boundary to limit the maximum displacements at the top-end and above-core load pads. In this approach, the reflector assemblies are made as stiff as the core design features will allow; that is, with a specified outer duct dimension the duct wall thickness and the nozzle outer diameter and wall thickness are chosen as large as possible. The reflector assemblies are also designed for as small as practical radial temperature gradient and for no reversal in the gradient which would produce a "buggy-spring" effect. Further study is needed to achieve the design details for the reflectors and to determine whether the reflector deformation during the reactor lifetime would require replacement.

There is some experience with the free-flowering core restraint system. EBR-II and Phenix were designed and operated well with "loosely" cantilevered assemblies in a grid plate and without any lateral support at the core periphery. The EBR-II operation does not provide information on the performance of high fluence cores in which swelling distortion may adversely affect the core restraint performance. Phenix has operated to moderate burn-up ($\sim$65 to 70 $\frac{\text{MWd}}{\text{kg}}$) and satisfied the core restraint requirements. A concern has been expressed that higher fluence on the reference duct alloy may result in unacceptable top-end bowing for refueling. The Creys-Malville Reactor (Super Phenix) will also employ the free-flowering concept, but details of the design have not been received. A core seismic analysis has not been published for any of these reactors.

The Components Technology Division at ANL previously conducted a conceptual design study on a free-flowering restraint system for a 1200 MWe LMFBR homogeneous core[1]. The study concluded that the design met the requirements regarding static-force displacements and reactivity effects. To satisfy the requirements on top-end deflection for the outermost fuel assemblies, the reflector assemblies were made as stiff as possible. In this design, irradiation creep dominates the swelling-induced bowing effect. As the outer fuel assemblies bow (due to differential swelling) against the blanket assemblies, which in turn transmit the load radially to the stiff reflector assemblies, stresses build up in the assembly duct walls because the reflector assemblies resist the outward bowing of the fuel assemblies. Irradiation creep limits the bowing by relaxing the bending stresses in the duct wall. Thus, a free-flowering core restraint system was found to be feasible in principle but attention must be given to particular design features. Although the

seismic response of such a core restraint system was of concern, no analytical tools were available at that time to investigate the topic.

The core design studied here differs in some features from that on which previous detailed core restraint analysis had been performed. An important feature is that the core is arranged in a heterogeneous configuration. A heterogeneous core with internal blankets is expected to exhibit a pattern of assembly interaction considerably different from that typically seen in homogeneous cores.

First, the magnitude of the flux and temperature gradients are greater in a heterogeneous core than in a homogeneous one. The flux is much greater in a fuel assembly than in an internal blanket; thus, sharp flux gradients occur across the boundary of a fuel-internal blanket region that do not occur in a homogeneous core except around control assemblies and at interfaces between the core and radial blanket. Likewise, large temperature gradients occur where a fuel assembly is adjacent to a fresh internal blanket assembly. In addition to larger gradients in a heterogeneous core, the sign of the gradients change with radial location, from a fuel region to an internal blanket region and then back to a fuel region.

Greater assembly interaction is therefore expected because of the greater number of gradients, the large values of the gradients, and the opposing signs of the gradients within the core. This pattern was calculated in a preliminary analysis of the core restraint performance for the Large Heterogeneous Reference Core Study (LHRCS)[2]. The core restraint system in this study employed the "limited-free-bow" concept, similar to that of the CRBRP and FFTF. Although the analysis was confined to 2-D calculations (a considerable limitation), the amount of interaction between assemblies was found to be greater than typically found in homogeneous designs. Sufficient information on the temperature and flux environment in the core was not available so no quantitative results on the core restraint performance of the heterogeneous core were reported. However, the study showed qualitatively that the larger and more interactive gradients produce poorer core restraint performance for the case of a "limited-free-bow" concept.

Core restraint and seismic analyses require a great deal of design information about the core. The core map, fuel management scheme, the geometrical and mechanical description of the various assembly types and, if they exist, the dimensions and mechanical properties of the core restraint rings must be defined. In addition, flux and temperature data must be specified for the six faces of the assembly ducts at several elevations. The reactivity effect due to radial movement

must be given for the various axial sections of each assembly.

The data used in this study were either developed in the course of the core restraint and seismic analysis or obtained from the analysis reported in the other volumes of the Large Heterogeneous Core Study. In the early stages of this study the dimensions and configuration of the core components were identical in all parts of the study. As the design analyses proceeded some minor differences arose. For example, only stiff reflectors are considered here, while a stiff and a flexible design are presented in "Reactor Core Design"[12]. The nozzle portion is slightly shorter in this analysis than the Reactor Core Design study. Small differences also exist due to the use of the metric system here and the English system elsewhere. For example, the across-flats dimension of 144 mm is not quite identical to 5.682". These differences in the design are, however, not significant to the results of the core restraint and seismic analysis.

Extensive neutronic analysis was performed on the core layout and some fuel management schemes were investigated. Some of the dimensions of the assemblies were established by both neutronic and mechanical calculations. Individual assembly and core-wide thermal-hydraulic analyses were also performed. Most of the input data and the design information on which the data are based (e.g. the assembly stiffness) can be found in the reports 11 and 12 on the nuclear and assembly design report. Design data sufficient to describe the core restraint system and its analysis are contained herein.

The core map for the study is identical to that analyzed in the core neutronic report[11]. The fuel management scheme consists of a one-third reload, which was adopted in the neutronic study but the selection of the specific assemblies was done by the core restraint analysts prior to its availability from the neutronic analysis volume. The mechanical description of the core and axial blanket regions was taken from the neutronic and thermal-hydraulic study[11] The design features above and below the axial blanket regions were established by the core restraint and seismic analysts with the consultation of EBR-II staff. The mechanical properties of the full length of the reflector assemblies are specified in this study and are also discussed in the "Reactore Core Design " report 12. The values of the flux were first calculated in the neutronic analysis, and then converted into the quantities (i.e., fast flux at the mid-wall of each duct face) used for NUBOW-3D input. Beginning of life (B01C) mid-wall duct temperatures were provided by the thermal-hydraulic [11] study. The duct wall temperatures at other times (i.e., E01C, B02C, ..., E04C) were

obtained with an algorithm which relates the change in the mean outlet coolant temperatures of two adjacent assemblies to the change of the duct wall temperatures in the neighboring faces of the two assemblies. Since these temperatures are based on those from the thermal-hydraulic analysis,[11] they also overpredict the duct gradients by neglecting the heat transfer across the gap. The reactivity values for radial movement of the assemblies was calculated as part of the nuclear analysis, using a method prescribed by the authors of this volume.

As stated earlier in the Introduction, one of the objectives of the study is to assess the design in terms of the calculated performance. To meet this objective, criteria must be established. The criteria fall into three categories: forces, displacements, and start-up reactivity effects.

The forces must be sufficiently low so load pads are not crushed, the bending stresses must be acceptably low, and the frictional force during refueling operations must permit withdrawal and insertion of assemblies. The displacements must not produce misalignments that exceed those prescribed by the control-rod drive system and the refueling mechanism. The "bowing" reactivity change during start-up must result in a generally negative power coefficient or at worst slightly positive at low power/flow ratios, so that the control system can easily and safely bring the reactor to full power. To permit an assessment of the design, acceptable values will be given for the forces, displacements, and "bowing" reactivity in subsequent sections after the results of the analysis have been presented. These values are qualitative and "semi-quantitative" based on experience with other designs.

The core restraint portion of the study is presented in Chapter II and the core seismic in Chapter III. Each chapter contains all aspects of the work. The computer code is explained, the pertinent features of the core restraint system are described, the scope of the analysis is presented, the results are given in tables and figures, and the design is assessed in terms of this part of the system performance.

2.0 CORE RESTRAINT ANALYSIS

2.1 THE NUBOW-3D COMPUTER CODE

The time history of core deformations resulting from thermal expansions and irradiation swelling were analyzed with the NUBOW-3D computer code[4]. The core geometry and material properties, including temperature and irradiation dependence, provide the basic input to the code. Temperature and flux distributions were specified, including time variations of the temperatures. The computer program calculates the mechanical equilibrium response of the system to the forces induced by the temperature and fluence gradients. The response is expressed in terms of displacements and forces. Associated with displacements, reactivity changes are computed; and associated with the forces, stresses are computed. The temperature is allowed to vary with time, and under this influence, together with the cumulative effects of irradiation-induced swelling and irradiation-enhanced creep, the core mechanical response will change with time.

The overall development of the NUBOW codes has been supported by DOE for about five years. The DOE program consisted of the development of three codes, NUBOW-2D which solves the "spoke" or 2-D problem, PARABOW which can use information supplied by the user to take into account some 3-D and other effects, and NUBOW-3D which solves the mechanical equilibrium among the assemblies in a sector (typically a 30° sector) of a core. Since NUBOW-3D was used exclusively in this study, the following comments are intended for NUBOW-3D although many statements can be applied to all codes. The development effort has consisted of the formulation, writing and placing the code into operation in March 1978. A verification effort was carried out during this time period, in which NUBOW-3D results were found to agree well with hand calculations for simple cases and with ANSYS, CRAMP (a UK code) and DDT (a German code) for cases similar to a small reactor core. NUBOW-3D also agreed inside a very broad band of experimental uncertainties with the results from Core Restraint Test Facility and deformation measurements of EBR-II reflectors. The code has been exported to all fast reactor contractors (AI, CE, GE, GA, HEDL, and WARD) and is being used in the analysis of the FFTF, CRBRP, CDS and GCFR-300.

Because of symmetry considerations, only a 30° sector of the assembly configuration, as shown in Fig. 2.1, is required in the computer model. The outer dimensions are identical for all assemblies as shown in Fig. 2.2. However, because the wall thickness differs, there are three mechanically distinct duct types. The fuel and blanket assemblies are mechanically identical and constitute one type (see axial cross-section, Fig. 2.3). The control assemblies constitute a second type, and differ from the first type in that there is no shielding section at the top, which would interfere with the motion of the control rods (compare Figs. 2.3 and 2.4). The reflector assemblies, shown in Fig. 2.5, constitute the third type. These assemblies are very rigid, made of solid steel sections with coolant passages, and provide a stiff outer mechanical restraint.

Each assembly is treated individually in the computer code as a beam-theory model allowing bending in two planes (x-z and y-z); axial variations in beam properties and environment are considered for each assembly. There are 23 numbered locations, called nodes, along the axial direction (see Fig. 2.2) which partition the assembly beam into geometrical segments. The segment between nodes (1) and (2) is a circular nozzle. The above-core-load-pad (ACLP) is at node (19), and the top-load-pad (TLP) is at node (23). The assembly is treated as a beam which can have external loads applied at these four locations. There is no clearance at the top of the nozzle (node 2), at which location the beam may be conceived as "pivoted", while clearances may exist at the other three locations. The cross-sections at the load pads are hexagonal, and the forces may vary over the six faces at these locations. The six mid-flat temperatures are provided at four axial locations: the bottom of the core (node 6); the core mid-plane (node 11); the top of the core (node 16); and the top of the upper blanket (node 20). The temperature is assumed to vary linearly between these specified axial locations. Also, at a given axial location, the temperature may vary circumferentially form mid-flat to mid-flat about the six faces. The axial locations also define segments of differing gecmetric properties. For example, for the fuel assembly, nodes (1) to (2) define the circular nozzle segment; node (2) to (3) the heavy, thick-walled lower shield section, with a high beam moment-of-inertia; nodes (3) to (6) the lower blanket; nodes (6) to (16) the core region; nodes (16) to (20) the upper blanket; nodes (20) to (21) the fission gas plenum; and another heavy shield section is included between nodes (21) and (23). Each of the 23 locations is a "strain node" in the sense that at each node the irradiation flux is specified, and the strains due to creep and swelling are computed in these sections as described in Ref. 4.

A representative sample of the computer output data is shown in Tables 2.1, 2 and 3. A brief description of this output will indicate the general computational approach. Greater detail may be found in Ref. 4. In Table 2.1, duct displacements and clearances with adjacent ducts are shown at the four load-point levels. (Refer to Figs. 2.1 and 2.2). Table 2.1 includes data for ducts (1) through (10) only; however, all 90 ducts are listed in the computer output. (Note in Fig. 2.1 that ducts (17), (19), (34), and (48) are fictitious ducts and are included only for convenience in generating the duct matrix). The equilibrium computations occur at discrete time steps, in general at 10-day intervals. Table 2.1 shows Step 28 at a time of 127.5 days from beginning-of-life (BOL). (This is at "half cycle" for a refueling time interval of 255 days). The values of VTX and VTY are the full-power, thermal bow displacements at the four levels for a conceptually unconstrained isolated duct in the X and Y directions, respectively. (See Fig. 2.1). The values of VPX and VPY are due to the total creep and swelling that have occurred up to this time. The values of DEL(1) through DEL(6) are the hypothetical "clearances" that would occur between imaginary neighboring ducts at the six faces. The faces are counted in the clockwise direction in Fig. 2.1, starting from the top face. Negative values would indicate an overlap or "interference" with the neighboring duct. Since this is physically impossible, the two interfering faces must be in contact, exerting equal and opposite reaction forces. An iterative force equilibrium computation is then initiated and the resulting configuration is shown in Table 2.2. The values of F1 through F6 are the resultant equilibrium forces on the six faces, and VX and VY are the resultant displacements. The values of RX and RY are the residual numerical errors when the iteration is considered to have converged sufficiently. Hence, the values in Table 2.1 describe the "prebowed" shape, with zero forces, and the values in Table 2.2 give the constrained equilibrium configuration. Associated with the changes in the core sections of the duct, reactivity changes take place. The reactivity change DK(J) for each duct is shown in the even-numbered columns of Table 2.3. The number, WJ(J), in the odd-numbered columns, is the structural reactivity worth for the J-th duct.

2.2 THE COMPUTATIONAL RESULTS

The computation started with all fresh assemblies (BOL) and was repeated at 10-day intervals over a period of 255 days. Two temperature distributions were specified as input data, one for the beginning and the other for the end of this

first cycle period. At each of the intermediate 10-day interval times, the input temperature distribution was determined from a linear interpolation between the beginning and end distributions. An equilibrium computation at full power was made over the period of 255 days, and at certain times a computation with the time fixed was made for a power ramp ranging from full to zero power. At completion of the first cycle, a second fuel cycle of 255 days was started. For this second fuel cycle computation, two new sets of temperature distributions at the beginning and end of cycle were specified. One-third of the fuel and inner blanket assemblies were replaced. Equilibrium computations at full power were again performed at 10-day intervals with linearly interpolated temperature distributions. Power ramp computations were then performed at selected times.

2.2.1 The Full-Power Life Computation

For the design summarized in Figs. 2.1-4, an equilibrium computation for two cycles at full power was made. After 255 days, a refueling was assumed at which time ducts 3, 5, 8, 10, 20, 28, 36, 39, 41, 43, 50, 53, 55, 62, 72, and 74 were replaced with fresh assemblies. Starting with all fresh assemblies (BOL), equilibrium computations were made at 10-day intervals to the completion of this first fuel cycle. The results of this computation are summarized in Tables 2.4-7.

2.2.1.1 Duct Displacements at Beginning of Life (BOL)

Table 2.4 shows the displacements, temperatures, loads, and stresses at the beginning of life under full load conditions. Table 2.4(a) shows the unconstrained thermal bow displacements at the two load-pad positions, the above-core-load-pad (ACLP) and the top-load-pad (TLP). The ten ducts with the highest and the ten with the lowest thermal bows are tabulated. For example, duct (29) has the highest thermal bow, 4.4 mm at the ACLP and 34.8 mm at the TLP. The direction of the displacement is 94° measured clockwise from the positive Y-axis. The final constrained equilibrium displacements are listed under "Total Displacements". Note that for duct (29) the displacement at the TLP has been reduced from the unconstrained thermal bow of 34.8 mm to a value of 22.8 mm. For the ACLP, duct (69) now has the maximum displacement of 4.9 mm, in a direction 109° measured counterclockwise from the positive Y-axis. At the TLP, duct (66) has a maximum displacement of 24.5 mm. The displacement configuration at the ACLP is shown in Fig. 2.6 and at the TLP in Fig. 2.7. Note that the scale at the ACLP is magnified by a factor of 10 greater than the scale factor at the TLP; i.e., the reference gap

scale is 2 mm at the ACLP, and the gap scale is 20 mm at the TLP. It should be emphasized that Figs. 2.6 and 7 show the scaled displacements (arrows) and clearances, and that the hexagonal shapes are not scaled and simply indicate the relative locations of the duct centers. Comparisons of the maximum displacements listed in Table 2.4 with Fig. 2.7 (see also Fig. 2.1 for the duct numbering system) show that the greatest displacements at the ACLP are directed outward for the outer three rows of ducts, i.e., the two reflector rows and the outermost row of blankets. Examination of the ACLP displacement pattern shown in Fig. 2.6 reveals that one row of blanket ducts (labeled 'B') tend to separate from its neighboring row of blanket ducts. On the other hand, fuel ducts (labeled 'C') in neighboring rows tend to compress at the ACLP. The intensity of the contact force at each face is indicated by the black area scaled to the maximum contact force in the system over the lifetime of interest. This general behavior is explained by reference to the schematic diagram, Fig. 2.8, which pictures two fuel assemblies in adjacent rows. It is assumed that the assemblies in- and out-board of the two fuel assemblies are low power assemblies so the flux and, in turn, the power and temperature distributions peak approximately between the two fuel assemblies. Under the action of the resultant thermal gradients, the hotter surfaces will cause the fuel assembly ducts to bow together at the ACLP and separate at the TLP as shown (much exaggerated) in the diagram. The opposite behavior can be expected for two cooler blanket assemblies when they are in between fuel assemblies. The thermal gradients across the pair of blanket ducts shown in the diagram will be opposite to the gradients for the fuel duct pair, and the resulting thermal bows will now be directed so that separation occurs at the ACLP, and the TLP faces are drawn together. This is the exact behavior observed in Figs. 2.6 and 7. At the ACLP, (Fig. 2.6) the blanket (B) ducts tend to separate, and at the TLP, (Fig. 2.7) the fuel (C) ducts tend to separate.

Table 2.4(a) shows the hottest ducts (about 880°F) to be in the outer core region, and the coldest ducts are the outer two rows of reflectors (about 600°F). Thus, the greatest thermal gradients occur at the outer core region, and consequently the greatest displacements are observed in Fig. 2.6 for those ducts out-board of the separation between the outer blankets, and in Fig. 2.7 for those ducts out-board of the separation between the outer fuel ducts.

2.2.1.2 Duct Loads at BOL

The greatest and lightest loads on the ducts are shown in Table 2.4(b). The loads occur at four levels: the nozzle tip, the nozzle base, the ACLP, and the

TLP. There is zero clearance at the nozzle base, which is referred to as the "pivot" point for the duct considered as a bending beam. The forces are all normal to the contact surfaces. The nozzle is circular, and the resultant force is in the direction of the resultant displacement. At the ACLP and TLP, forces can act at each of the six faces (numbered clockwise in Fig. 2.1, starting with the top face). The algebraic sum of the six face-force gives total normal force magnitudes at the ACLP and the TLP, and are listed in Table 2.4(b). The algebraic sum of these force magnitudes at the four levels gives the total lateral force magnitude. For example, the heaviest lateral load is exerted on duct (35). A relatively light load of 753 N is exerted at the nozzle tip, the loads at the pivot and TLP are about the same, 4016 N and 4401 N, respectively. By far, the highest load is 17494 N at the ACLP. The sum of these four forces, gives a total lateral force of 26663 N (or about 6000 lb). Note that this is the lateral force at full power; the force will drop to zero at no power as shown in Fig. 2.9. The lateral force multiplied by some coefficient of friction will represent the frictional resistance to withdrawal of the duct. Of course, the duct will be withdrawn when the reactor is not in operation, so that at the beginning of life the friction force will be zero and only the weight of the duct need be considered. However, later in life, because of permanent residual strains, an appreciable lateral force may exist at a zero power condition.

The total lateral load is of interest chiefly with regard to duct withdrawal. The individual force components acting on the faces of the hexagonal sections are also of interest with regard to the resulting strain on the load pad. Each surface of a load pad is assumed to behave as a simple linear spring, with a stiffness defined by a representative spring constant (see Figs. 2.2, 3 and 4) which is independent of the load condition at the other five faces. The individual faces with the highest and lowest loads are listed in Table 2.4(b). For example, the maximum interfacial load occurs between ducts (52) and (53); face (1) of duct (52) is in contact with face (4) of duct (53), and a mutual force of 5287 N is exerted. Tabulated under the heading "Lightest Loads" are zero forces, which indicate faces that are not in contact.

2.2.1.3 Duct Bending Stresses at BOL

The highest and lowest bending stresses at the outer surface are listed in Table 2.4(c). The bending moments at the nozzle tip and at the TLP are zero, so there are no bending stresses at these sections. Bending stresses occur at the

nozzle base ("pivot point" of the duct) and at the ACLP. In general, the bending stresses at the ACLP are much higher than at the nozzle. Tensile stresses are positive and compressive stresses negative. Outer surface stresses at the corner and at the mid-flat of the hexagonal cross-section are listed. The highest stress is a tensile stress of 131 PMa at the corner of the ACLP section of duct (20). The maximum mid-flat stresses occur at ducts (9), (35), and (52) of the order of 106 MPa; the stresses for ducts (9) and (52) are tensile, and the stress for duct (35) is compressive. These may be considered to be fairly high stresses (about 19,000 psi), but as life progresses, as shown in Fig. 2.10, these stresses are relieved due to creep relaxation.

2.2.1.4 Displacements at End of First Fuel Cycle

The summary of full power output data at the end of the first fuel cycle (255 days) is shown in Table 2.5 and can be compared to the data at the beginning of life. The dominant influence is the irradiation-enhanced creep which allows relaxation of the thermal stresses so that the duct bowing is reduced. The reduction of the maximum bending stresses with time is shown in Fig. 2.8. The high maximum stress of 131 MPa (in duct 20) drops off rather rapidly to about a 25 MPa maximum stress (in duct 52) after 255 days. The associated maximum forces also diminish, as shown in Fig. 2.11 from about 26600 N (duct 35) to about 6600 N (duct 50).

The relaxed displacement configuration is shown in Figs. 2.12 and 13. Comparison with the fully bowed configuration at BOL shows that at the ACLP the outer core, which was significantly displaced outward with a prominent separation at the internal blanket row, has returned to a much less bowed configuration. We see in Fig. 2.14 that the maximum ACLP displacement of about 5 mm has been reduced to about 2 mm, less than half the BOL value. The force levels at which the fuel assemblies contact each other have also been significantly relieved, as may be observed by the reduction in the size of the black area scaled to the maximum force intensities during the cycle. Hence, although the outer core as a cluster of fuel assemblies has been displaced inward, the net reactivity has diminished, as shown in Fig. 2.15 because the individual fuel assemblies are not squeezed as tightly together against their neighbors as at the beginning of life. The reactivity has dropped from about +7 cents at BOL to about +1.5 cents at 255 days.

2.2.1.5 Summary of Output Data at Beginning of Second Fuel Cycle

At the end of the first fuel cycle, roughly one-third of the fuel and blanket assemblies are replaced. When the reactor is brought up to full power again, a discontinuity in the performance data occurs. For example, in Fig. 2.15, the reactivity drops from about +1.5 cents to about -1.25 cents. The reactivity then begins to rise with the passage of time because of the delayed influence of irradiation swelling caused by the flux accumulation.

It is informative to compare the reactivity curve of Fig. 2.15 with an earlier computation shown in Fig. 2.16. In this earlier computation, the initial values of the temperature distribution inputted to the computer code were maintained constant, rather than permitted to vary with the passage of time as is the results presented so far. The more realistic case in which the temperatures vary, results in diminishing temperature gradients, and since the temperature gradients provide the driving force for the thermal bowing, the effect should be to reduce the reactivity. However, if the two reactivity curves are superimposed, we see in fact that the curve for the case with reduced temperature gradients with time does not fall more sharply than the curve for the case with the fixed temperature distribution. The reason is that changes in the stress due to the creep relaxation have a more significant effect upon the bowing than the changes in stress due to the thermal gradients. That is, the reduced thermal stresses, and associated reduced forces, result in less creep. Hence, the greater creep rate for the constant temperature case actually causes a greater drop in the reactivity during the first 255 day fuel cycle, i.e., a reduction in the compaction of the core.

At the end of the first cycle approximately one-third of the fuel and one-third of the internal blanket assemblies were replaced with new assemblies. The specific numbers are given in Fig. 2.15. Under full power conditions the refueling at 255 days results in a core with greater average assembly bow, because the thermal bow of the "old" assemblies had been reduced by irradiation-induced creep. The "new" assemblies are scattered through the fuel-internal blanket region in a somewhat arbitrary scheme. This particular replacement pattern resulted in moving the higher worth fuel assemblies into less reactive locations, probably by increasing on the average the size of the interassembly gap at the elevation of the fissile zone. It is believed tha another replacement pattern could be devised which would increase the reactivity level rather than decrease it. To take the point to the extreme, one can see that replacing all of the fuel and

internal blanket assemblies would increase the reactivity level from +1.4 cents to 7.2 cents, i.e., the value at time = 0. This topic is discussed further in the presentation of the displacement data below.

During the second cycle the increase in reactivity level is the result of the core compaction due to irradiation swelling-induced bowing of the fuel and blanket assemblies. The bowing force mechanism is similar to that produced by the unequal thermal expansions caused by the temperature gradients. As time and, consequently, fluence increases, the amount of bowing increases. The effect of swelling bow is the same as that described above for thermal bow. Thus, the fuel assemblies contact at the ACLP and the reactivity level increases. This behavior is seen in the reactivity curve between 255 days and 550 days in Fig. 2.15.

The summary of full power output data at the beginning of the second fuel cycle (255 days) is shown in Table 2.6. We see that the maximum stresses (Fig. 2.10), forces (Fig. 2.11), and ACLP and TLP displacements (Fig. 2.14) have all jumped upwards, but the values are not as high as at the beginning of life. The reactivity (Fig. 2.15) on the other hand, shows a drop of about 3 cents down to a value of -1.5 cents. This may seem to be somewhat unexpected, as the forces between the fuel ducts have increased, as may be observed by comparing the ACLP sections in Figs. 2.12 and 17. (The TLP sections may be compared in Figs. 2.13 and 2.18). However, comparison of Figs. 2.12 and 17 also shows that the spacing between the old fuel ducts has increased significantly, causing the actual drop in reactivity. For example, the increased outward bowing of the fresh outer core ducts (28), (43), and (74), have induced an obvious increased separation between (12) and (29), and between (27) and its adjacent ducts (28) and (42). We can also see other increased separations, as between (63) and (71), and between (40) and (53). The net effect of these induced separations is to cause a drop in the full power reactivity level.

2.2.1.6 Summary of Output Data at End of Second Fuel Cycle

The summary of full power output data at the end of the second fuel cycle (510 days) is shown in Table 2.7. We would expect a second refueling of, say, another one-third of the original ducts to again cause moderate discontinuous jumps in the maximum displacements, forces, and stresses. Based on the results from two cycles, it appears that the worst conditions in terms of maximum forces and stresses occur during full power at the beginning of life. As long as creep effects dominate the swelling effect, as is predicted by current correlations, longer term operation should not result in greater forces and stresses than found at BOL.

2.2.2 Power Ramps at Selected Points During Life

2.2.2.1 BOL Power Ramp

We have noted already (Fig. 2.9) how the interduct forces increase as the power at beginning of life is brought up to full operating value. The establishment of temperature gradients causes thermal bowing of the duct and constraining interference of neighboring ducts results in increasing interface forces. We see in Fig. 2.9 that the resultant lateral load exerted on each duct increases with increasing power. The particular duct which bears the maximum load may not remain the same during the power ramp. At first, duct (50) has the maximum load, then duct (37), then (20), and finally at full power duct (35) has a maximum total loading of about 6000 N. The displacements behave with a similar trend, increasing with increasing power. The reactivity change is shown in Fig. 2.19 as a function of the power/flow ratio. This ratio is directly related to the fraction of the radial temperature gradient at full power conditions. With decreasing power the reactivity drops uniformly from a maximum of about 7 cents; and if the ducts were to return to their exact original configuration, the reactivity should drop to zero at zero power. However, because of the clearances at the load pads and at the nozzle tip the ducts do not return exactly to their original vertical equilibrium alignment. As soon as the forces on a duct become zero, the position of the duct, within the allowable clearances, becomes indeterminate. The associated indeterminacy of the reactivity change is indicated in Fig. 2.19 by the dashed-line portion of the curve. The negative reactivity indicates that the particular indeterminate positions result in a net increased separation of fuel assemblies.

The conceptual diagram of Fig. 2.8 illustrates the thermal-bowing mechanism that results in increasing reactivity, as the reactor power is increased at the beginning of life. As time elapses, the full-power bowing of the ducts will be relaxed by creep. The thermal bowing curvature will not be as great as shown in the exaggerated schematic diagram, Fig. 2.20. The creep is manifested by permanent inelastic strains. When the power is shut down, the ducts will not return to their original BOL unstrained, straight vertical configuration. Rather, when the thermal gradient driving forces disappear, the relaxed ducts will assume an equilibrium configuration with a residual curvature opposite to the thermal bow curvature. Hence, it is apparent that the core regions of the fuel assemblies

will be bowed away from adjacent fuel assemblies, with the result that the reactivity effect will tend to be negative. This effect is shown clearly in Fig. 2.21 for the reactivity change at the end of the first fuel cycle, as explained in the following section.

2.2.2.2 Power Ramp at End of First Fuel Cycle

Under the duct bowing mechanism described above, a relatively large change in reactivity is observed in Fig. 2.21 during the shut-off power ramp from full power. The reactivity level is lowered about 17 cents from +1.5 cents down to about -15 cents. In the range of power reduction from 0.8 to 0.6 the curve is particularly steep, and shows a considerable sensitivity to power changes. In this range many of the fuel ducts are passing from the concave inward to the convex outward curvature (see Fig. 2.19). At this transition point considerable sensitivity can be expected. We see, in Fig. 2.22, at a power/flow ratio of 0.6, that there is scarcely any contact between the ducts at the TLP, indicating that the ducts are in a relatively straight, vertical, unbowed configuration, which is the configuration in which the greatest displacement sensitivity to small force changes should be expected. The small interface forces and larger clearances (about 2 mm) between some of the fuel ducts at the ACLP shown in Fig. 2.23 characterizes the negative reactivity.

At zero power, large spaces may be seen at the ACLP in Fig. 2.24 between fuel ducts, accounting for the -15 cents reactivity change. Some significant residual interface forces remain at both the ACLP and at the TLP (Fig. 2.25). The forces are the result of residual bowing remaining at zero power. The fuel ducts that are bowed apart in the core region (Fig. 2.24) which lower the reactivity level are pressed together at the TLP and produce the relatively high interface forces shown in Fig. 2.25. The residual bowing that causes fuel ducts to separate, will also cause the same ducts to press against neighboring ducts on the side opposite the separation. The resulting forces at the ACLP are shown in Fig. 2.24. While some of the neighbors are blanket ducts, a few are fuel ducts, and this compaction between fuel ducts should cause a local increase in reactivity; however, this effect is overridden by the more dominant separations, and as a result the net reactivity level is lowered. A summary of the output data at zero power and 275 days is listed in Table 2.8. The average duct temperatures are uniform, 595°F, so that there are no thermal gradients and, consequently, no thermal bowing. However, the maximum total residual displacements are of the order of 1.5 mm at the ACLP and

about 8 mm at the TLP. The maximum total lateral load is 4900 N, or about 1000 lb, exerted on duct (20). The maximum total lateral loading throughout the power ramp is shown in Fig. 2.26. The maximum load does not vary much: at full power a force of about 6600 N is exerted on duct (50) and then the load drops to about 3300 N on ducts (20) and (37), in the middle power/flow range, and finally, at zero power, slightly over 4900 N is exerted on duct (20). It is the magnitude at the force at zero power which is of importance when considering the frictional resistance to duct withdrawal.

The highest residual bending stress (Table 2.8(c)), is at the ACLP mid-flat of duct (35), a tensile stress of 34 MPa maximum stress at full power (see Table 2.5(c)), but much lower than the maximum stress of 131 MPa at the BOL full power operation. (See also, Fig. 2.10).

2.2.2.3 Power Ramp at Beginning of Second Fuel Cycle

The power-ramp reactivity change, shown in Fig. 2.27 fueling, has a total change of about 11 cents. The steepness of the curve in the 0.6 to 0.8 power/flow range is less severe, and together with the reduced reactivity change, the power-ramp reactivity curve is improved by the refueling. (Compare Fig. 2.27 with Fig. 2.21).

Comparison of the ACLP configuration at zero power after refueling (Fig. 2.28) with the ACLP configuration before refueling (Fig. 2.24), shows that the clearances between certain fuel ducts, particularly (28) and (29), (40) and (53), and (49) and (50), have been significantly reduced. This reduction in clearances between fuel ducts in the core region accounts for the increase in reactivity from -15 cents to a value of -12 cents after refueling.

To understand the detailed mechanisms involved in the duct displacement pattern in the core region presents a complex problem and requires examination of both the ACLP and TLP displacements and also the associated interface force patterns. For example, suppose we consider duct (49) which undergoes a significant outward displacement at the ACLP after refueling. (Compare Figs. 2.24 and 28). Since duct (49) is not a replacement duct, and the forces in the ACLP plane do not act in the direction of the displacement, the reason for the displacement is not apparent. However, in the TLP plane (Fig. 2.29) we saw that the adjacent duct (50) is replaced with a fresh unbowed duct, permitting duct (49) to move in the upward direction (in the figure), and for this reason the space in the ACLP

plane between (49) and (50) is reduced.

The residual forces and stresses at zero power, after refueling, are shown in Table 2.9. The maximum lateral load is about the same as before refueling; however, the 4900 N total load is now exerted on duct (38) rather than on duct (20). The variation of maximum lateral load throughout the power ramp is shown in Fig. 2.30. Although the zero-power load is the same before and after refueling, the full-power load after fueling is about double the load existing before fueling, over 12000 N compared to 6000 N.

Similarly, the zero-power maximum stress at the ACLP section has been reduced to about one-half the magnitude existing before refueling: from a peak of 34 MPa to a peak of 17 MPa. However, at full power, we see from Fig. 2.10 that the maximum stress has increased from 25 MPa (4000 psi) to 99 MPa (14000 psi) after refueling. Note that at zero power the highest stress, 19 MPa, occurs at the nozzle. At full power the maximum stress is at the ACLP rather than at the nozzle, although the nozzle stress increases to 20 MPa.

2.2.2.4 Power Ramp at End of Second Fuel Cycle

Comparison of the power ramp reactivity curves at the beginning of the second fuel cycle (Fig. 2.27) with the reactivity curve at the end of the cycle (Fig. 2.31) shows that although the end points have been raised several cents, the net difference in reactivity during the ramp has not been significantly changed. For an increase in reactor output from zero to full power, the corresponding total change at the end of the cycle is about 9 cents, compared to 11 cents at the beginning of the second fuel cycle. The differences between the reactivity ramps from beginning to end of the second fuel cycle is much less than the differences for the first fuel cycle. Hence, a stabilizing trend for subsequent fuel cycles is indicated in which changes in the power ramps with time may be expected to become more moderate.

The variation of maximum lateral load throughout the power ramp at the end of the second fuel cycle is shown in Fig. 2.32. Comparison with the lateral loads at the beginning of the fuel cycle (Fig. 2.30) shows a significant relaxation of the full-power load from about 12000 N to 7000 N. This full-power lateral load at the end of the second cycle is comparable to that at the end of the first fuel cycle. The zero-power maximum lateral load has remained essentially unchanged at a value of 4900 N throughout the full cycle.

2.3 ASSESSMENT OF THE DESIGN

The results of the core restraint calculations have been presented in the preceding sections of this chapter and the assessment of the free-flowering design with respect to its core restraint performance is given here. The assessment is complicated because both the preliminary state and the limited scope of the EPRI study prevent the core restraint system requirements from being finalized. The preliminary state of the study does not allow, for example, the detailed stress analysis of load pads to determine the allowable one-face and multiface loadings. Since the scope of the study was limited to the core region, the requirement of interfacing systems, such as the control rod drive system and the refueling system, cannot specify alignment requirements.

The assessment made here and in the next chapter on the core seismic performance is a preliminary one, based on the experience from other design assessments and limited by the lack of quantitative requirements from interfacing components and systems of this core system.

The maximum load on a single load pad face of any assembly in the core is about 5200 N (or 1200 lb); the maximum force on a load pad, that is the total of the loads on the six faces, is ∿18500 N (4200 lb). These forces, which occur at the beginning of life under full power conditions, are sufficiently high that further analysis is required to assess the design of the load pad. As noted earlier, these forces decrease rapidly, as irradition-induced creep relaxes the assembly bowing. The ACLP of the fuel assemblies, where these loads occur, is relatively soft so detailed structural analysis is needed to determine whether such a load pad could be designed to withstand both high loads and high compression. The full circumferential stiff load pad of the CRBRP assemblies can probably withstand such loads[5] but the soft "button" design of EBR-II may not, so a new load pad design may be needed. A solution other than designing the load pads, should be mentioned. A 50% reduction in the duct temperature gardients, which are known to be unrealistically high[6], would result in force levels about half of the calculated values. If more accurate duct temperature data were available, the loads may pose no problems to the load pad design and only a few straight-forward calculations would be needed to establish the feasibility of the design.

A reasonable maximum value for the withdrawal force during refueling operations is ∿4400 N (1000 lb) excluding the weight of the assembly. Using a reasonable value for the friction coefficient of 1.0 means that the total lateral force should be 4400 N (1000 lb) or less. The results predict a maximum total lateral force of ∿4400 N.

so that the most heavily loaded assembly could be removed first. A strategy of removing first the assemblies which have low lateral loads may well result in lowering the lateral forces on the assemblies which are heavily loaded. In view of the above information, the free-flowering design appears to meet the force limit set by the refueling system.

The peak duct bending stress of 130 MPa (∿19 ksi) occurs in the ACLP at the BOlC under full power conditions. If other substantial stresses occur in the duct, the total stress may exceed the allowable. This situation is not bad, however; the duct design could be changed slightly, more realistic temperature gradients could be used as input or a temporary solution (e.g. reduced power/flow level) could be employed until irradiation-creep has reduced the stress levels. It appears that bending stresses will not present any insurmountable problems for the free-flowering core.

The limit on top-end deflection under power conditions is set by the alignment requirement of the control-rod drive system. The misalignment value assigned to the core restraint system is about 10 mm for the CRBRP;[5] it is several times larger for the Phenix reactor.[6] The maximum top-end displacement for the control assemblies under full power conditions is calculated to be 8.1 mm for Assembly #4, considerably below the restrictive CRBRP value. The design appears to have no difficulty in meeting this requirement.

The misalignment value for assembly top-ends assigned to the core restraint system is about 10-15 mm in the CRBRP.[5] A maximum displacement of 8.3 mm is predicted for an assembly under refueling conditions at 255 days. The design appears to meet this requirement without difficulty.

The power coefficient is composed of reactivity effects due to doppler, sodium density, and axial expansion, in addition to the bowing or radial movement. From zero to full power the sodium contribution for the core, which has ∿$2.5 sodium worth value, is about +15¢, the doppler is about -$2.00, and the axial expansion worth is small and negative. More accurate values may be obtained from the values appearing in the neutronic analysis. The maximum values of the bowing during the first two cycles is ∿+16¢, most of which takes place from zero to 30% power. From these values, even though some are very approximate, it is clear that the power coefficient should be negative over the power range. It is also apparent that the negative components (i.e., doppler) would dominate any power increase event so the system meets the minimum requirement of allowing the reactor to be brought to power easily and safely.

The assessment has found that the free-flowering core exhibits satisfactory core restraint performance. The single area of concern is the maximum force limits at the contact points of the assemblies. If more detailed structural analysis shows that the forces are too high, two options are available: (1) perform more refined duct temperature calculations which are expected to give lower temperature gradients and thus lower contact forces; or (2) modify the duct design slightly to bring the stresses within allowable limits.

2.4 CONCLUSIONS

In the previous section the results of the core restraint analysis were assessed against typical values for force, displacement and reactivity effects with the overall finding that the core restraint system performed in an acceptable manner. This section presents the key features of the core restraint system and their role in influencing its performance. Since the core design is distinguished by a free-flowering restraint concept and a heterogeneous core layout, the key features will be discussed in terms of both.

2.4.1 Free-Flowering Concept

a. Stiff Reflector Assemblies. The displacement of the core assemblies which reside in temperature and fluence gradients must be limited by some means other than restraint rings. The approach in this design is to use stiff reflector assemblies which resist the bowing of fuel and blanket assemblies and allow irradiation creep to relax the stresses which tend to displace the assemblies. The reflector assemblies should not, in principle, be extremely stiff, e.g. as stiff as the restraint rings. In practice, however, dimensional limitations in the core dictate that the assemblies should be as stiff as the design limitation would allow. Thus, the reflectors should be made out of solid metal blocks rather than pins with a thin duct and should be a single axial member rather than articulated.

b. Flexible Fuel and Internal Blanket Assemblies. In contrast to the reflector assemblies, the fuel and internal blanket assemblies should be flexible, particularly in the fissile region where the greatest amount of creep is needed to maintain relatively straight assemblies. In this design the duct wall thickness, which was set primarily by neutronic and bulging considerations, is acceptably flexible.

c. Tight Nozzle Clearances. The clearance in the nozzle of all assemblies should be as small as allowable. Small clearances restrict the rotation of the top-end and sets up greater bending stress as a neighbor displaces the assembly. The design has an acceptable nozzle clearance. If top-end misalignment requirements (control rod drive and fuel handling) are relaxed, the nozzle clearance may be relaxed also.

d. Top-end Misalignments. In a design with a fixed radial boundary, e.g. a core restraint ring, the clearances in a load plane determine the maximum possible displacements. Thus, very tight top-end misalignment requirements could, in principle, be imposed on the core restraint system. (From practical considerations there are limits on this requirement). The flexible radial boundary on the limited free bow design cannot meet highly restrictive top-end misalignment requirements. Thus, the designers of the interfacing systems imposing these requirements should be urged to choose features in their systems which relax the misalignment requirements. The values of acceptable misalignment, i.e. $\sim$10-15 mm are satisfied by this free-flowering design, but additional margin would be very desirable to cover calculational uncertainties.

2.4.2 Heterogeneous Core

The features of a heterogeneous core which influence core restraint performance and of which the system engineer should be cognizant are:

a. Flux and Temperature Gradients. The gradients are greater on the average in heterogeneous core and change appreciably during power operation. Greater care must be taken in calculating the gradients and they must be calculated several times during the core lifetime, taking into account replacement of the fuel and blanket assemblies. A major source of uncertainties in the analysis arises from uncertainties in the value of the flux and temperature and their gradients.

b. Changes in Performance Throughout Core Life. The large swings in flux and temperature gradients with time produces changes in the loading levels and their pattern throughout the core history. In analyzing the core restraint performance of a

heterogeneous core one must carry the calculations through several cycles before an envelope of the performance characteristic is determined.

c. Higher Forces Early in Life. The analysis presented here showed the forces to be significantly higher early in life because of the large and interactive thermal bow of the assemblies in a heterogeneous core. This behavior suggests certain design options which could be introduced into the first cycle. For example, the internal blanket assemblies which are removed at the end of the first or second cycle could contain fissile material so the gradients between them and adjacent fuel assemblies are reduced.

d. Load Pad Design. The load pad on the duct wall of an assembly must meet the challenge of being sufficiently soft to produce acceptably low forces in the load plane but sufficiently firm to limit the amount of compression from both a mechanical and neutronic viewpoint. From a mechanical viewpoint, the strain on the load pad must be acceptable and from the neutronic side the reactivity effect due to compressing the active core must not produce an unacceptably positive power coefficient.

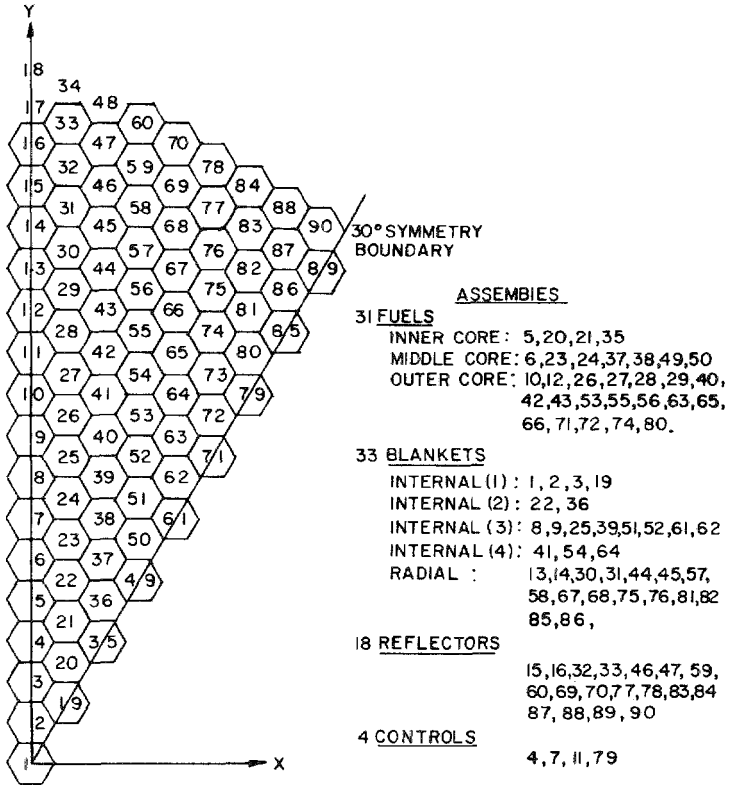

Fig. 2.1. Symmetrical Section (30°) of Fuel Subassembly System (Plan View)

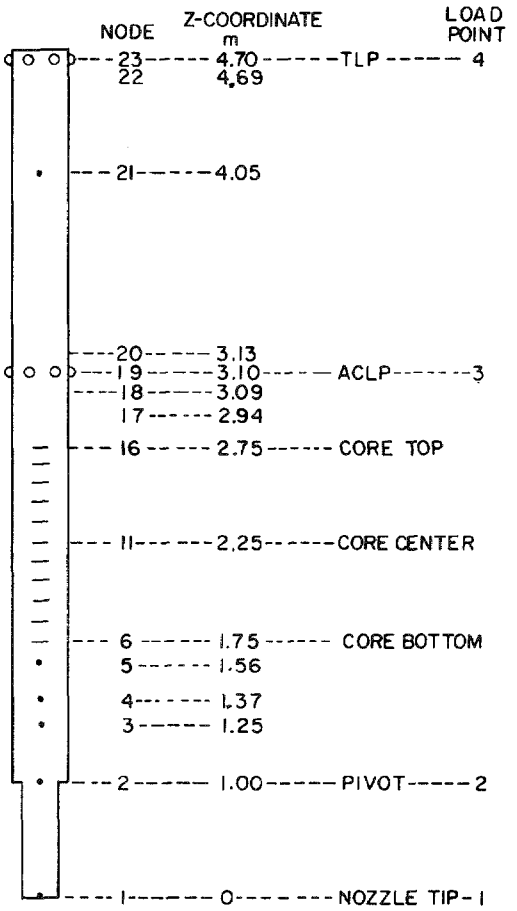

Fig. 2.2. Outer Dimensions of Eact Assembly and Definition of Axial Computational Nodes (Axial Section View)

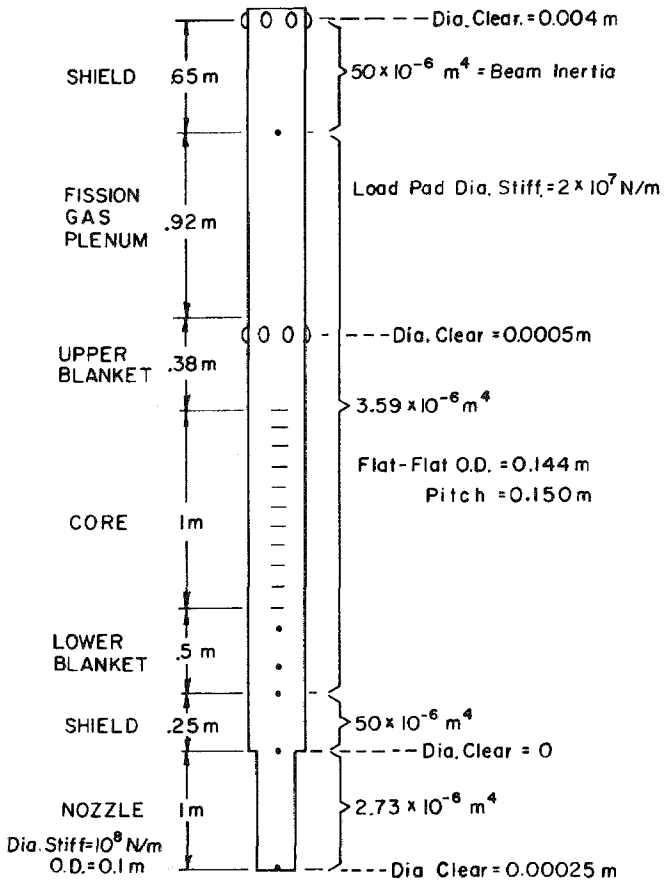

Fig. 2.3. Axial Section of Fuel and Blanket Assemblies

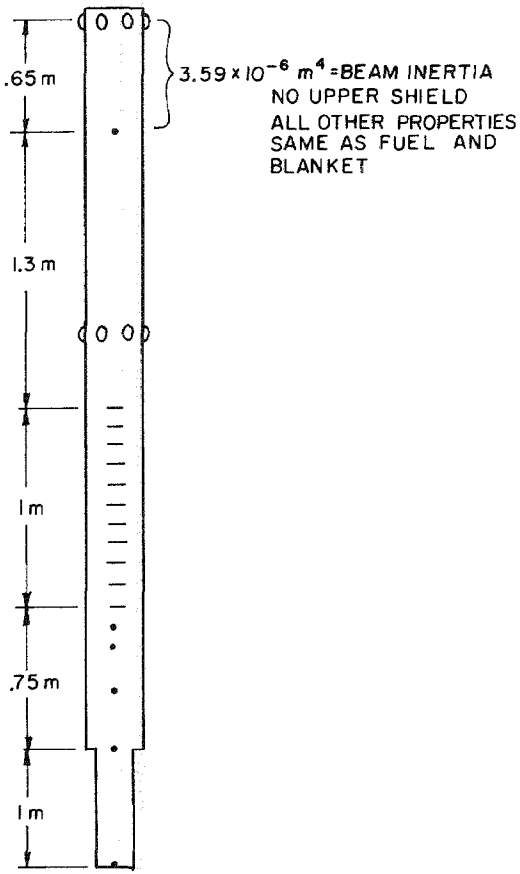

Fig. 2.4. Axial Section of Control Assembly

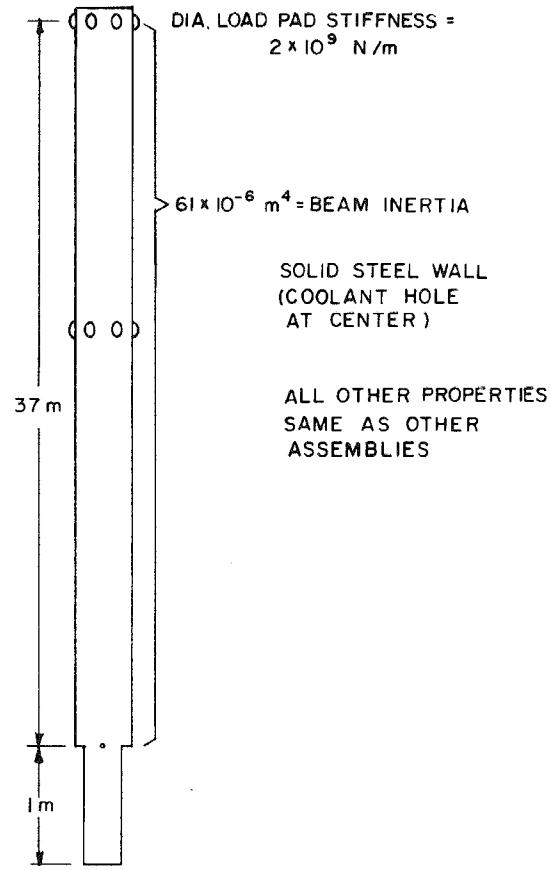

Fig. 2.5. Axial Section of Reflector Assembly

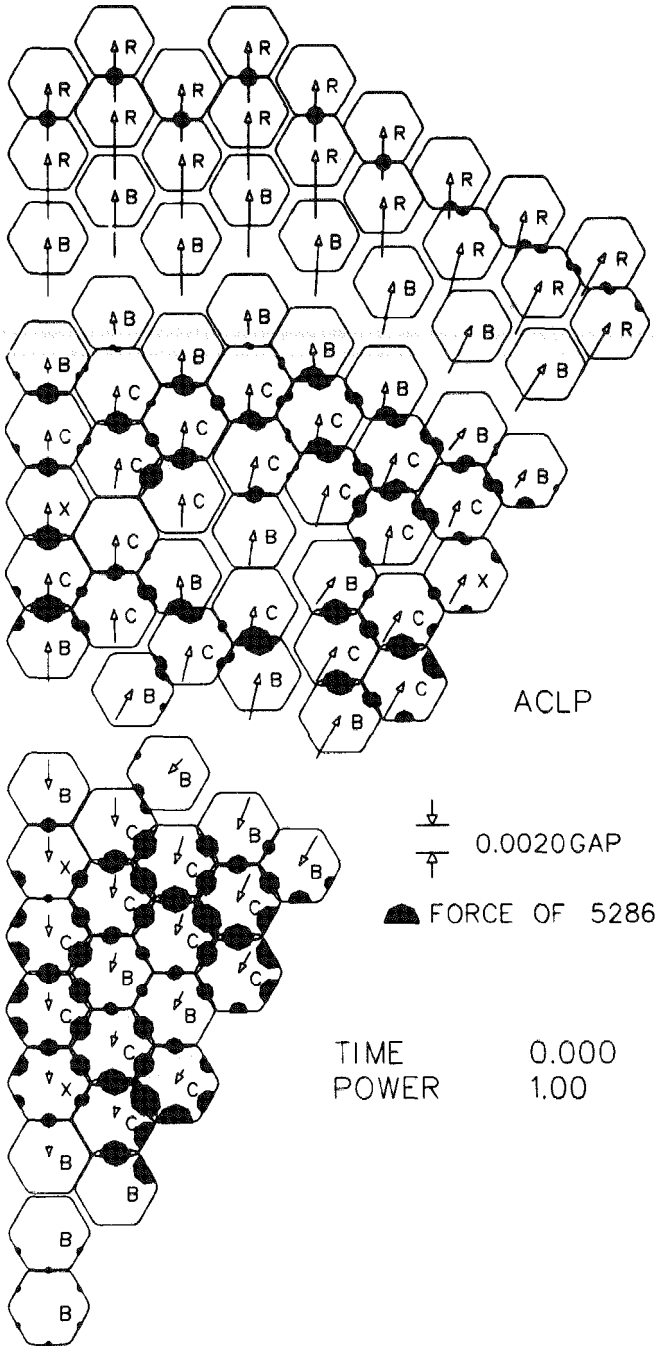

Fig. 2.6. Full Power Displacements and Forces at ACLP at Beginning of Life (BOL)

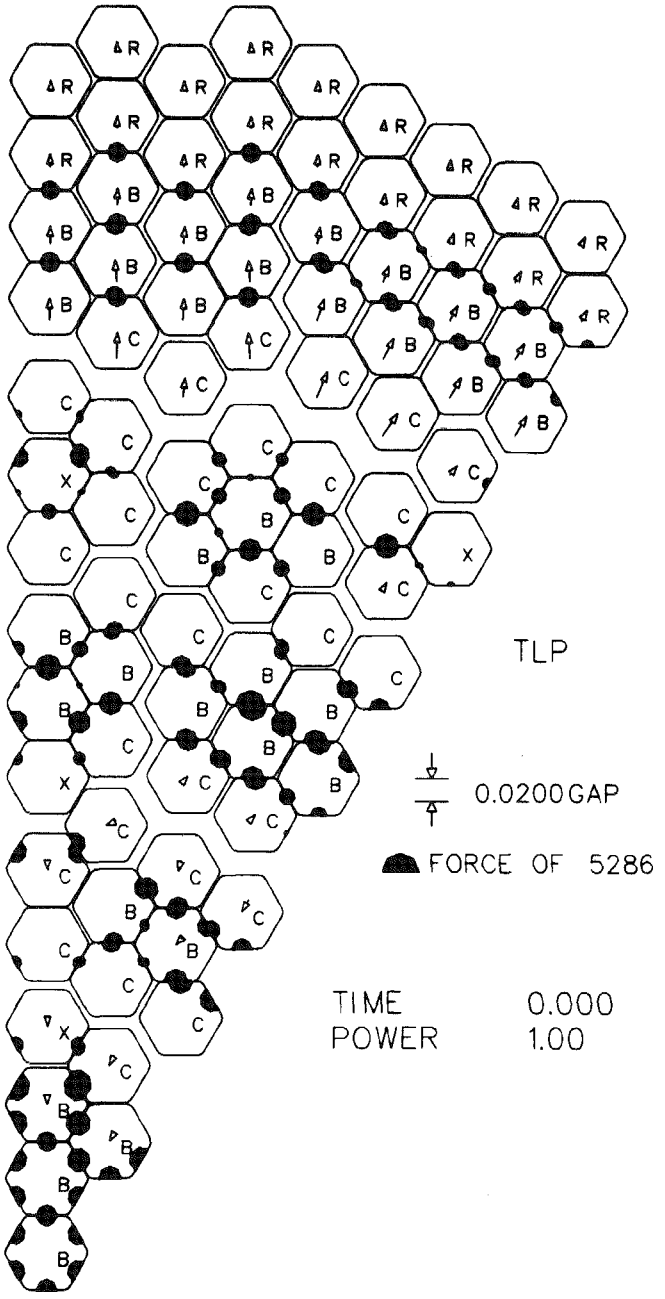

Fig. 2.7. Full Power Displacements and Forces at TLP at BOL

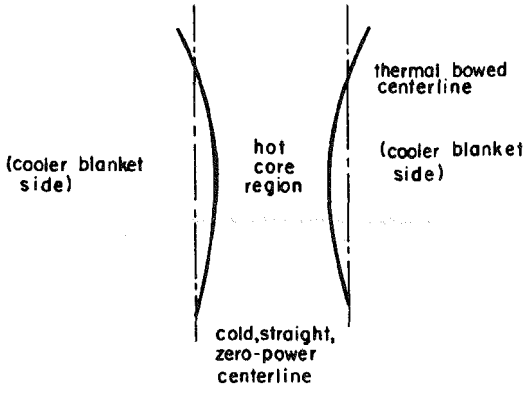

Fig. 2.8. Conceptual Diagram Illustrating Thermal Bowing at BOL

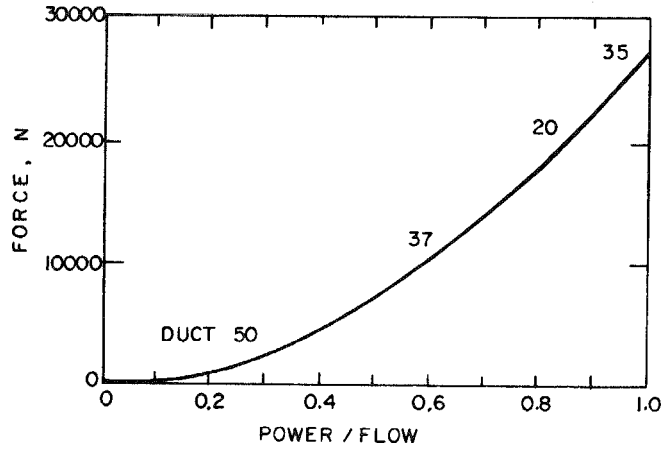

Fig. 2.9. Variation of Maximum Total Lateral Load on a Single Duct during Power Ramp at BOL

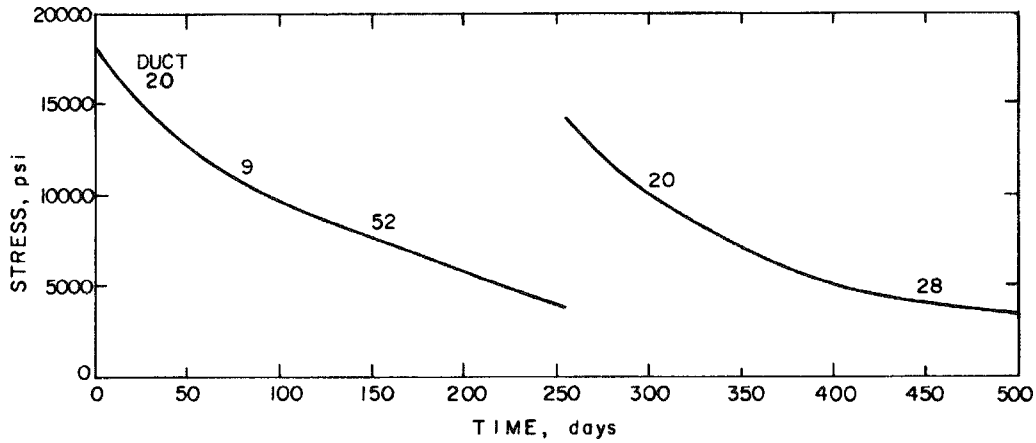

Fig. 2.10. Full Power Time History of Maximum Bending Stress at ACLP

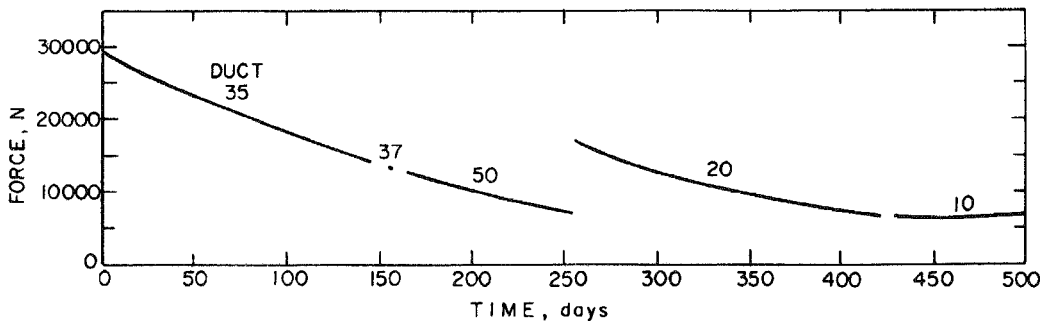

Fig. 2.11. Full Power Time History of Maximum Total Lateral Load on a Single Duct

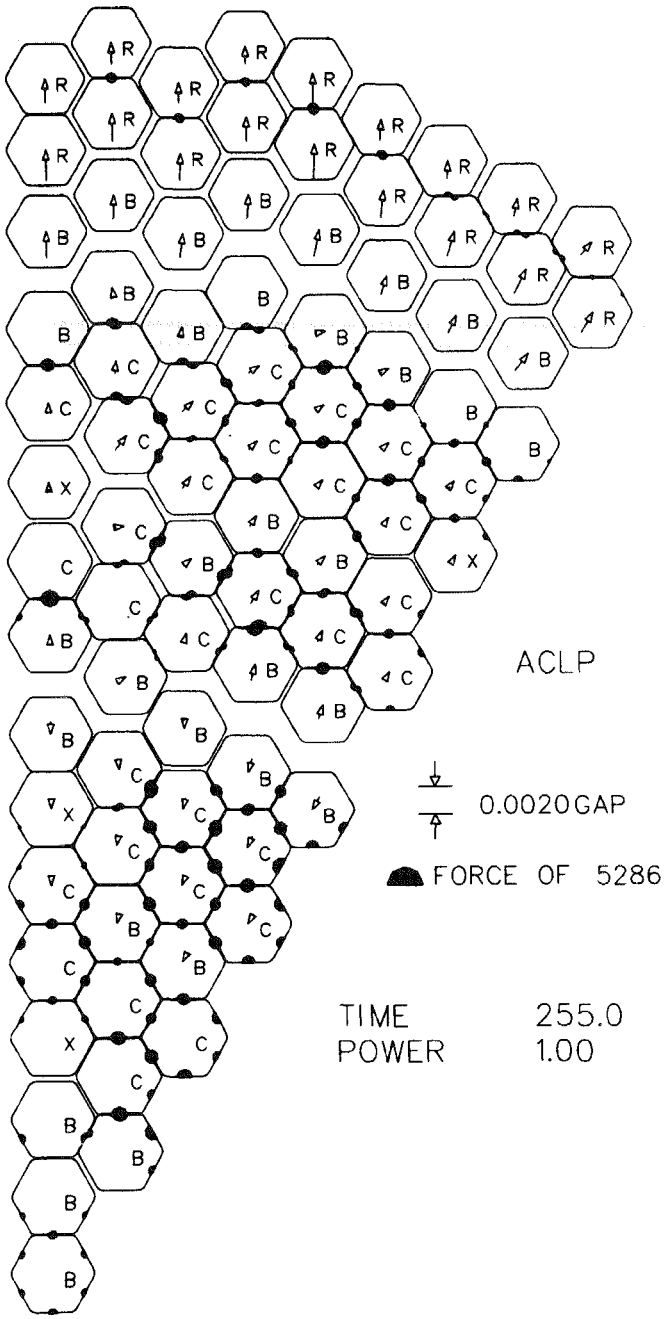

Fig. 2.12. Full Power Displacements and Forces at ACLP at End of First Fuel Cycle (E01C)

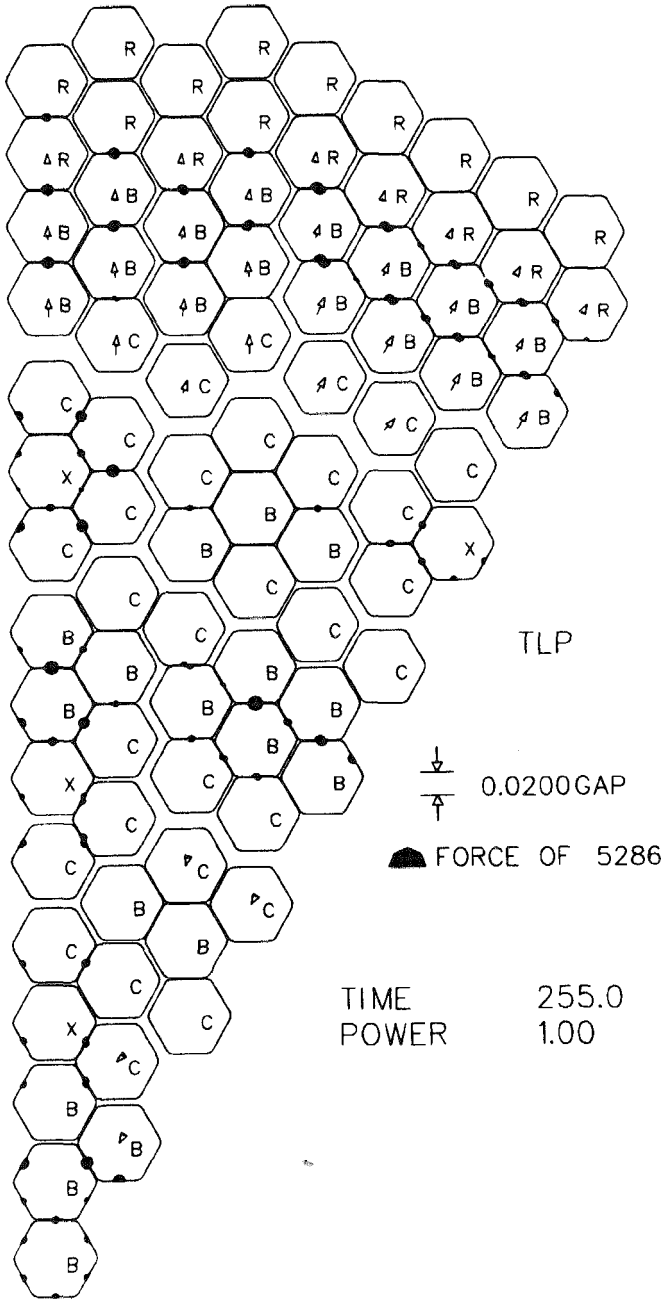

Fig. 2.13. Full Power Displacements and Forces at TLP at E01C

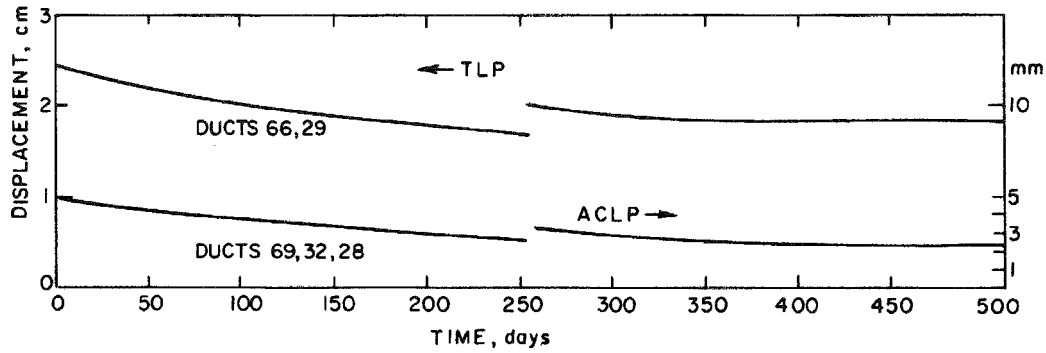

Fig. 2.14. Full Power Maximum Load-Pad Displacement-Time Histories

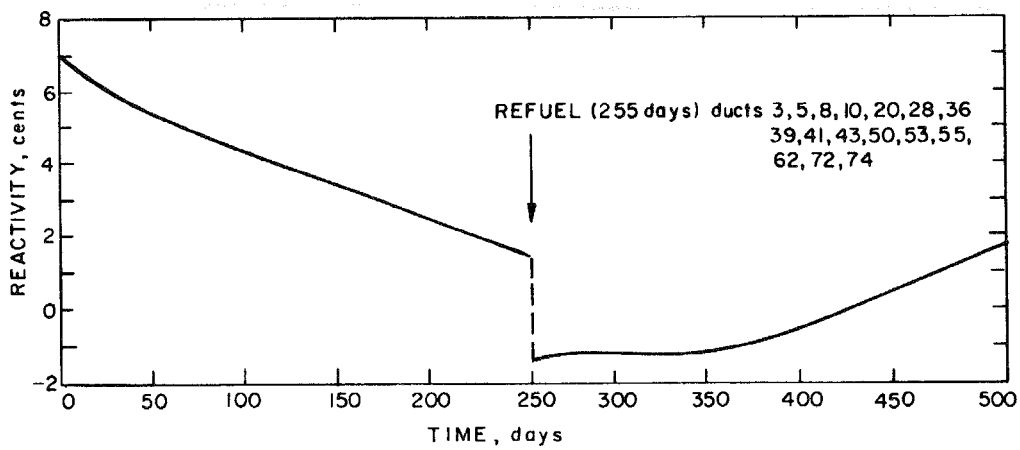

Fig. 2.15. Full Power Reactivity Change Time History for Variable Temperature and Refueling

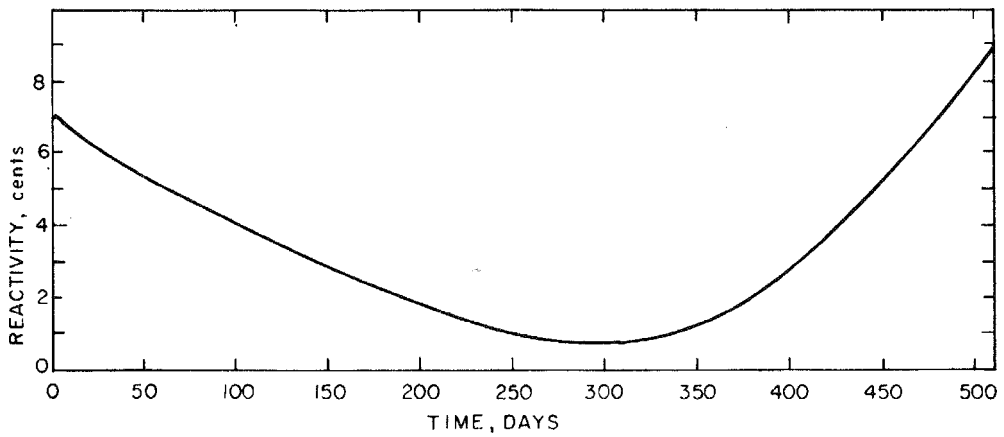

Fig. 2.16. Full Power Reactivity Change Time History for a Constant Temperature Distribution and No Refueling

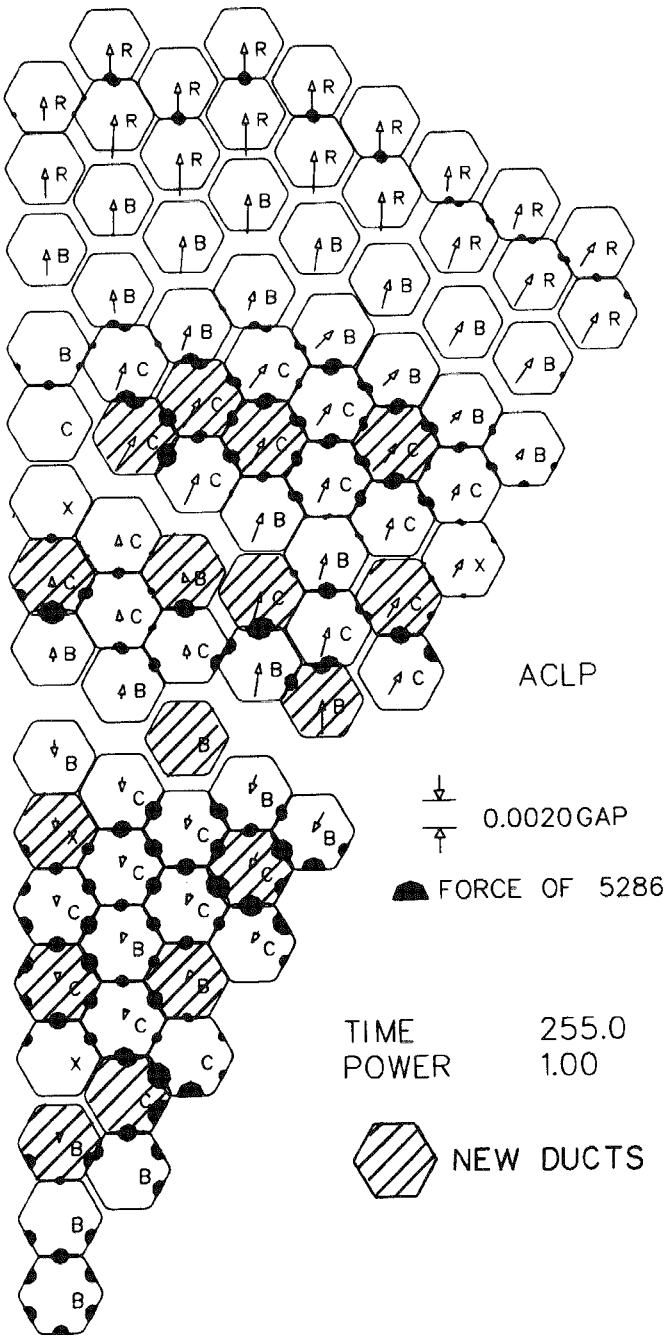

Fig. 2.17. Full Power Displacements and Forces at ACLP at Beginning of Second Fuel Cycle (B02C)

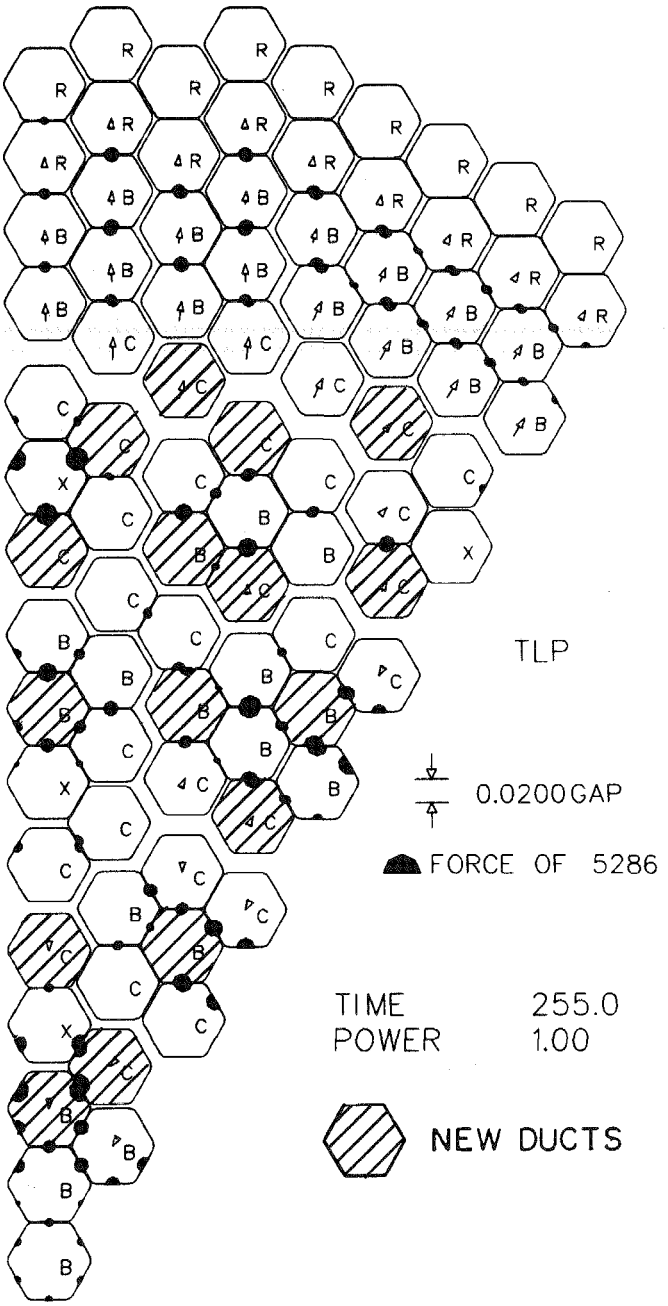

Fig. 2.18. Full Power Displacements and Forces at ACLP at B02C

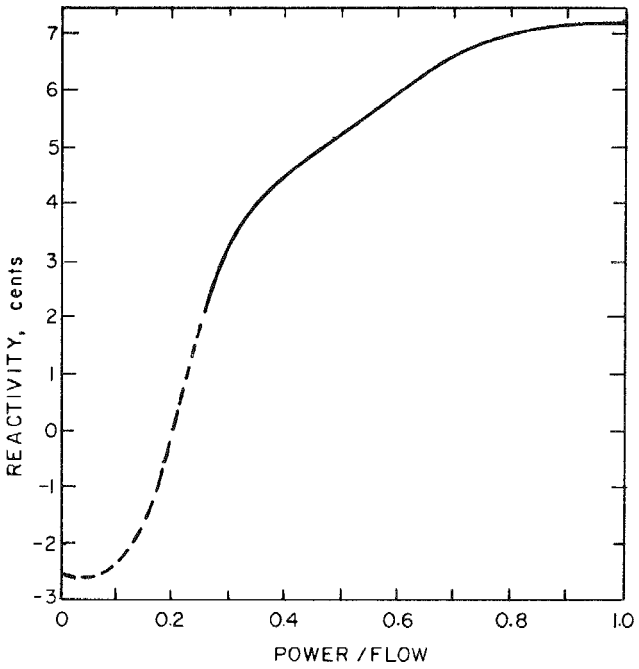

Fig. 2.19. Variation of Reactivity Change during Power Ramp at BOL

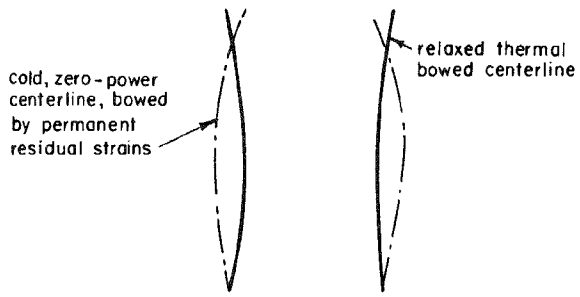

TWO ADJACENT FUEL ASSEMBLIES

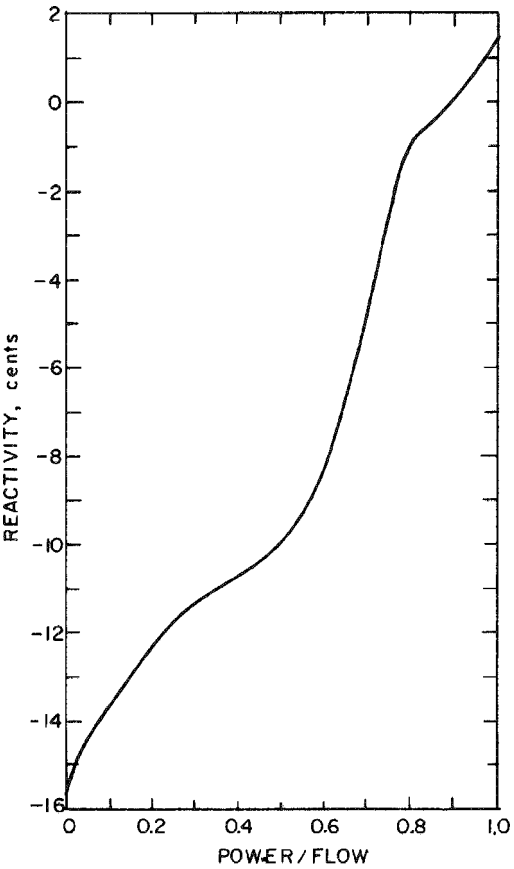

Fig. 2.21. Variation of Reactivity Change during Power Ramp at EOlC

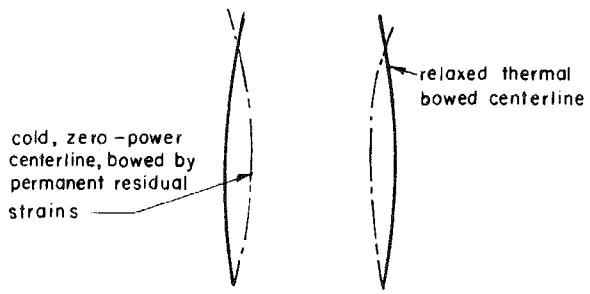

TWO ADJACENT BLANKET ASSEMBLIES

Fig. 2.20. Conceptual Diagram Illustrating Thermal Bowing Later in Life

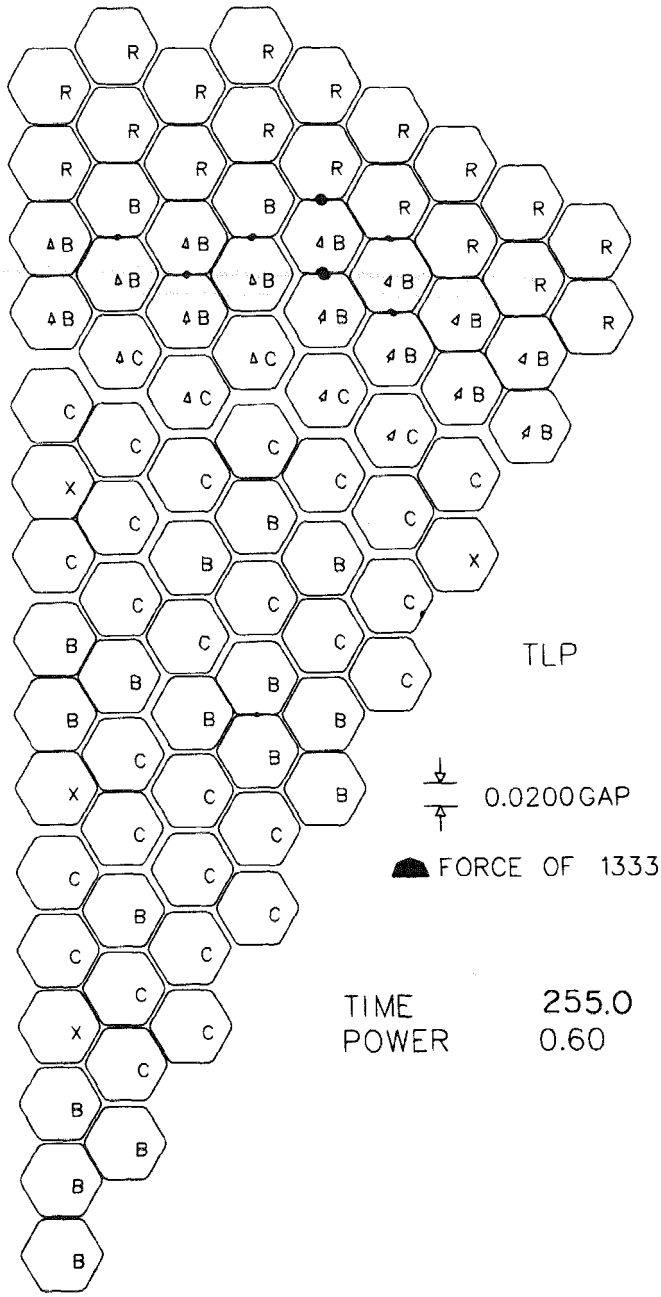

Fig. 2.22. TLP Duct Configuration at an Intermediate Power/Flow Ratio of 0.6 at E01C

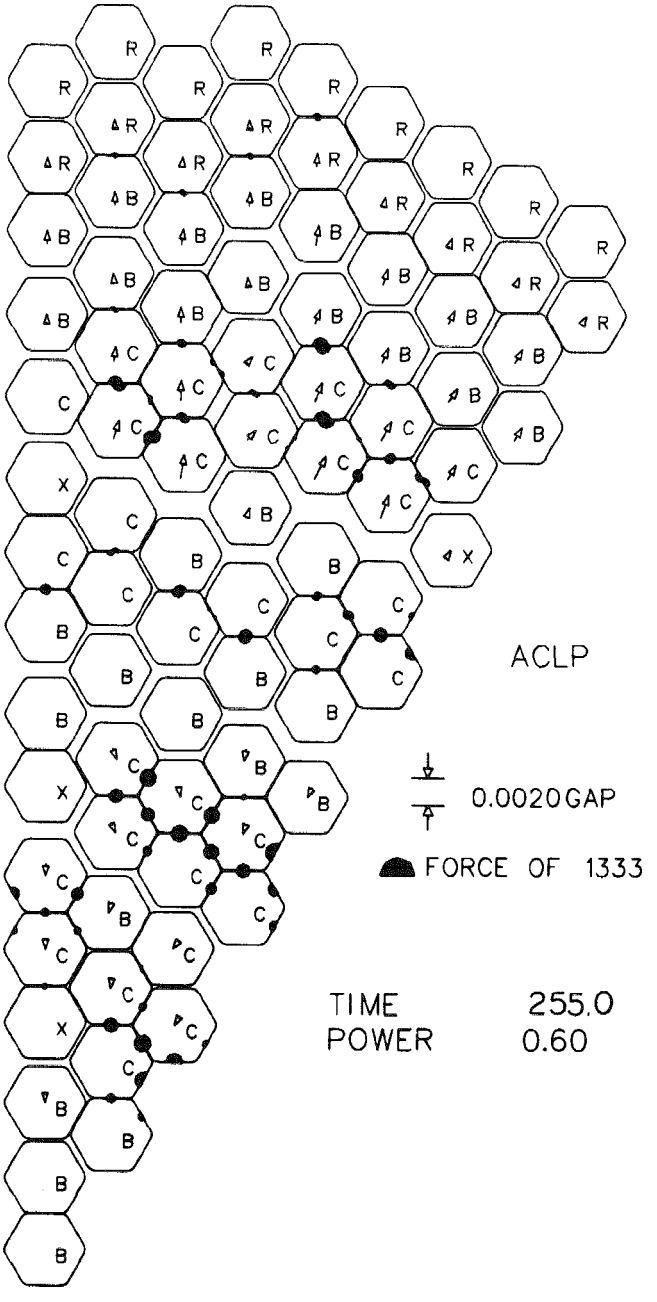

Fig. 2.23. ACLP Duct Configuration at an Intermediate Power/Flow Ratio of 0.6 at E01C

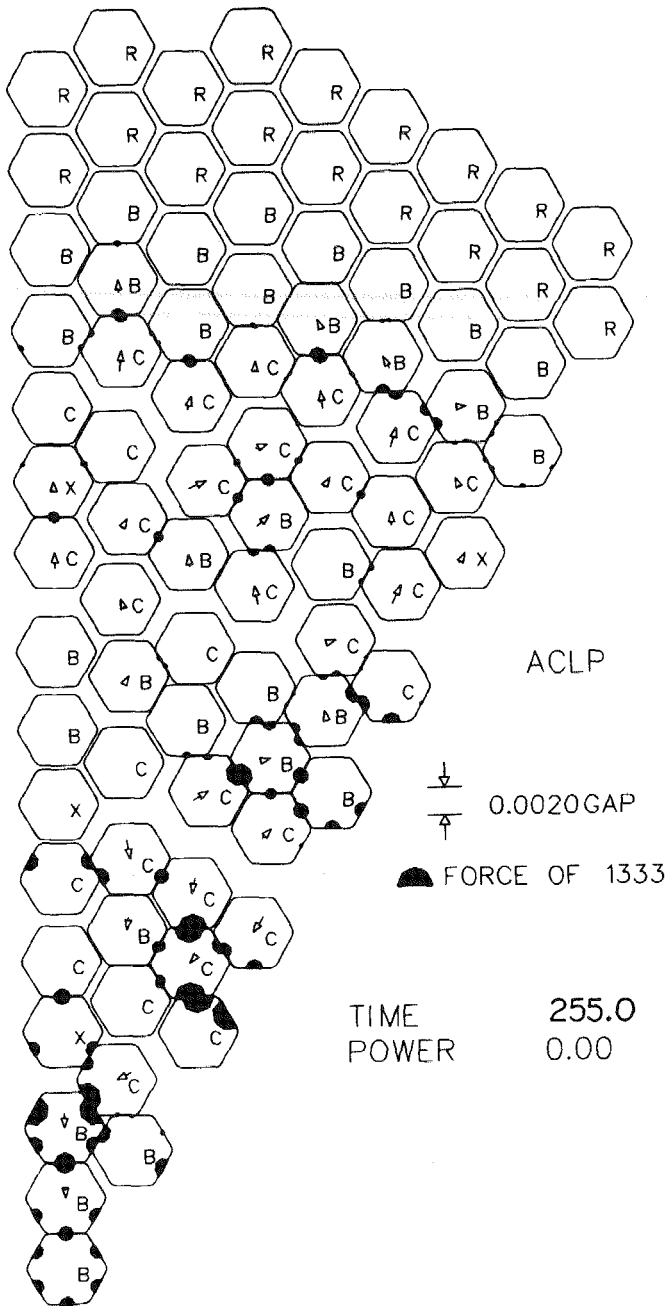

Fig. 2.24. ACLP Zero-Power Duct Configuration at E01C

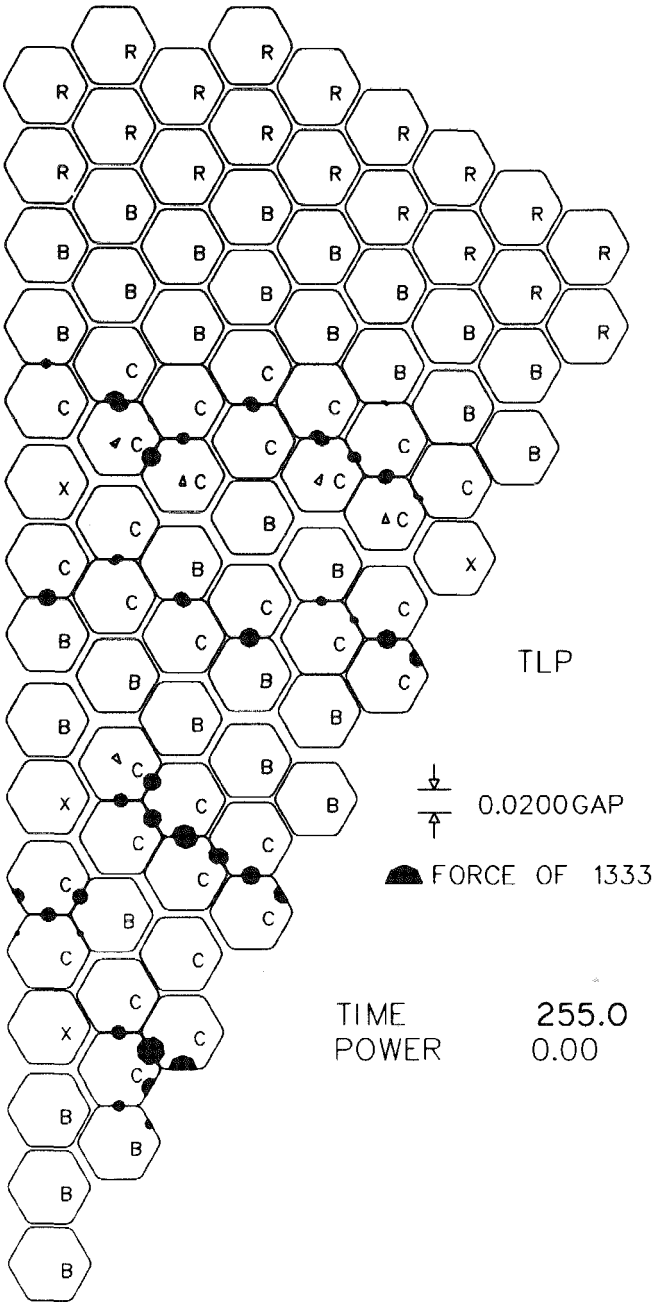

Fig. 2.25. TLP Zero-Power Duct Configuration at E01C

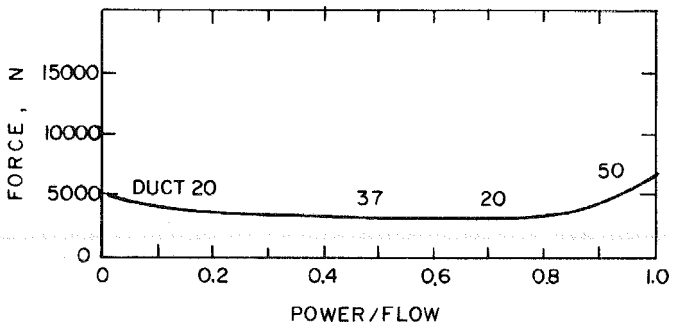

Fig. 2.26. Variation of Maximum Total Lateral Load on a Single Duct during Power Ramp at E01C

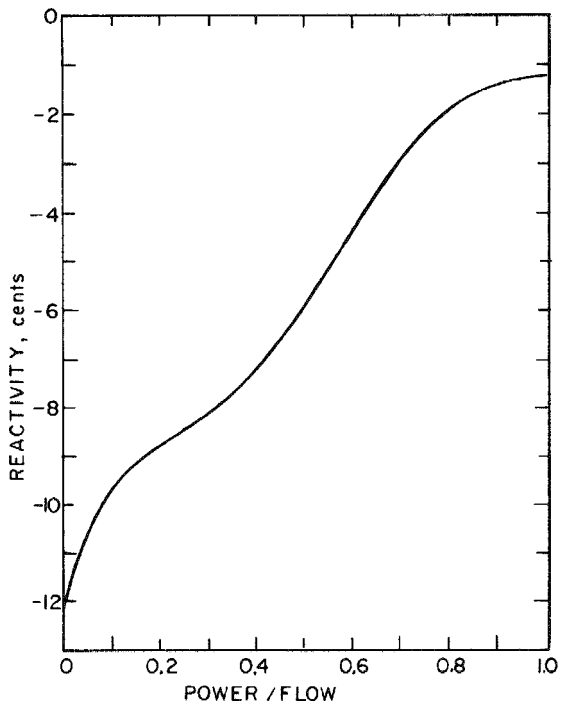

Fig. 2.27. Variation of Reactivity Change during Power Ramp at B02C

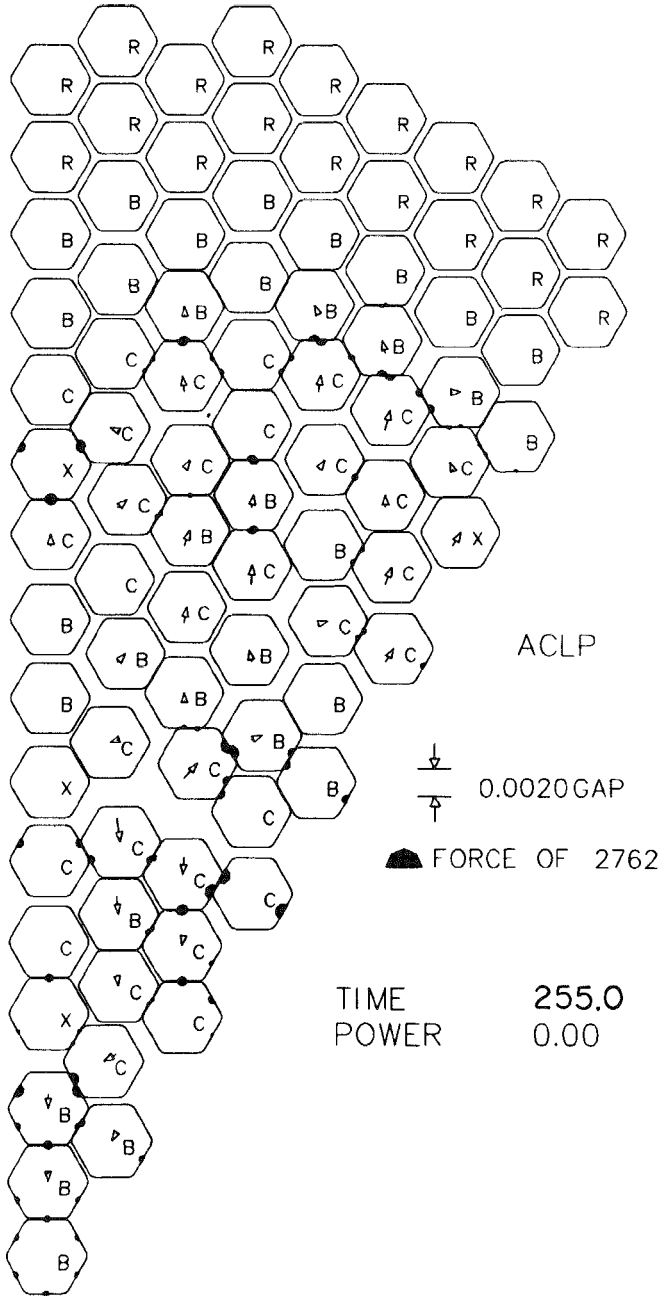

Fig. 2.28. ACLP Zero-Power Duct Configuration at B02C

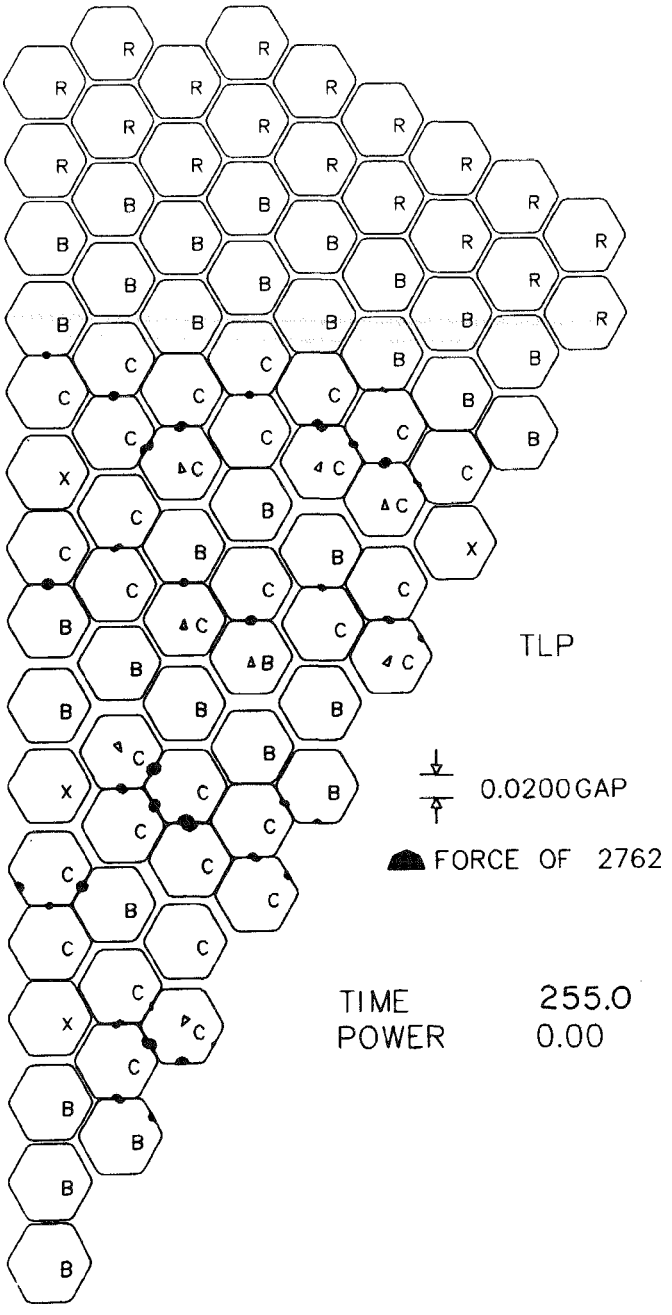

Fig. 2.29. TLP Zero-Power Duct Configuration at B02C

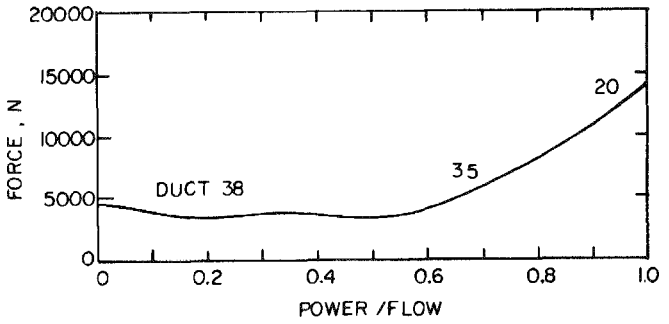

Fig. 2.30. Variation of Maximum Total Lateral Load on a Single Duct during Power Ramp at B02C

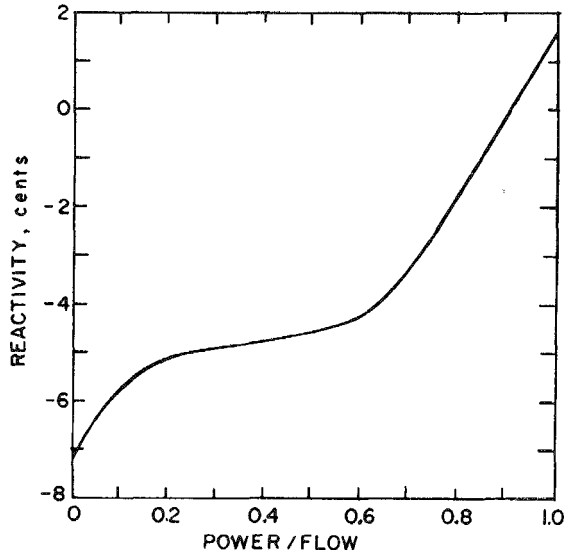

Fig. 2.31. Variation of Reactivity Change during Power Ramp at End of Second Fuel Cycle (E02C)

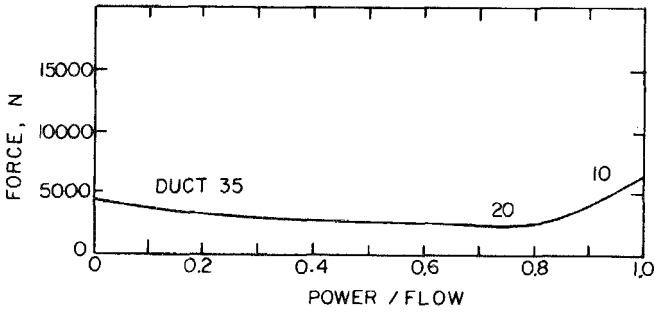

Fig. 2.32. Variation of Maximum Total Lateral Load on a Single Duct during Power Ramp at E02C

Table 2.1. Sample Computer Output - Prebow Conditions

SYSTEM DESCRIPTION AFTER STRAIN CALCULATION: STEP 28 AT TIME 127.50 DAYS

EPRI3 PGM1 NAMELIST DATA

SYSTEM DESCRIPTION:
18 ROW-30 DEG. SECTOR 90 (TOTAL) DUCTS WITH 4 LOAD POINTS. 2 SUPPORT POINT(S) AT LOAD POINT(S) 1, 2,
SYSTEM BOXED SHAPES AND CLEARANCES AT LOAD POINTS

DUCT	LEVEL	VTX	VTY	VPX	VPY	DEL(1)	DEL(2)	DEL(3)	DEL(4)	DEL(5)	DEL(6)
1	1	0.0	0.0	0.0	0.0	1.2573D-04	1.2573D-04	1.2573D-04	1.2573D-04	1.2573D-04	1.2573D-04
1	2	0.0	0.0	0.0	0.0	-3.4897D-18	-3.4897D-18	-3.4897D-18	-3.4897D-18	-3.4897D-18	-3.4897D-18
1	3	0.0	0.0	0.0	0.0	4.1925D-04	4.1925D-04	4.1925D-04	4.1925D-04	4.1925D-04	4.1925D-04
1	4	0.0	0.0	0.0	0.0	3.9405D-03	3.9405D-03	3.9405D-03	3.9405D-03	3.9405D-03	3.9405D-03
2	1	0.0	0.0	0.0	0.0	1.2573D-04	1.2573D-04	1.2573D-04	1.2573D-04	1.2573D-04	1.2573D-04
2	2	0.0	0.0	0.0	0.0	-3.4897D-18	-3.4897D-18	-3.4897D-18	-3.4897D-18	-3.4897D-18	-3.4897D-18
2	3	0.0	-3.5322E-04	0.0	0.0	3.7046D-04	3.6058D-04	4.1540D-04	4.1925D-04	4.1564D-04	3.6058D-04
2	4	0.0	-3.2156E-03	0.0	0.0	3.8825D-03	3.8825D-03	3.9367D-03	3.9405D-03	3.9367D-03	3.8825D-03
3	1	0.0	0.0	0.0	0.0	1.2573D-04	1.2573D-04	1.2573D-04	1.2573D-04	1.2573D-04	1.2573D-04
3	2	0.0	0.0	0.0	0.0	-3.4897D-18	-3.4897D-18	-3.4897D-18	-3.4897D-18	-3.4897D-18	-3.4897D-18
3	3	0.0	-1.6509E-03	7.5507D-18	3.4186D-04	2.8823D-04	2.1494D-04	3.1549D-04	3.7046D-04	3.1549D-04	2.1494D-04
3	4	0.0	-1.2501E-02	3.1416D-17	1.2779D-03	3.8126D-03	3.7329D-03	3.8330D-03	3.8925D-03	3.8332D-03	3.7329D-03
4	1	0.0	0.0	0.0	0.0	1.2573D-04	1.2573D-04	1.2573D-04	1.2573D-04	1.2573D-04	1.2573D-04
4	2	0.0	0.0	0.0	0.0	-3.4897D-18	-3.4897D-18	-3.4897D-18	-3.4897D-18	-3.4897D-18	-3.4897D-18
4	3	0.0	-1.7354E-03	1.6677D-17	3.8571D-04	1.7115D-04	1.7324D-04	1.7872D-04	2.0823D-04	1.7872D-04	1.7324D-04
4	4	0.0	-1.4295E-02	6.2956D-17	1.6122D-03	3.6967D-03	3.6002D-03	3.7046D-03	3.8126D-03	3.7046D-03	3.6902D-03
5	1	0.0	0.0	0.0	0.0	1.2573D-04	1.2573D-04	1.2573D-04	1.2573D-04	1.2573D-04	1.2573D-04
5	2	0.0	0.0	0.0	0.0	-3.4897D-18	-3.4897D-18	-3.4897D-18	-3.4897D-18	-3.4897D-18	-3.4897D-18
5	3	0.0	-7.9861E-04	2.9411D-17	3.9707D-04	8.8115D-05	1.4040D-04	9.1379D-05	1.7115D-04	9.1379D-05	1.4040D-04
5	4	0.0	-5.8798E-03	9.9125D-17	1.5917D-03	3.6154D-03	3.6666D-03	3.6106D-03	3.6967D-03	3.6106D-03	3.6666D-03
6	1	0.0	0.0	0.0	0.0	1.2573D-04	1.2573D-04	1.2573D-04	1.2573D-04	1.2573D-04	1.2573D-04
6	2	0.0	0.0	0.0	0.0	-3.4897D-18	-3.4897D-18	-3.4897D-18	-3.4897D-18	-3.4897D-18	-3.4897D-18
6	3	0.0	7.9826E-04	2.9915D-17	-2.8129D-03	1.7069D-04	7.0651D-05	1.3923D-04	8.8116D-05	1.3923D-04	7.0651D-05
6	4	0.0	5.8370E-03	1.0162D-16	-1.0285D-02	3.6963D-03	3.5983D-03	3.6655D-03	3.6154D-03	3.6655D-03	3.5983D-03
7	1	0.0	0.0	0.0	0.0	1.2573D-04	1.2573D-04	1.2573D-04	1.2573D-04	1.2573D-04	1.2573D-04
7	2	0.0	0.0	0.0	0.0	-3.4897D-18	-3.4897D-18	-3.4897D-18	-3.4897D-18	-3.4897D-18	-3.4897D-18
7	3	0.0	1.8735E-03	1.6941D-17	-3.3962D-04	2.9092D-04	2.0195D-04	1.5440D-04	1.7069D-04	1.5440D-04	2.0195D-04
7	4	0.0	1.5336E-02	6.3393D-17	-1.2551D-03	3.8221D-03	3.7271D-03	3.6883D-03	3.6963D-03	3.6883D-03	3.7271D-03
8	1	0.0	0.0	0.0	0.0	1.2573D-04	1.2573D-04	1.2573D-04	1.2573D-04	1.2573D-04	1.2573D-04
8	2	0.0	0.0	0.0	0.0	-3.4897D-18	-3.4897D-18	-3.4897D-18	-3.4897D-18	-3.4897D-18	-3.4897D-18
8	3	0.0	1.7643E-03	4.9160D-18	-4.2436D-04	3.2030D-04	3.2139D-04	2.4644D-04	2.9092D-04	2.4644D-04	3.2140D-04
8	4	0.0	1.3236E-02	2.1431D-17	-1.7413D-03	3.8438D-03	3.8477D-03	3.7709D-03	3.8221D-03	3.7709D-03	3.8477D-03
9	1	0.0	0.0	0.0	0.0	1.2573D-04	1.2573D-04	1.2573D-04	1.2573D-04	1.2573D-04	1.2573D-04
9	2	0.0	0.0	0.0	0.0	-3.4897D-18	-3.4897D-18	-3.4897D-18	-3.4897D-18	-3.4897D-18	-3.4897D-18
9	3	0.0	-4.2370E-03	7.4437D-18	2.3124D-03	1.8159D-04	2.0024D-04	3.0175D-04	3.2030D-04	3.0175D-04	2.0024D-04
9	4	0.0	-3.2317E-02	3.0073D-17	8.6535D-03	3.7071D-03	3.7255D-03	3.8259D-03	3.8438D-03	3.8259D-03	3.7255D-03
10	1	0.0	0.0	0.0	0.0	1.2573D-04	1.2573D-04	1.2573D-04	1.2573D-04	1.2573D-04	1.2573D-04
10	2	0.0	0.0	0.0	0.0	-3.4897D-18	-3.4897D-18	-3.4897D-18	-3.4897D-18	-3.4897D-18	-3.4897D-18
10	3	0.0	5.0725E-04	4.2524D-17	-7.0561D-04	1.3877D-04	6.9227D-05	8.4578D-05	1.8159D-04	8.4578D-05	6.9227D-05
10	4	0.0	3.2650E-03	1.4296D-16	-2.8081D-03	3.6649D-03	3.5969D-03	3.6121D-03	3.7071D-03	3.6121D-03	3.5969D-03

Table 2.2. Sample Computer Output - Converged Equilibrium Forces and Displacements

EPRI FGM1 NAMELIST DATA
CONVERGED RESULTS FOR STEP 29 AT TIME = 127.50 PASSES= 516 ITERATIONS = 2 TIME USED = 152.00 SEC. FMAX = 1.000
STIFFNESSES: 1.99800 08=K(1) 1.99800 08=K(2) 1.00000 07=K(3) 1.00000 07=K(4)

DUCT	LEVEL	F1	F2	F3	F4	F5	F6	VX	VY	RX	RY
1	1	0.0	0.0	0.0	0.0	0.0	0.0	0.0	0.0	0.0	0.0
1	2	0.0	0.0	0.0	0.0	0.0	0.0	0.0	0.0	0.0	0.0
1	3	97.52	97.52	97.52	97.52	97.52	97.52	0.0	0.0	0.0	0.0
1	4	934.00	934.00	934.00	934.00	934.00	934.00	0.0	0.0	0.0	0.0
2	1	0.0	0.0	0.0	0.0	0.0	0.0	2.6502700D-20	-3.3502630D-05	6.0195190D-16	-1.0168360D-06
2	2	100.63	-0.00	-0.00	0.0	0.0	0.0	-1.1773470D-22	5.0366630D-07	-1.6929230D-15	2.4264330D-06
2	3	0.0	0.0	135.19	97.52	135.19	0.0	-1.1811870D-21	-4.2099770D-04	-5.2251240D-14	1.6319760D-05
2	4	511.42	1526.62	971.96	934.00	971.96	1526.62	1.5307800D-19	-4.0338390D-03	2.9318280D-14	-1.1309210D-03
3	1	0.0	0.0	0.0	0.0	0.0	0.0	6.7002430D-19	-5.5255360D-05	-2.9363440D-14	7.8443430D-06
3	2	-271.45	0.00	0.00	0.0	0.0	0.0	1.3030320D-20	-1.3553220D-05	8.0797050D-14	3.4217190D-06
3	3	612.52	15.21	0.0	0.0	0.0	15.21	-3.9312070D-19	-5.1557740D-04	5.3508970D-14	-1.9269970D-04
3	4	0.0	1660.79	1505.65	511.42	1505.65	1660.79	-1.6216880D-19	-7.9775450D-03	-1.6972630D-11	-2.9714330D-05
4	1	109.77	0.00	0.00	0.0	0.0	0.0	1.1169630D-18	1.2627050D-04	-9.1403350D-15	-8.0446640D-07
4	2	-609.78	0.00	0.00	0.0	0.0	0.0	1.5703930D-20	-3.0519330D-05	1.8191910D-14	1.6090230D-05
4	3	1173.05	1465.92	933.78	612.52	933.78	1465.92	-3.2931290D-19	-8.6606010D-04	-6.8339750D-13	-4.3157100D-03
4	4	0.0	0.0	587.66	0.0	587.66	0.0	1.6349830D-19	-8.7933070D-03	1.0977510D-13	-5.6050550D-03
5	1	228.94	0.00	0.00	0.0	0.0	0.0	1.7221450D-18	1.2837490D-04	-3.4937310D-15	-1.7524720D-05
5	2	-443.49	0.00	0.00	0.0	0.0	0.0	8.7218370D-21	-2.8447010D-05	6.5133630D-15	5.1701950D-05
5	3	1712.41	1970.78	2145.53	1173.05	2145.53	1970.78	-4.3221410D-19	-1.1515130D-03	9.7149300D-13	-9.4671410D-03
5	4	0.0	0.0	145.07	0.0	145.07	0.0	5.6142240D-19	-5.0328360D-03	5.9566100D-13	-3.1102220D-03
6	1	-598.43	0.00	0.00	0.0	0.0	0.0	8.0274170D-19	-1.2872420D-04	-4.0038970D-15	-6.3133230D-05
6	2	1549.49	0.00	0.00	0.0	0.0	0.0	5.1541710D-21	7.7552110D-06	1.3185630D-14	1.5106920D-04
6	3	441.44	1811.26	2365.62	1712.41	2365.62	1811.26	-5.1019360D-19	-1.4130720D-03	-1.4925100D-12	2.1046750D-04
6	4	0.0	874.25	0.0	0.0	0.0	874.25	1.8652220D-19	-7.3009380D-03	-1.0099320D-12	-6.8882130D-03
7	1	529.00	0.00	0.00	0.0	0.0	0.0	3.7863310D-19	1.2837670D-04	9.5320770D-16	-2.2155610D-05
7	2	-327.48	0.00	0.00	0.0	0.0	0.0	1.0901330D-20	-1.6330170D-05	-1.6033160D-15	1.0329460D-04
7	3	1016.92	90.39	1462.49	441.44	1462.49	90.39	-3.3034200D-19	-1.6238700D-03	-4.7067860D-13	-1.0599070D-02
7	4	167.54	427.55	0.0	0.0	0.0	427.55	3.8556100D-19	4.8502720D-03	2.2284910D-13	-2.1061360D-02
8	1	478.95	0.00	0.00	0.0	0.0	0.0	5.5377640D-20	1.2812630D-04	4.3775760D-15	1.0620160D-04
8	2	-103.84	0.00	0.00	0.0	0.0	0.0	7.2450040D-21	-5.1970370D-07	-9.4176310D-15	-2.8901790D-04
8	3	0.0	0.0	149.89	1016.92	149.89	0.0	-2.5759010D-19	-2.0293220D-03	2.0777710D-13	-3.0263140D-03
8	4	1834.63	0.0	875.43	167.54	875.43	0.0	1.8133870D-19	1.0201080D-03	5.0111220D-13	-2.2541070D-02
9	1	168.56	0.00	0.00	0.0	0.0	0.0	3.0131140D-19	1.2657220D-04	1.1225190D-15	-1.1562200D-04
9	2	-2236.55	0.00	0.00	0.0	0.0	0.0	8.6075020D-21	-1.1193910D-05	-3.0776450D-15	2.0210330D-04
9	3	3703.34	973.54	0.0	0.0	0.0	973.54	-3.2943600D-19	2.2057930D-03	2.3560810D-15	9.9172220D-03
9	4	0.0	0.0	774.26	1834.63	774.26	0.0	2.2717520D-19	-3.0665720D-03	7.4626510D-13	-8.0700760D-03
10	1	-682.22	0.00	0.00	0.0	0.0	0.0	2.1411310D-18	-1.2914330D-04	-1.4295070D-16	1.8274000D-04
10	2	1282.65	-0.00	-0.00	0.0	0.0	0.0	-8.3568120D-20	6.4196910D-05	2.7872050D-16	-4.2073360D-04
10	3	2625.12	113.09	0.0	3703.34	0.0	113.09	3.6041650D-19	1.6569400D-03	4.5155050D-14	-3.8183430D-02
10	4	361.66	0.0	0.0	0.0	0.0	0.0	5.8431790D-17	2.4631520D-03	-5.9804370D-16	-1.1018800D-02

Table 2.3. Sample Computer Output - Reactivity Changes

REACTIVITY RESULTS: DUCT/WJ(J)/DK(J)

1	0.0	0.0	2	0.0	0.0	3	0.0	0.0	4	0.0	0.0
5	0.9299E 01	-0.5318E-01	6	0.3614E 01	0.2720E-01	7	0.0	0.0	8	-0.9637E 01	0.1293E 00
9	0.1738E 02	0.8937E-01	10	0.2955E 02	0.3962E 00	11	0.0	0.0	12	-0.1069E 02	-0.6142E-01
13	-0.1474E 02	0.6300E-01	14	-0.1540E 01	-0.2464E-01	15	0.0	0.0	16	0.0	0.0
17	0.0	0.0	18	0.0	0.0	19	0.0	0.0	20	0.6533E 02	-0.7450E 00
21	0.1860E 02	0.1212E 00	22	0.1048E 02	-0.5518E-01	23	0.7228E 01	-0.1134E 00	24	-0.8062E 02	-0.1339E 00
25	-0.1927E 02	-0.2137E 00	26	0.5911E 02	0.4663E 00	27	-0.2274E 02	-0.2397E 00	28	-0.2139E 02	-0.2533E-01
29	-0.1159E 03	-0.3411E 00	30	-0.2948E 02	0.1612E 00	31	-0.3080E 01	-0.5576E-01	32	0.0	0.0
33	0.0	0.0	34	0.0	0.0	35	0.9299E 01	0.1828E 00	36	0.1048E 02	-0.1393E-01
37	0.7228E 01	-0.1822E 00	38	-0.8062E 02	-0.2209E 00	39	-0.1927E 02	0.2062E 00	40	0.5911E 02	0.3712E 00
41	0.1530E 01	0.2881E-01	42	-0.2139E 02	0.8128E-01	43	-0.1159E 03	0.3871E 00	44	-0.2948E 02	0.5884E-01
45	-0.3080E 01	-0.4737E-01	46	0.0	0.0	47	0.0	0.0	48	0.0	0.0
49	0.3614E 01	-0.7480E-01	50	-0.8062E 02	-0.9315E-01	51	-0.1927E 02	0.1903E 00	52	0.3477E 02	0.4231E 00
53	0.5911E 02	0.1635E 01	54	0.1530E 01	0.1529E-01	55	-0.2139E 02	-0.1617E 00	56	-0.1159E 03	-0.4919E 00
57	-0.2948E 02	0.1292E 00	58	-0.3080E 01	-0.5368E-01	59	0.0	0.0	60	0.0	0.0
61	-0.9637E 01	0.9942E-01	62	0.3477E 02	0.4221E 00	63	0.5911E 02	0.7085E 00	64	0.1530E 01	0.2933E-01
65	-0.2139E 02	0.7106E-01	66	-0.1159E 03	0.6719E 00	67	-0.2948E 02	0.9786E-02	68	-0.3080E 01	-0.5017E-01
69	0.0	0.0	70	0.0	0.0	71	0.2955E 02	0.1134E 00	72	-0.2274E 02	-0.5225E 00
73	-0.2139E 02	0.1111E 00	74	-0.1159E 03	0.4678E 00	75	-0.2948E 02	0.1889E-02	76	-0.3080E 01	-0.4122E-01
77	0.0	0.0	78	0.0	0.0	79	0.0	0.0	80	-0.1159E 03	-0.4106E 00
81	-0.2948E 02	0.8035E-03	82	-0.3080E 01	-0.4091E-01	83	0.0	0.0	84	0.0	0.0
85	-0.1474E 02	0.2370E-01	86	-0.3080E 01	-0.4480E-01	87	0.0	0.0	88	0.0	0.0
89	0.0	0.0	90	0.0	0.0						

TOTAL REACTIVITY CHANGE= 0.3377E 01

Table 2.4 (a) Summary of Data Output at Beginning of Life, Full Power

SUMMARY AT TIME= 0., POWER= 1.00 (STEP NO. 1)

THERMAL BOW DISPLACEMENTS

HIGHEST						LOWEST					
ACLP			TLP			ACLP			TLP		
NO.	DISP	ANG	NO.	DISP	ANG	NO.	DISP	ANG	NO.	DISP	ANG
29	.0044	94	29	.0348	94	1	.0	88	1	.0	89
56	.0043	69	56	.0343	68	60	.0001	152	60	.0005	0
75	.0043	62	38	.0338	-146	33	.0001	-79	33	.0006	-79
52	.0043	58	50	.0333	21	70	.0001	65	70	.0008	65
67	.0042	60	75	.0330	77	11	.0001	62	11	.0009	59
9	.0042	60	67	.0328	0	47	.0001	0	78	.0011	66
38	.0042	-147	20	.0328	-120	78	.0001	66	47	.0011	103
20	.0042	-115	52	.0325	64	16	.0001	-120	16	.0012	87
50	.0042	16	24	.0324	59	84	.0002	95	84	.0013	98
13	.0041	122	9	.0323	122	36	.0002	83	36	.0014	83

TOTAL DISPLACEMENTS

HIGHEST						LOWEST					
ACLP			TLP			ACLP			TLP		
NO.	DISP	ANG	NO.	DISP	ANG	NO.	DISP	ANG	NO.	DISP	ANG
69	.0049	-109	66	.0245	38	1	.0	89	1	.0	67
32	.0049	58	74	.0237	89	19	.0001	56	62	.0004	33
59	.0049	67	29	.0228	88	2	.0004	89	12	.0005	93
58	.0048	95	56	.0226	59	3	.0006	89	11	.0006	94
31	.0048	0	75	.0205	-150	20	.0006	75	54	.0011	131
15	.0047	0	67	.0203	-98	4	.0009	88	35	.0012	47
46	.0046	88	85	.0202	133	13	.0011	63	40	.0015	90
70	.0044	95	81	.0202	-120	35	.0012	76	8	.0020	59
33	.0044	77	13	.0193	83	21	.0012	77	9	.0021	0
60	.0044	86	44	.0191	-159	5	.0013	89	52	.0024	-133

AVERAGE DUCT TEMPERATURES

HOTTEST DUCTS				COLDEST DUCTS			
ACLP		TLP		ACLP		TLP	
NO.	TEMP	NO.	TEMP	NO.	TEMP	NO.	TEMP
43	884.4	43	886.3	60	597.5	60	597.6
55	883.6	55	885.5	33	598.2	33	598.2
28	880.0	28	881.9	70	598.8	70	598.9
66	877.3	66	879.1	78	600.0	78	600.0
37	876.0	37	877.9	47	600.2	47	600.3
49	875.4	49	877.3	16	600.6	16	600.7
65	873.5	65	875.4	84	600.7	84	600.8
74	868.8	74	870.6	88	600.9	88	601.0
12	866.5	12	868.4	90	601.6	90	601.7
38	865.9	38	867.6	59	603.1	59	603.2

Table 2.4 (b)

SUMMARY AT TIME= 0., POWER= 1.00 (STEP NO. 1)

TOTAL CONTACT LOAD (N)

HEAVIEST LOADS

DUCT	NOZ.TIP	PIVOT	ACLP	TLP	TOTAL
35	753.	4016.	17494.	4401.	26663.
20	894.	4138.	17032.	4080.	26144.
37	1165.	4178.	15834.	3724.	24901.
50	362.	1601.	18574.	3095.	23633.
49	868.	3254.	15948.	2989.	23060.
38	200.	1838.	16517.	3219.	21773.
19	682.	3549.	7164.	8355.	19750.
23	797.	2400.	14209.	1848.	19254.
6	265.	1799.	12315.	3697.	18076.
21	145.	1629.	13601.	2283.	17658.

LIGHTEST LOADS

DUCT	TOTAL
57	3506.
30	3594.
27	4245.
45	4357.
14	4406.
76	4430.
79	4482.
82	4507.
86	4509.
68	4811.

PAD FACE LOAD (N)

HEAVIEST LOADS				LIGHTEST LOADS			
ACLP		TLP		ACLP		TLP	
DT/FCE	LOAD	DT/FCE	LOAD	DT/FCE	LOAD	DT/FCE	LOAD
52/1	5287.	51/1	3467.	90/6	0.	90/6	0.
53/4	5287.	52/4	3467.	90/3	0.	90/5	0.
20/2	5274.	3/2	3151.	90/2	0.	90/4	0.
35/4	5274.	3/6	3151.	90/1	0.	90/3	0.
35/5	5274.	20/5	3151.	89/6	0.	90/2	0.
9/1	4804.	8/1	2468.	89/5	0.	90/1	0.
10/4	4804.	9/4	2468.	89/4	0.	89/6	0.
37/2	4723.	51/2	2453.	89/3	0.	89/3	0.
50/5	4723.	62/5	2453.	88/6	0.	89/2	0.
37/1	4210.	41/1	2337.	88/3	0.	89/1	0.

Table 2.4 (c)

SUMMARY AT TIME= 0., POWER= 1.00 (STEP NO. 1)

NOZZLE BENDING STRESSES (PA)

NO.	HIGHEST STRESS	ANG	NO.	LOWEST STRESS	ANG
32	45528048.	90	85	0.	0
59	45448720.	0	43	0.	180
69	45244176.	180	29	0.	-180
33	43389920.	-180	3	0.	-180
70	43175744.	-180	2	0.	180
60	43033856.	0	1	0.	0
15	41516976.	180	13	533484.	0
46	41130512.	-180	44	754049.	0
16	39856128.	180	81	1829155.	0
47	39344144.	0	56	1921725.	0

ACLP MIDFLAT BENDING STRESSES (PA)

NO.	HIGHEST STRESS	NO.	LOWEST STRESS
9	107861888.	35	-105924608.
52	105920192.	53	-85160608.
19	92734544.	24	-84946128.
37	87620928.	38	-80641632.
62	86807648.	50	-79351360.
42	76132032.	72	-74041120.
65	72429456.	41	-66168096.
49	71944096.	51	-62715632.
73	71784496.	61	-60341312.
71	71757360.	21	-59491264.

ACLP CORNER BENDING STRESSES (PA)

NO.	HIGHEST STRESS	NO.	LOWEST STRESS
20	130925296.	22	-75469104.
24	75195936.	35	-70624288.
37	63776784.	42	-50716288.
19	61829872.	38	-45279296.
28	59569392.	61	-40231856.
23	59319920.	50	-34076640.
65	48136128.	51	-33459328.
49	47968016.	41	-30288240.
71	47843472.	85	-26310992.
63	33518544.	36	-24247040.

Table 2.5 (a) Summary of Data Output at End of First Fuel Cycle at Full Power

SUMMARY AT TIME= 255., POWER= 1.00 (STEP NO. 53)

THERMAL BOW DISPLACEMENTS

HIGHEST						LOWEST					
ACLP			TLP			ACLP			TLP		
NO.	DISP	ANG	NO.	DISP	ANG	NO.	DISP	ANG	NO.	DISP	ANG
67	.0037	61	67	.0284	0	1	.0	70	1	.0	71
75	.0037	0	75	.0279	77	11	.0000	-142	11	.0001	-86
81	.0035	85	29	.0269	66	60	.0001	0	60	.0005	-82
13	.0035	59	85	.0268	0	33	.0001	0	33	.0006	0
85	.0034	0	81	.0264	72	70	.0001	-120	70	.0008	-120
29	.0034	64	13	.0262	-120	47	.0001	0	78	.0011	-110
56	.0032	-142	56	.0257	-140	78	.0001	-120	47	.0011	0
44	.0032	0	44	.0238	-145	16	.0001	132	16	.0012	92
52	.0031	69	28	.0234	-120	36	.0002	77	36	.0013	59
9	.0031	-88	38	.0223	63	84	.0002	88	84	.0013	90

TOTAL DISPLACEMENTS

HIGHEST						LOWEST					
ACLP			TLP			ACLP			TLP		
NO.	DISP	ANG	NO.	DISP	ANG	NO.	DISP	ANG	NO.	DISP	ANG
69	.0025	25	29	.0176	74	1	.0	88	1	.0	86
15	.0022	88	85	.0170	59	19	.0000	85	35	.0000	167
70	.0021	52	75	.0169	-110	26	.0002	74	8	.0005	83
32	.0020	71	81	.0168	114	57	.0002	42	11	.0005	49
77	.0020	-120	67	.0168	88	20	.0003	72	6	.0011	89
68	.0020	8	56	.0166	-144	2	.0003	0	64	.0014	-116
87	.0020	0	13	.0159	61	4	.0003	89	61	.0017	-58
46	.0019	-120	44	.0152	60	85	.0003	-119	54	.0018	7
14	.0019	88	66	.0144	73	10	.0004	73	79	.0019	6
83	.0018	104	30	.0138	-120	35	.0004	32	51	.0019	0

AVERAGE DUCT TEMPERATURES

HOTTEST DUCTS				COLDEST DUCTS			
ACLP		TLP		ACLP		TLP	
NO.	TEMP	NO.	TEMP	NO.	TEMP	NO.	TEMP
37	870.3	37	872.1	60	597.5	60	597.6
49	869.2	49	871.1	33	598.2	33	598.2
38	862.4	38	864.1	70	598.8	70	598.9
50	857.5	50	859.3	78	600.0	78	600.0
35	857.5	35	859.3	47	600.2	47	600.3
23	856.4	23	858.2	16	600.6	16	600.7
55	855.7	55	857.4	84	600.7	84	600.8
43	855.6	43	857.4	88	600.9	88	601.0
65	851.7	65	853.4	90	601.6	90	601.7
66	851.5	66	853.2	59	603.8	59	603.9

Table 2.5 (b)

SUMMARY AT TIME= 255., POWER= 1.00 (STEP NO. 53)

TOTAL CONTACT LOAD (N)

HEAVIEST LOADS

DUCT	NOZ.TIP	PIVOT	ACLP	TLP	TOTAL
50	462.	792.	4948.	145.	6346.
38	588.	1050.	3828.	277.	5743.
20	897.	1572.	2884.	383.	5736.
35	885.	1306.	3476.	0.	5667.
37	774.	1143.	3588.	0.	5505.
49	556.	821.	3895.	0.	5272.
19	372.	1172.	2550.	944.	5037.
53	691.	1039.	2979.	32.	4742.
28	499.	1215.	1865.	1075.	4654.
24	906.	1678.	1334.	512.	4430.

LIGHTEST LOADS

DUCT	TOTAL
86	670.
39	692.
26	737.
25	773.
54	825.
76	840.
45	857.
11	897.
82	925.
14	1090.

PAD FACE LOAD (N)

HEAVIEST LOADS				LIGHTEST LOADS			
ACLP		TLP		ACLP		TLP	
DT/FCE	LOAD	DT/FCE	LOAD	DT/FCE	LOAD	DT/FCE	LOAD
9/1	1272.	51/1	765.	90/6	0.	90/6	0.
10/4	1272.	52/4	765.	90/2	0.	90/5	0.
52/1	1176.	8/1	659.	90/1	0.	90/4	0.
53/4	1176.	9/4	659.	89/6	0.	90/3	0.
50/3	1117.	67/1	598.	89/5	0.	90/2	0.
24/3	1073.	68/4	598.	89/4	0.	90/1	0.
38/6	1073.	68/1	556.	89/3	0.	89/6	0.
19/2	934.	69/4	556.	88/6	0.	89/3	0.
19/1	934.	27/1	523.	88/3	0.	89/2	0.
20/4	934.	28/4	523.	88/2	0.	89/1	0.

Table 2.5 (c)

SUMMARY AT TIME= 255., POWER= 1.00 (STEP NO. 53)

NOZZLE BENDING STRESSES (PA)

NO.	HIGHEST STRESS	ANG	NO.	LOWEST STRESS	ANG
69	19575984.	90	82	0.	0
70	17833728.	0	76	0.	0
24	16600398.	0	55	0.	0
20	16435413.	180	29	0.	0
35	16208275.	180	12	0.	180
32	14869470.	0	1	0.	0
37	14178520.	180	86	173197.	0
15	14000792.	-180	51	282428.	180
72	13862546.	180	62	313593.	0
23	13857890.	0	2	570820.	0

ACLP MIDFLAT BENDING STRESSES (PA)

NO.	HIGHEST STRESS	NO.	LOWEST STRESS
52	25156624.	67	-20113184.
9	24787616.	51	-20043232.
19	22707728.	10	-19471968.
62	14215290.	61	-17675952.
28	13117447.	75	-14712386.
12	12512141.	13	-14087367.
73	7346759.	30	-11691745.
79	6673358.	44	-11291557.
4	6356442.	57	-11231656.
5	6179466.	85	-10719530.

ACLP CORNER BENDING STRESSES (PA)

NO.	HIGHEST STRESS	NO.	LOWEST STRESS
28	17722320.	61	-11784819.
27	15593843.	85	-7146780.
19	15140155.	75	-6173282.
23	13540430.	73	-5142971.
24	13368495.	38	-4569604.
20	12275515.	72	-4449499.
21	6180146.	81	-3135391.
62	4862747.	67	-1847557.
79	4449652.	39	-1235541.
25	3655352.	53	-778927.

Table 2.6 (a) Summary of Data Output at Beginning of Second Fuel Cycle at Full Power

SUMMARY AT TIME= 255., POWER= 1.00 (STEP NO. 55)

THERMAL BOW DISPLACEMENTS

HIGHEST						LOWEST					
ACLP			TLP			ACLP			TLP		
NO.	DISP	ANG	NO.	DISP	ANG	NO.	DISP	ANG	NO.	DISP	ANG
75	.0040	73	71	.0306	70	1	.0	64	1	.0	-120
52	.0039	0	75	.0300	77	79	.0000	71	60	.0005	80
9	.0038	59	29	.0298	-179	60	.0001	142	79	.0005	84
71	.0038	70	56	.0293	87	33	.0001	81	33	.0006	81
81	.0038	0	81	.0284	0	70	.0001	65	70	.0008	0
29	.0038	179	67	.0284	0	11	.0001	0	11	.0008	67
67	.0037	0	52	.0281	69	47	.0001	-85	78	.0011	0
56	.0037	29	61	.0280	142	78	.0001	0	47	.0011	-64
61	.0037	80	49	.0276	58	16	.0001	-143	16	.0012	59
49	.0035	63	9	.0276	-120	84	.0002	88	84	.0013	59

TOTAL DISPLACEMENTS

HIGHEST						LOWEST					
ACLP			TLP			ACLP			TLP		
NO.	DISP	ANG	NO.	DISP	ANG	NO.	DISP	ANG	NO.	DISP	ANG
32	.0031	56	29	.0198	-134	1	.0	85	1	.0	87
69	.0031	-126	56	.0194	-149	19	.0001	69	35	.0001	-92
59	.0031	-105	75	.0186	147	39	.0002	89	8	.0004	81
46	.0031	58	66	.0185	153	20	.0002	59	65	.0004	-106
77	.0028	89	81	.0182	-89	13	.0003	89	6	.0008	59
58	.0028	79	85	.0181	-119	4	.0003	88	11	.0012	89
45	.0027	71	67	.0179	-1	11	.0004	58	21	.0019	84
33	.0026	58	44	.0175	59	2	.0004	87	62	.0019	-89
87	.0026	0	30	.0160	0	35	.0005	65	52	.0021	61
31	.0026	72	43	.0159	165	12	.0005	89	40	.0023	-120

AVERAGE DUCT TEMPERATURES

HOTTEST DUCTS				COLDEST DUCTS			
ACLP		TLP		ACLP		TLP	
NO.	TEMP	NO.	TEMP	NO.	TEMP	NO.	TEMP
43	879.1	43	881.0	60	597.5	60	597.6
55	878.0	55	879.9	33	598.2	33	598.2
50	869.2	50	871.0	70	598.8	70	598.9
28	865.5	28	867.3	78	600.0	78	600.0
37	864.2	37	866.1	47	600.2	47	600.3
74	861.4	74	863.1	16	600.6	16	600.7
72	858.9	72	860.7	84	600.7	84	600.8
65	858.0	65	859.8	88	600.9	88	601.0
66	857.8	66	859.5	90	601.6	90	601.7
38	857.5	38	859.2	59	603.8	59	603.9

Table 2.6 (b)

SUMMARY AT TIME= 255., POWER= 1.00 (STEP NO. 55)

TOTAL CONTACT LOAD (N)

HEAVIEST LOADS

DUCT	NOZ.TIP	PIVOT	ACLP	TLP	TOTAL
20	455.	2703.	8884.	3084.	15126.
35	1569.	3893.	6936.	2390.	14787.
50	412.	452.	10627.	1311.	12802.
49	1252.	3330.	5866.	2258.	12707.
37	1137.	2390.	7364.	1090.	11980.
61	276.	2003.	5831.	3700.	11810.
28	607.	1168.	5512.	2276.	9564.
19	449.	1553.	4672.	2878.	9552.
10	573.	2197.	4823.	1775.	9367.
3	283.	883.	2235.	5807.	9208.

LIGHTEST LOADS

DUCT	TOTAL
79	524.
12	873.
14	964.
13	1504.
82	1646.
86	1666.
39	1797.
27	1852.
76	1984.
85	1989.

PAD FACE LOAD (N)

HEAVIEST LOADS				LIGHTEST LOADS			
ACLP		TLP		ACLP		TLP	
DT/FCE	LOAD	DT/FCE	LOAD	DT/FCE	LOAD	DT/FCE	LOAD
9/1	2985.	11/2	1905.	90/6	0.	90/6	0.
10/4	2985.	11/6	1905.	90/3	0.	90/5	0.
52/1	2976.	28/5	1905.	90/2	0.	90/4	0.
53/4	2976.	3/2	1885.	90/1	0.	90/3	0.
20/3	2849.	3/6	1885.	89/6	0.	90/2	0.
20/2	2831.	20/5	1885.	89/5	0.	90/1	0.
35/5	2831.	51/1	1862.	89/4	0.	89/6	0.
35/4	2831.	52/4	1862.	89/3	0.	89/3	0.
37/2	2767.	10/1	1775.	88/6	0.	89/2	0.
50/5	2767.	11/4	1775.	88/3	0.	89/1	0.

Table 2.6 (c)

SUMMARY AT TIME= 255., POWER= 1.00 (STEP NO. 55)

NOZZLE BENDING STRESSES (PA)

NO.	HIGHEST STRESS	ANG	NO.	LOWEST STRESS	ANG
35	28730160.	90	79	0.	0
32	26329120.	0	51	0.	0
59	26011456.	0	30	0.	180
69	24860832.	180	26	0.	0
33	24362448.	180	12	0.	-180
60	23590288.	0	1	0.	0
70	23296160.	0	81	149835.	0
46	23088224.	-180	5	151264.	-180
49	22932912.	-180	74	1249040.	-180
47	22857136.	0	66	1455411.	0

ACLP MIDFLAT BENDING STRESSES (PA)

NO.	HIGHEST STRESS	NO.	LOWEST STRESS
52	56933856.	61	-58180048.
49	54043728.	35	-57517344.
9	50909104.	10	-56944384.
62	42493600.	53	-45165648.
71	39836320.	50	-36938560.
42	38143872.	51	-33111584.
28	33192928.	72	-30912896.
19	32477520.	24	-29668432.
4	32132176.	2	-29443152.
73	30538432.	41	-29301648.

ACLP CORNER BENDING STRESSES (PA)

NO.	HIGHEST STRESS	NO.	LOWEST STRESS
20	98963120.	61	-38791104.
28	67328432.	35	-38349168.
49	36033248.	36	-30048160.
71	26560400.	22	-24551392.
19	21654096.	62	-13162403.
37	18790960.	42	-12510334.
24	17747600.	81	-12231995.
23	14197978.	80	-10849196.
54	12510334.	75	-10831591.
25	11657708.	51	-10342230.

Table 2.7 (a) Summary of Data Output at End of Second Fuel Cycle at Full Power

SUMMARY AT TIME= 510., POWER= 1.00 (STEP NO. 107)

THERMAL BOW DISPLACEMENTS

HIGHEST						LOWEST					
ACLP			TLP			ACLP			TLP		
NO.	DISP	ANG	NO.	DISP	ANG	NO.	DISP	ANG	NO.	DISP	ANG
28	.0035	60	28	.0272	-120	1	.0	-142	1	.0	-142
75	.0034	62	75	.0250	77	11	.0000	0	11	.0001	91
67	.0032	15	67	.0240	0	79	.0000	71	79	.0004	84
81	.0032	77	10	.0237	82	60	.0001	61	60	.0005	-41
10	.0030	83	81	.0232	78	33	.0001	0	33	.0006	59
13	.0028	90	29	.0219	0	70	.0001	-155	70	.0008	-150
29	.0028	54	85	.0213	0	47	.0001	-122	78	.0011	0
85	.0028	0	56	.0207	61	78	.0001	0	47	.0011	84
52	.0028	-84	13	.0203	-83	16	.0001	-120	16	.0012	140
44	.0027	70	44	.0199	-21	84	.0002	59	84	.0013	59

TOTAL DISPLACEMENTS

HIGHEST						LOWEST					
ACLP			TLP			ACLP			TLP		
NO.	DISP	ANG	NO.	DISP	ANG	NO.	DISP	ANG	NO.	DISP	ANG
28	.0022	53	29	.0181	82	1	.0	52	1	.0	88
32	.0020	89	81	.0169	-152	19	.0001	29	35	.0004	76
12	.0020	79	75	.0166	48	4	.0001	49	2	.0010	59
43	.0020	81	56	.0166	62	20	.0001	59	3	.0010	62
16	.0018	89	85	.0163	60	35	.0001	59	11	.0010	93
69	.0018	-135	13	.0160	59	5	.0001	0	40	.0015	130
13	.0018	90	67	.0158	86	8	.0001	41	8	.0018	81
56	.0017	73	44	.0151	-68	51	.0002	86	62	.0019	177
59	.0017	59	30	.0143	76	2	.0002	89	7	.0020	66
29	.0016	56	66	.0138	59	26	.0002	43	51	.0022	42

AVERAGE DUCT TEMPERATURES

HOTTEST DUCTS				COLDEST DUCTS			
ACLP		TLP		ACLP		TLP	
NO.	TEMP	NO.	TEMP	NO.	TEMP	NO.	TEMP
50	866.1	50	868.0	60	597.5	60	597.6
22	861.4	22	863.8	33	598.2	33	598.2
53	860.6	53	862.5	70	598.8	70	598.9
37	858.5	37	860.3	78	600.0	78	600.0
5	854.0	5	855.9	47	600.2	47	600.3
38	853.9	38	855.6	16	600.6	16	600.7
49	850.8	49	852.6	84	600.7	84	600.8
43	850.4	43	852.0	88	600.9	88	601.0
55	850.0	55	851.7	90	601.6	90	601.7
26	849.2	26	850.9	59	604.5	59	604.6

Table 2.7 (b)

SUMMARY AT TIME= 510., POWER= 1.00 (STEP NO. 107)

TOTAL CONTACT LOAD (N)

HEAVIEST LOADS

DUCT	NOZ.TIP	PIVOT	ACLP	TLP	TOTAL
10	584.	1563.	2676.	1531.	6355.
28	263.	1007.	1905.	1261.	4436.
20	694.	1286.	1302.	421.	3703.
27	232.	423.	1135.	1257.	3046.
56	305.	450.	2148.	0.	2903.
66	662.	977.	1165.	0.	2804.
41	124.	228.	2368.	72.	2793.
23	411.	734.	1041.	566.	2752.
43	86.	127.	2526.	0.	2739.
53	200.	296.	2228.	0.	2724.

LIGHTEST LOADS

DUCT	TOTAL
25	121.
2	141.
54	190.
89	274.
1	322.
39	405.
46	474.
79	511.
45	520.
58	584.

PAD FACE LOAD (N)

HEAVIEST LOADS				LIGHTEST LOADS			
ACLP		TLP		ACLP		TLP	
DT/FCE	LOAD	DT/FCE	LOAD	DT/FCE	LOAD	DT/FCE	LOAD
28/2	1159.	10/2	611.	90/6	0.	90/6	0.
43/5	1159.	10/6	611.	90/5	0.	90/3	0.
9/1	1122.	27/5	611.	90/4	0.	90/2	0.
10/4	1122.	27/1	571.	90/3	0.	90/1	0.
27/3	1096.	28/4	571.	90/2	0.	89/6	0.
41/6	1096.	7/1	435.	90/1	0.	89/3	0.
41/3	1028.	8/4	435.	89/6	0.	88/6	0.
53/6	1028.	31/1	394.	89/5	0.	88/3	0.
8/1	1007.	32/4	394.	89/4	0.	88/2	0.
9/4	1007.	12/3	353.	89/3	0.	88/1	0.

Table 2.7 (c)

SUMMARY AT TIME= 510., POWER= 1.00 (STEP NO. 107)

NOZZLE BENDING STRESSES (PA)

HIGHEST NO.	HIGHEST STRESS	ANG	LOWEST NO.	LOWEST STRESS	ANG
16	14889982.	90	74	0.	0
32	14047630.	0	71	0.	0
20	12710222.	0	58	0.	0
33	12679615.	180	45	0.	-180
66	12118633.	-180	31	0.	-180
35	11818577.	0	30	0.	-180
69	11080482.	-180	26	0.	-180
59	11038730.	-180	13	0.	0
10	10699985.	-180	6	0.	0
73	10446672.	0	4	0.	0

ACLP MIDFLAT BENDING STRESSES (PA)

HIGHEST NO.	HIGHEST STRESS	LOWEST NO.	LOWEST STRESS
28	18072640.	10	-29524864.
8	17036448.	27	-9728185.
12	11321679.	57	-9374257.
5	9893571.	67	-9235347.
62	5864842.	14	-7488836.
39	3784005.	30	-6820667.
52	3557125.	38	-5867171.
71	2976169.	75	-5670379.
42	2426888.	82	-5399151.
80	2165393.	23	-5354875.

ACLP CORNER BENDING STRESSES (PA)

HIGHEST NO.	HIGHEST STRESS	LOWEST NO.	LOWEST STRESS
28	22118224.	62	-11439907.
27	21997664.	73	-5899431.
23	15891071.	36	-4848683.
20	12336252.	82	-4709845.
51	4166801.	76	-4301043.
40	3359065.	38	-4166801.
24	3082745.	26	-3359065.
71	1984332.	61	-2129832.
49	1097520.	63	-2022511.
19	1071573.	86	-1540751.

Table 2.8 (a) Summary of Data Output at End of First Fuel Cycle at Zero Power

SUMMARY AT TIME= 255., POWER= 0.0 (STEP NO. 11)

THERMAL BOW DISPLACEMENTS

HIGHEST						LOWEST					
ACLP			TLP			ACLP			TLP		
NO.	DISP	ANG	NO.	DISP	ANG	NO.	DISP	ANG	NO.	DISP	ANG
1	.0	0	1	.0	0	90	.0	0	90	.0	0
2	.0	0	2	.0	0	89	.0	0	89	.0	0
3	.0	0	3	.0	0	88	.0	0	88	.0	0
4	.0	0	4	.0	0	87	.0	0	87	.0	0
5	.0	0	5	.0	0	86	.0	0	86	.0	0
6	.0	0	6	.0	0	85	.0	0	85	.0	0
7	.0	0	7	.0	0	84	.0	0	84	.0	0
8	.0	0	8	.0	0	83	.0	0	83	.0	0
9	.0	0	9	.0	0	82	.0	0	82	.0	0
10	.0	0	10	.0	0	81	.0	0	81	.0	0

TOTAL DISPLACEMENTS

HIGHEST						LOWEST					
ACLP			TLP			ACLP			TLP		
NO.	DISP	ANG	NO.	DISP	ANG	NO.	DISP	ANG	NO.	DISP	ANG
29	.0015	13	65	.0083	73	1	.0	83	1	.0	62
74	.0015	78	73	.0079	93	19	.0000	91	10	.0000	59
72	.0015	72	24	.0073	-94	6	.0001	100	5	.0003	49
23	.0014	60	42	.0067	-174	35	.0001	89	49	.0004	-89
42	.0014	162	28	.0063	76	24	.0001	112	11	.0004	89
53	.0014	89	62	.0057	88	57	.0002	0	82	.0004	89
49	.0014	-45	23	.0050	-120	13	.0002	89	86	.0005	0
66	.0013	83	54	.0048	89	7	.0002	-120	45	.0005	-75
38	.0013	72	21	.0045	60	12	.0002	-101	68	.0005	79
54	.0012	77	19	.0044	98	4	.0003	-80	90	.0005	0

AVERAGE DUCT TEMPERATURES

HOTTEST DUCTS				COLDEST DUCTS			
ACLP		TLP		ACLP		TLP	
NO.	TEMP	NO.	TEMP	NO.	TEMP	NO.	TEMP
1	595.0	1	595.0	90	595.0	90	595.0
2	595.0	2	595.0	89	595.0	89	595.0
3	595.0	3	595.0	88	595.0	88	595.0
4	595.0	4	595.0	87	595.0	87	595.0
5	595.0	5	595.0	86	595.0	86	595.0
6	595.0	6	595.0	85	595.0	85	595.0
7	595.0	7	595.0	84	595.0	84	595.0
8	595.0	8	595.0	83	595.0	83	595.0
9	595.0	9	595.0	82	595.0	82	595.0
10	595.0	10	595.0	81	595.0	81	595.0

Table 2.8 (b)

SUMMARY AT TIME= 255., POWER= 0.0 (STEP NO. 11)

TOTAL CONTACT LOAD (N)

HEAVIEST LOADS

DUCT	NOZ.TIP	PIVOT	ACLP	TLP	TOTAL
20	1284.	1185.	1140.	1290.	4900.
38	1436.	1579.	677.	1105.	4797.
35	867.	330.	2059.	1439.	4694.
37	1087.	1060.	1093.	843.	4084.
50	1360.	1612.	339.	604.	3914.
24	1420.	1804.	0.	439.	3663.
28	1256.	1585.	25.	694.	3560.
3	276.	407.	2868.	0.	3552.
42	1235.	1528.	130.	434.	3326.
49	1027.	1113.	511.	610.	3261.

LIGHTEST LOADS

DUCT	TOTAL
88	0.
83	0.
60	0.
46	0.
47	0.
69	0.
16	0.
70	0.
78	0.
32	0.

PAD FACE LOAD (N)

HEAVIEST LOADS				LIGHTEST LOADS			
ACLP		TLP		ACLP		TLP	
DT/FCE	LOAD	DT/FCE	LOAD	DT/FCE	LOAD	DT/FCE	LOAD
35/2	1029.	35/4	719.	90/6	0.	90/6	0.
35/1	1029.	20/2	719.	90/5	0.	90/5	0.
36/4	1029.	35/5	719.	90/4	0.	90/4	0.
3/2	893.	37/1	545.	90/3	0.	90/3	0.
3/6	893.	38/4	545.	90/2	0.	90/2	0.
20/5	893.	28/1	367.	90/1	0.	90/1	0.
36/1	889.	29/4	367.	89/6	0.	89/6	0.
37/4	889.	52/1	327.	89/5	0.	89/5	0.
38/2	609.	53/4	327.	89/4	0.	89/4	0.
51/5	609.	71/1	321.	89/3	0.	89/3	0.

Table 2.8 (c)

SUMMARY AT TIME= 255., POWER= 0.0 (STEP NO. 11)

NOZZLE BENDING STRESSES (PA)

NO.	HIGHEST STRESS	ANG	NO.	LOWEST STRESS	ANG
38	26303552.	90	90	0.	0
24	26011264.	-180	89	0.	-180
50	24903360.	-180	88	0.	-180
20	23518624.	-180	87	0.	-180
28	23005040.	-180	84	0.	-180
42	22613264.	0	83	0.	0
72	22513936.	0	78	0.	0
65	20102352.	0	77	0.	0
37	19913024.	-180	70	0.	-180
49	18808704.	0	69	0.	0

ACLP MIDFLAT BENDING STRESSES (PA)

NO.	HIGHEST STRESS	NO.	LOWEST STRESS
35	34630864.	37	-22267088.
38	17719840.	71	-15469303.
50	14585734.	49	-14688215.
6	12242086.	52	-10482717.
29	11784173.	23	-9962537.
72	10929596.	20	-9455920.
53	10482717.	65	-8904750.
24	9716054.	42	-8827665.
10	7870365.	9	-7870365.
74	7743016.	28	-6817836

ACLP CORNER BENDING STRESSES (PA)

NO.	HIGHEST STRESS	NO.	LOWEST STRESS
35	23089728.	20	-32809808.
38	17979024.	28	-10483223.
42	10208493.	71	-10313957.
50	9588501.	49	-9793475.
22	7257531.	37	-9588501.
74	4047290.	23	-9236023.
72	1233569.	24	-8743003.
80	1212581.	65	-4047290.
43	274738.	19	-2914733.
1	0.	63	-1233569.

Table 2.9 (a) Summary of Data Output at Beginning of Second Fuel Cycle at Zero Power

SUMMARY AT TIME= 255., POWER= 0.0 (STEP NO. 11)

THERMAL BOW DISPLACEMENTS

HIGHEST						LOWEST					
ACLP			TLP			ACLP			TLP		
NO.	DISP	ANG	NO.	DISP	ANG	NO.	DISP	ANG	NO.	DISP	ANG
1	.0	0	1	.0	0	90	.0	0	90	.0	0
2	.0	0	2	.0	0	89	.0	0	89	.0	0
3	.0	0	3	.0	0	88	.0	0	88	.0	0
4	.0	0	4	.0	0	87	.0	0	87	.0	0
5	.0	0	5	.0	0	86	.0	0	86	.0	0
6	.0	0	6	.0	0	85	.0	0	85	.0	0
7	.0	0	7	.0	0	84	.0	0	84	.0	0
8	.0	0	8	.0	0	83	.0	0	83	.0	0
9	.0	0	9	.0	0	82	.0	0	82	.0	0
10	.0	0	10	.0	0	81	.0	0	81	.0	0

TOTAL DISPLACEMENTS

HIGHEST						LOWEST					
ACLP			TLP			ACLP			TLP		
NO.	DISP	ANG	NO.	DISP	ANG	NO.	DISP	ANG	NO.	DISP	ANG
23	.0017	22	65	.0083	93	1	.0	-82	1	.0	62
74	.0015	78	73	.0080	60	4	.0001	87	11	.0001	-26
38	.0015	-120	71	.0076	56	13	.0001	59	8	.0003	84
53	.0014	80	42	.0074	-79	56	.0001	86	82	.0004	79
72	.0014	75	35	.0074	125	12	.0001	97	45	.0005	-89
22	.0013	48	24	.0073	-87	49	.0002	-89	86	.0005	0
37	.0013	-89	52	.0072	92	57	.0002	84	68	.0005	67
66	.0013	60	40	.0065	89	8	.0002	82	90	.0005	0
41	.0012	91	9	.0060	89	30	.0002	91	78	.0005	80
40	.0012	117	21	.0056	47	7	.0002	-94	70	.0005	68

AVERAGE DUCT TEMPERATURES

HOTTEST DUCTS				COLDEST DUCTS			
ACLP		TLP		ACLP		TLP	
NO.	TEMP	NO.	TEMP	NO.	TEMP	NO.	TEMP
1	595.0	1	595.0	90	595.0	90	595.0
2	595.0	2	595.0	89	595.0	89	595.0
3	595.0	3	595.0	88	595.0	88	595.0
4	595.0	4	595.0	87	595.0	87	595.0
5	595.0	5	595.0	86	595.0	86	595.0
6	595.0	6	595.0	85	595.0	85	595.0
7	595.0	7	595.0	84	595.0	84	595.0
8	595.0	8	595.0	83	595.0	83	595.0
9	595.0	9	595.0	82	595.0	82	595.0
10	595.0	10	595.0	81	595.0	81	595.0

Table 2.9 (b)

SUMMARY AT TIME= 255., POWER= 0.0 (STEP NO. 11)

TOTAL CONTACT LOAD (N)

HEAVIEST LOADS

DUCT	NOZ.TIP	PIVOT	ACLP	TLP	TOTAL
38	1576.	1844.	658.	1073.	5151.
37	1271.	1559.	853.	522.	4204.
24	1487.	1889.	0.	455.	3830.
35	1253.	1475.	365.	643.	3735.
49	808.	1027.	1014.	252.	3101.
42	1125.	1422.	21.	363.	2931.
23	1009.	1233.	277.	390.	2909.
65	1102.	1397.	62.	342.	2902.
51	797.	1177.	616.	0.	2590.
73	891.	1144.	62.	243.	2340.

LIGHTEST LOADS

DUCT	TOTAL
15	0.
60	0.
69	0.
33	0.
87	0.
90	0.
59	0.
77	0.
88	0.
84	0.

PAD FACE LOAD (N)

HEAVIEST LOADS				LIGHTEST LOADS			
ACLP		TLP		ACLP		TLP	
DT/FCE	LOAD	DT/FCE	LOAD	DT/FCE	LOAD	DT/FCE	LOAD
37/3	507.	37/1	522.	90/6	0.	90/6	0.
49/6	507.	38/4	522.	90/5	0.	90/5	0.
49/3	507.	24/3	308.	90/4	0.	90/4	0.
38/2	436.	38/6	308.	90/3	0.	90/3	0.
51/5	436.	35/4	284.	90/2	0.	90/2	0.
3/2	327.	20/2	284.	90/1	0.	90/1	0.
3/6	327.	35/5	284.	89/6	0.	89/6	0.
20/5	327.	23/2	243.	89/5	0.	89/5	0.
10/1	270.	38/5	243.	89/4	0.	89/4	0.
11/4	270.	65/1	239.	89/3	0.	89/3	0.

Table 2.9 (c)

SUMMARY AT TIME= 255., POWER= 0.0 (STEP NO. 11)

NOZZLE BENDING STRESSES (PA)

NO.	HIGHEST STRESS	ANG	NO.	LOWEST STRESS	ANG
38	28870064.	90	90	0.	0
24	27232832.	-180	89	0.	-180
37	23276368.	-180	88	0.	-180
35	22947200.	-180	87	0.	-180
42	20611872.	-180	84	0.	-180
65	20176048.	0	83	0.	0
23	18481488.	0	79	0.	0
73	16311275.	0	78	0.	0
19	15056421.	-180	77	0.	-180
49	14803348.	0	70	0.	0

ACLP MIDFLAT BENDING STRESSES (PA)

NO.	HIGHEST STRESS	NO.	LOWEST STRESS
38	15719462.	37	-16755951.
35	13667971.	65	-9311769.
24	9653281.	42	-8762184.
6	8807689.	23	-8616792.
66	7307698.	73	-7163837.
74	7193513.	9	-6637259.
10	6637259.	19	-6174472.
43	5873495.	49	-6070750.
53	5226718.	52	-5226718.
29	4869505.	71	-5135374.

ACLP CORNER BENDING STRESSES (PA)

NO.	HIGHEST STRESS	NO.	LOWEST STRESS
38	17675440.	24	-9874325.
35	9112954.	20	-9112971.
22	6741971.	23	-7801127.
42	5778015.	28	-5778015.
74	3309352.	19	-4116766.
61	2678506.	49	-4047593.
80	1294319.	71	-3423958.
1	0.	65	-3309352.
2	0.	50	-2678506.
3	0.	73	-1294319.

3.0 SEISMIC ANALYSIS OF A FREE-FLOWERING HETEROGENEOUS, LMFBR CORE

3.1 INTRODUCTION

The seismic analysis of fast reactor core structures is a complex problem involving the dynamic interaction of many hundreds of individual fuel, blanket, and reflector assemblies in a fluid environment. The designer requires information about the magnitude and frequency of displacements of control assemblies, stresses in duct walls, impact loadings from the collision of adjacent assemblies, and possible adverse reactivity effects. Because the problem involves a large number of assemblies which cannot be analyzed individually due to their strong interaction and because of lack of adequate models of impacts in fluids and fluid-structure interaction between closely spaced hexagons, previous fast reactor core seismic analyses have been quite simplistic. Argonne has recently developed a special purpose computer program, SCRAP, to address these problems[8]. The SCRAP code has been under development since 1976 including extensive efforts in developing fluid coupling coefficients for closely packed arrays of hexagons, experimental study of impacting blocks in fluid, development of impact modeling methods, verification studies and modeling sensitivity studies. Several aspects of the SCRAP development program are not yet complete, particularly in the area of impact modeling in a fluid, but at this point there is a reasonable degree of confidence in the reliability of the code. This study is the first comprehensive study of a reactor design using the SCRAP code with the full fluid coupling models. It is also, to the best information of the authors, the first reported time history analysis of the seismic response of an LMFBR core including these important fluid effects.

The purpose of this portion of the report is to present the SCRAP code analysis and to determine the aseismic feasibility of using a free-flowering core restraint design for a commerical size LMFBR with a heterogeneous core. A free-flowering core restraint design does not have a restraining boundary to limit the core motion during an earthquake and some observers have felt that the seismic response of such a core would not be acceptable. The results of this study indicate that it is probably feasible, from a seismic viewpoint, to use a free-flowering core restraint design. Some uncertainty remains because of limitations

in the modeling of impacts between assemblies at the load pads. The final section gives the detailed conclusions of this study.

3.2 DESIGN DESCRIPTIONS

3.2.1 The Base Core Design (D-2)

The basic core restraint design philosophy under study was a free-flowering restraint with features similar to the Phenix and EBR-II reactors; this contrasts with the "limited-free-bow" core restraint concept used in the FTR and CRBRP designs. The core is heterogeneous with a total of 883 assemblies; 330 fuel assemblies, 331 blanket assemblies, 198 radial reflector assemblies, and 24 control assemblies. Each assembly is 4.75 m (15.58 ft) in length including a 1 m (3.28) nozzle which is imbedded in a grid plate support structure. The assemblies are arranged on a triangular pitch of 0.15 m (5.91 in). Figure 3.1 gives the structural properties for the fuel and blanket assemblies. The mass per unit length ρA, is an average for blanket and fuel assemblies. Figure 3.2 gives the structural properties for the radial reflector assemblies which are considerably stiffer.

The isothermal clearances between straight assemblies are 0.5 mm (0.020 in) at the ACLP and 4.0 mm (0.157 in) at the TLP. The ACLP clearance was chosen to give approximate closure of this gap at operating temperature while the TLP clearance was chosen to give maximum freedom for bowing of the assembly. The clearance at the upper end of the nozzle is zero but the lower end has a diametral clearance of 0.25 mm (0.010 in). This allows a free rotation of the assembly top of ±0.47 mm (±0.019 in).

The assembly bending stiffness is governed primarily by the duct wall thickness of 2.00 mm (0.079 in) which was specified by the core neutronics analysis. The stiffness in the shield portions of the assemblies, the nozzle sections, and the radial reflector assemblies were chosen as large as possible so that creep relaxation of assembly bowing interaction would be maximized.

The load pad stiffness at both the TLP and ACLP, were chosen small, 2×10^7 N/m (1.14×10^5 lb/in), for the fuel, blanket and control assemblies to avoid excessive local load pad forces. The load pads on the radial reflector assemblies are stiff, 2×10^9 N/m (1.14×10^7 lb/in), compatible with a solid assembly.

This design allows as much space as possible for bowing of assemblies without interaction and encourages creep relaxation of that interaction when it does occur. From an aseismic design view, there was an initial concern that the unconstrained top-end may have excessive motion during a seismic event and that the large clearances may lead to excessive impact loads between assemblies. As the results of the study show, the initial concern was unwarranted. This design is referred to as D-2 in the report.

3.2.2 The Scoping Design (D-1)

Prior to consideration of the design described in the previous section, a preliminary scoping study based on a limited free-flowering core restraint system was studied. This scoping study differed from the base case design in the following particulars:

a. The nozzle was only 0.6 m (23.6 in) in length.
b. There was zero diametral clearance at the lower nozzle support.
c. The across flats dimension at the TLP for all assemblies was 149.5 mm (5.886 in) leaving an isothermal clearance of 0.5 mm (0.020 in).

This scoping design was intended to allow less clearance in order to reduce impact loads during seismic events; it is designated D-1 in this report. The nozzle clearance and length used are probably impractical but are also not significant to the seismic response.

3.3 MODELING ASSUMPTIONS

The analysis was done using the SCRAP computer code[8,9] which performs a time history solution of an assumed mode model subject to a specified grid plate support motion. The important factors are the assumed modes of deformation allowed in the particular model, the physical phenomena that are modeled including the parameters in those models, and the input support motions studied.

3.3.1 The Assumed Modes

In this study the cluster mode approach was used with SCRAP to define the deformation field for the model. Seventeen clusters were identified symmetric about the y axis, Fig. 3.3, and each was allowed three modes of deformation in the y direction for a total of 51 degrees of freedom for the model.

Clusters #1, #2, #3, #13, #16 and #17 consist of radial reflector assemblies and have the properties from Fig. 3.2. The remaining clusters have nearly equal numbers of blanket and fuel assemblies and use the structural properties of Fig. 3.1. The deformation modes for each cluster were the first three free-vibration modes for the cluster. These were determined as a series solution of trigonometric functions which satisfy the geometric boundary conditions for the cluster. Five terms were included in the series with the coefficients determined by the Rayleigh-Ritz method. Fifty-one points were used in the numerical integration of the trigonometric generating functions both in the Rayleigh-Ritz approximation to the free-vibration modes and in the assumed mode model generation.

For the base case, D-2, the first mode of each cluster is a rigid body rotation about the pinned upper nozzle support and the next two modes are bending modes. For the preliminary case, D-1, all three modes of each cluster are bending modes since two points on the nozzle are fixed.

The clusters were chosen to give some indication of the effect of cluster size on the response of the model. Note clusters #1 and #16 are identical but #1 has a finer mesh of neighboring clusters than #16.

3.3.2 The Physical Phenomena Modeled

The following phenomena are considered in the energy functionals used in generating the assumed mode model:

a. Structural stiffness. Each assembly is considered a Bernouli/Euler beam with uniform properties over each segment. The segment lengths, and section moments are given in Figs. 3.1 and 3.2. The support plate is considered rigid for this analysis.

b. Structural mass. The assembly segment mass densities are given in Figs. 3.1 and 3.2.

c. Fluid inertia. The kinetic energy of the interassembly sodium coolant is modeled using fluid coupling coefficients for the thirty-six neighbors of each assembly. These coefficients are based on extensive finite element analysis of fluid coupling between closely spaced hexagons using both potential flow and linearized Novier-Stokes models of the fluid structure interaction[10]. The mass density of the sodium was 845 kg/m^3.

d. Fluid damping. The energy dissipated due to interassembly coolant viscous effects is modeled using fluid damping coefficients linking each assembly with 18 neighbors. These coefficients are based on the same finite element studies using linearized Novier-Stokes equations[10].

e. Structural damping. The SCRAP code uses proportional damping in generating a damping matrix due to the deformation of the assembly beam elements. For this study the damping was 2% of critical for all assemblies.

f. Interassembly gap and stiffness. The SCRAP code models contact between clusters with compression only gap elements which provide a force proportional to the relative position of two clusters, a gap stiffness, and a force proportional to the relative velocity of the two clusters, the impact damping force. For a heavily bowed core such as the heterogeneous core, most clusters are in contact with their neighbors through some of the assembly load pads. The gap stiffness was chosen to be the individual load pad stiffness (see Figs. 3.1 and 3.2) times the number of load pads in contact in the given direction at that axial location. The interference (or negative gap) between clusters is determined by dividing the force transmitted through the load pads in contact by the gap stiffness. In those instances where a cluster was not in contact with a neighbor in the equilibrium state at a given axial load level in a given direction, the gap was taken to be the average of the gaps between all the corresponding faces and the stiffness was the load pad stiffness times the total number of load pads involved. The calculation of these gap states and stiffnesses requires an equilibrium solution for the bowed reactor core such as is given by the NUBOW-3D code.

g. Impact damping. The damping parameter for each impact gap element was taken to give 20% of critical damping for a two mass system connected by the gap stiffness. The masses were chosen to be proportional to the masses of the clusters involved. Critical damping of 20% corresponds to a coefficient of restitution of 0.7.

h. Assembly bowing. Assembly bowing occurs due to thermal gradients, swelling gradients, and irradiation creep. The equilibrium state of the core, under given bowing conditions, is the initial state for a seismic analysis. Two states were considered: 1) an unbowed state in which all assemblies were straight, all clearances between assemblies were equal, and no loads occurred at equilibrium; 2) a bowed state corresponsing to full power at 225 full power days after loading of a virgin core (i.e., EOIC). The bowed equilibrium state for the latter case was obtained from a NUBOW-3D solution, as discussed in Chapter 2.

3.3.3 The Support Motion

The reactor vessel and core support structure, in series with the reactor building, act as a mechanical filter/amplifier of the ground motion due to a seismic event. As a result, the core sees a narrow band amplified input; the exact characteristics of this input depend to some extent on the nature of the earthquake but to a much larger extent on the design of the building and particularly the support of the reactor vessel. We have chosen, arbitrarily, a center frequency of 6 Hz and a peak acceleration of 1.0 g. as the primary input motion for this study. Moreover, most of the numerical simulations used a 6 Hz, 1 g. peak acceleration sinusoid for the support motion since this produced maximum response in a shorter dynamic simulation. One calculation was done with a time history generated to match a narrow band response spectrum centered at 6 Hz. Figure 3.4 gives a time trace of this acceleration.

3.4 BASE CASE SOLUTIONS

In this section the response of the base case design (D-2) with all of the modeling assumptions discussed in Section 3.2 subject to a 1 g. 6 Hz sinusoidal base motion is described. The SCRAP timestep used in the calculations was 0.32 ms, which was found to give stable and accurate solutions for this mode. The graphics output used 900 samples at 2.22 ms intervals to plot the first 2.0 s of response. Three measures of response are examined: displacement histories, bending stress histories, and impact loads at load pads and nozzle restraints.

3.4.1 Displacement Time Histories

Figures 3.5-21 depict the time history of the displacement at the TLP of the seventeen clusters of assemblies. Superposition of the graphs on a light table was used to study relative displacement of neighboring clusters. All of the graphics routines in the SCRAP code are self scaling; this results in some difficulty in comparing plots at different locations but for this case fifteen of the seventeen histories have the same time scale. The observations from the superposition of the displacement revealed:

a. strongly coherent motion of the central clusters (#4 through #15 with a strong frequency component of 6 Hz, the base motion frequency)
b. substantially more rattling of the edge clusters at either end (#1, #2, #3, #16, and #17).
c. somewhat greater amplitude of motion of the central clusters (~15 mm peak to peak). Note that #13 (reflector assemblies) moves with the frequency of a central cluster but at the amplitude of the edge clusters.
d. impacts observable as abrupt changes in the displacement history, e.g. clusters #4 through #9 all clearly show a major collision occurring at about 0.455 s. Many more impacts occur which are not nearly so discernible; these can be identified by superposition of the time history graphs on a light table.

Figures 3.22-27 contain time histories of the ACLP displacements for clusters #1, #2, #4, #7, #8, and #10. They show basically the same properties as the TLP displacement, i.e. coherent motion with larger amplitude 6 Hz response in the central region, (Figs. 3.24-27) and higher frequency smaller amplitude response in the reflectors (Figs. 3.22 and 23). This indicates that most of the displacement is governed by the first two modes (rigid body rotation and first bending). Some third mode response is evident by the difference between ACLP and TLP displacement for cluster #4 (Figs. 3.24 and .8) at 0.5 seconds.

3.4.2 Bending Stress Response

The bending stress time history response plotted in Figs. 3.28-38 is calculated by the relation

$$\sigma = \frac{My}{I} = w'' E y$$

where M is the bending moment given by the second spacial derivative of the

displacement, w", times the section modulus EI, I is the 2nd moment of area of the section, E is Young's modulus, and y is the distance from the neutral axis to the extreme fiber. The value of E y for the assembly ducts is 1.37×10^{10} N/m. Figures 3.28-34 give histories of the bending stress at about the mid-core elevation. While the bending stress shows somewhat more higher frequency content than the displacement because the second derivative amplifies higher frequencies, the behavior is essentially the same as the displacement histories. The central region is dominated by coherent second mode (first bending mode) response and has higher peak stresses. The reflector assemblies (except for cluster #13) have more high frequency response and lower peak stresses.

Figures 3.35-38 give bending stress histories for clusters #1, (reflector assemblies) and #10, (center core assemblies) at the ACLP and at the top of the lower axial shield. These indicate that the peak bending stresses occur below the core and are dominated by the first bending mode contribution. The largest bending stress observed was 37 MPa at 0.3 s in cluster #10 at 0.6 m above the support plate; a more detailed study of the axial variation of bending stress was not conducted.

3.4.3 Impact Loading Histories

Figures 3.39-47 give time histories of impact forces at several TLP, ACLP, and nozzle locations. In each figure the force is the total force between two clusters (or between the cluster and the support plate for nozzles) at the given load pad on the faces in the given direction. In all cases the y direction (i.e., the direction of the support motion) was used. The average force on an individual load pad is obtained by dividing the value of the force in the figure by the number of faces given in the figure caption.

The peak impact forces have the most uncertainty of all the response measures examined. The dynamics of the core structure is governed primarily by the total impulse at each impact and is rather insensitive to the shape (peak and time duration) of the impacts. The impact model currently used in SCRAP does not account for the increasing fluid pressure on the load pad prior to closing the gap. As a result, the peak impact forces in our model must be higher during the closed gap portion of impact to result in the same total impulse. Another problem with the impact forces lies with the sampling time of 2.22 ms for the graphics routines. It is possible, particularly for the sharp impacts occurring at the reflectors, that the peak impact forces are underestimated because of the coarse sampling of

the solution. With these caveats in mind we examine the impact forces at a few locations.

The largest impact forces occur at the reflector radial blanket boundary (Figs. 3.39-.41). This is expected because the largest relative displacements occur here and the reflector load pads are stiffer, resulting in an impulse with shorter duration and higher peak force. In the central core region the contact forces are of longer duration with smaller amplitude, which is compatible with softer load pads and coherent motion. The largest peak force observed on the face of a cluster #10 assembly was 10.4 kN (3822 lb) at the TLP, 7.2 kN (1619 lb) at the ACLP, and 3.4 kN (764 lb) at the nozzle. Peak impact forces observed at the reflector boundary were 26 kN (5845 lb) at the TLP and 17 kN (3822 lb) at the ACLP.

3.5 SENSITIVITY STUDIES

3.5.1 Studies Based on the D-2 Design

In addition to the base case which was discussed in detail in Section 3.4, several other cases were studied to determine the sensitivity of the core response to the modeling assumptions and support motion input. Rather than present the detailed time history response for these cases, the key results were summarized in a bar chart form. The response measures chosen for comparison are:

1. The TLP maximum peak-to-peak displacement during a 2 second simulation for clusters #1, #8, #10, and #16.

2. The maximum bending stress during a 2 second simulation for clusters #1, at the top of the lower shield (1.6 m) and for cluster #10 at the top of the lower shield (1.6 m), mid-core (2.35 m), and the ACLP (3.1 m).

3. The peak impact force during the 2 second simulation at the TLP between clusters 8-10, 10-14, and 1-4, and at the ACLP between clusters 8-10 and 1-4.

In each of the sensitivity studies, the model of the core system was the same as the base case with the exception that the core was not bowed. At the time the sensitivity calculations were conducted the procedure for including the results of a NUBOW-3D bowing calculation in the SCRAP code had been completed so that the equilibrium state corresponded to straight assemblies at operating temperature. This means that at equilibrium there are gaps between each cluster in every direction and the load pad springs always correspond to the number of faces in the gap direction.

In the first series of simulations, the sensitivity of the response measures to variations in the amplitude of the base motion was investigated. Input amplitudes of 0.2 g, 0.6 g, 1.0 g, 1.2 g and 1.5 g, all at 6 Hz, were investigated and the results are given in Figs. 3.48-50 along with the corresponding response measures for the base case. We find that TLP peak-to-peak displacement and peak bending stress are quite linear with input amplitude while peak impact force behaves in a nonlinear fashion. The latter might be expected since the nonlinearities in the model are associated with the impact gaps which are directly involved in the impact force calculation.

This simulation also provides insight into the effect of assembly bow on seismic response by comparing the base case with the 1.0 g case since the only difference between these cases is the inclusion of assembly bow in the base case. Bowing of the core, in general, reduces the response measures although the bending stress of the outer cluster, #1, is increased. This is due to the equilibrium bending stress in these assemblies in the bowed state which is not present with straight assemblies. The equilibrium stress is observed as the positive bias in the bending stress history for this assembly, (Fig. 3.36). The second sensitivity series consisted of varying the input support frequency at a constant 1.0 g amplitude. Figures 3.51-53 give the results of this study and it is readily seen that displacement and bending stress appear to resonate at low frequency. In addition, there appears to be some tendency for increased response at 10 Hz. The picture for peak impact force is generally the same in the central core region but out near the reflectors the behavior is more complex. The maximum impact force varies between the ACLP and TLP for different frequencies and is proportionately less sensitive to input frequency while being substantially more erratic.

Next a series of simulations was run to determine the effect of the various physical phenomena included in the model. Figures 3.54-56 summarize the results of this study. The inertia of the interassembly fluid has the strongest effect in reducing all of the response parameters. Impact damping, structural damping, and assembly bow have a moderate effect in reducing TLP peak-to-peak displacement but a more pronounced effect in reducing bending stress and peak impact force. Interassembly fluid damping due to relative motion of the assembly flow ducts between load pads appears to have negligible effect on the core seismic response.

3.5.2 Studies Based on the D-1 Design

Finally, early in the study several simulations of the first design iteration were performed. Design D-1 had considerably less freedom to displace than D-2, and TLP displacements were 40% less in the mid-core region for design D-1. The coherence of the motion and frequency of the response were similar to the D-2 case, but the rattling of the reflector assemblies did not occur in this design. This is probably because the reduced clearance at the TLP does not allow as much relative motion so that large impacts do not occur to excite the rattling of the reflectors. Bending stresses in the reflector assemblies of the D-1 design were comparable to those for D-2, but bending stresses in the central core region were reduced by a factor of 10. Peak impact forces were generally lower for the D-1 design by a factor of 4, although the first impact at the blanket-reflector interface (clusters 1-4) was as large as the D-2 design impacts.

A simulation using a narrow band seismic support motion, Fig. 3.4, was run for 3.5 s using the D-1 design. The peak acceleration for this time interval was only 0.5 g and the response measures were correspondingly lower but the basic behavior of the core was the same as for the sinusoidal support motion. The response followed the amplitude and frequency of the support motion and was coherent. The TLP displacement for cluster #10 is given in Fig. 3.57 as an example.

3.6 CONCLUSIONS

The purpose of this study was to evaluate the effect of seismic disturbance on the feasibility of a free-flowering core restraint design. The answer to that question for a specific plant requires detailed design requirements for such items as control rod drive line misalignment, structural reactivity insertion, assembly stress allowables, etc. These system design requirements were not available for this study. The study shows that if the following four conditions are allowable, there is no inherent reason why a free-flowering core restraint design of the type considered in this study cannot be designed to withstand seismic disturbances. The conditions are:

1. A building, vessel, and core support system can be designed to provide support plate motions with peak accelerations of no more than 1.0 g and with little frequency content below 5 Hz. The design and support of the reactor vessel as well as the manner in which the core is supported in the vessel must be considered early in the design process to avoid excessive amplification of the seismic motion at core support.

2. A control rod drive system can be designed to accept 25 mm (1 in) peak-to-peak misalignment at the fundamental frequency of the core support motion. The magnitude of the TLP displacements at control rod positions can be controlled somewhat by varying the stiffness of the assemblies and the load pad gap between assemblies.

3. Assemblies can be designed to allow additional bending stress due to the seismic event of the order of 50 MPa (7.24 ksi). The peak bending stress is closely related to TLP displacements and some improvements might be made by allowing less freedom (available gap) in the design but this is likely to be countered by increased bowing stress during normal operation. Little improvement in this condition is likely without reducing the support motion during a seismic event.

4. Assemblies can be designed with soft load capable of withstanding impacts with peak forces of 50 kN (11,250 lb) and hard (solid) load pads capable of withstanding 200 kN (45,000 lb). This condition is probably quite conservative; that is, the 50kN and 200 kN peak force might be reduced substantially with improved modeling of the load pad impact. The 50 kN and 200 kN figures reflect the uncertainty of the impact model, which does not include fluid cushioning, and the variability of the peak forces observed in the study.

Finally, while no calculations of reactivity time histories were attempted in this study, the strong coherence of the motion in the central core region indicates that reactivity effects should not be limiting for this free-flowering design.

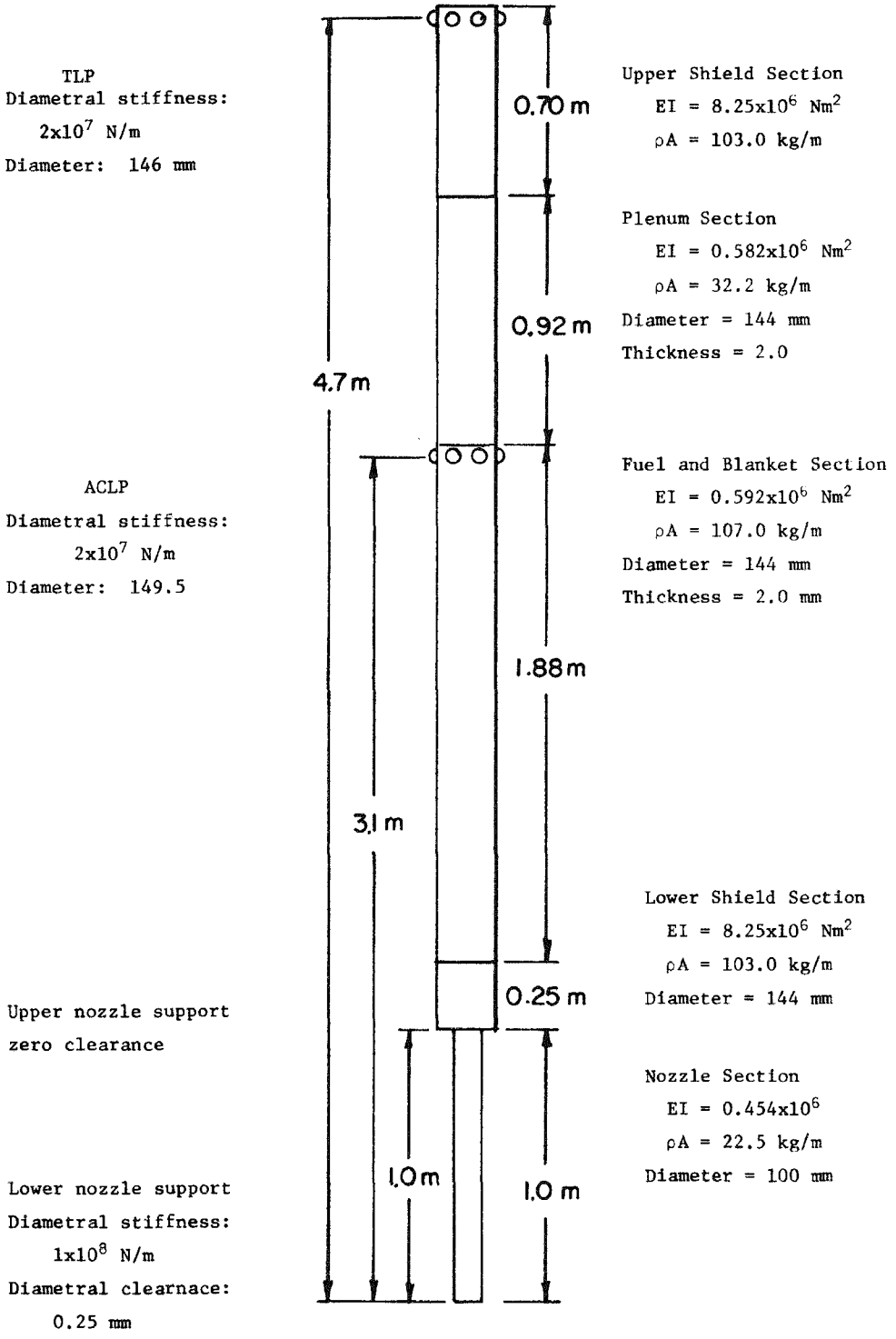

Fig. 3.1. Fuel and Blanket Assembly Description for Design D-2

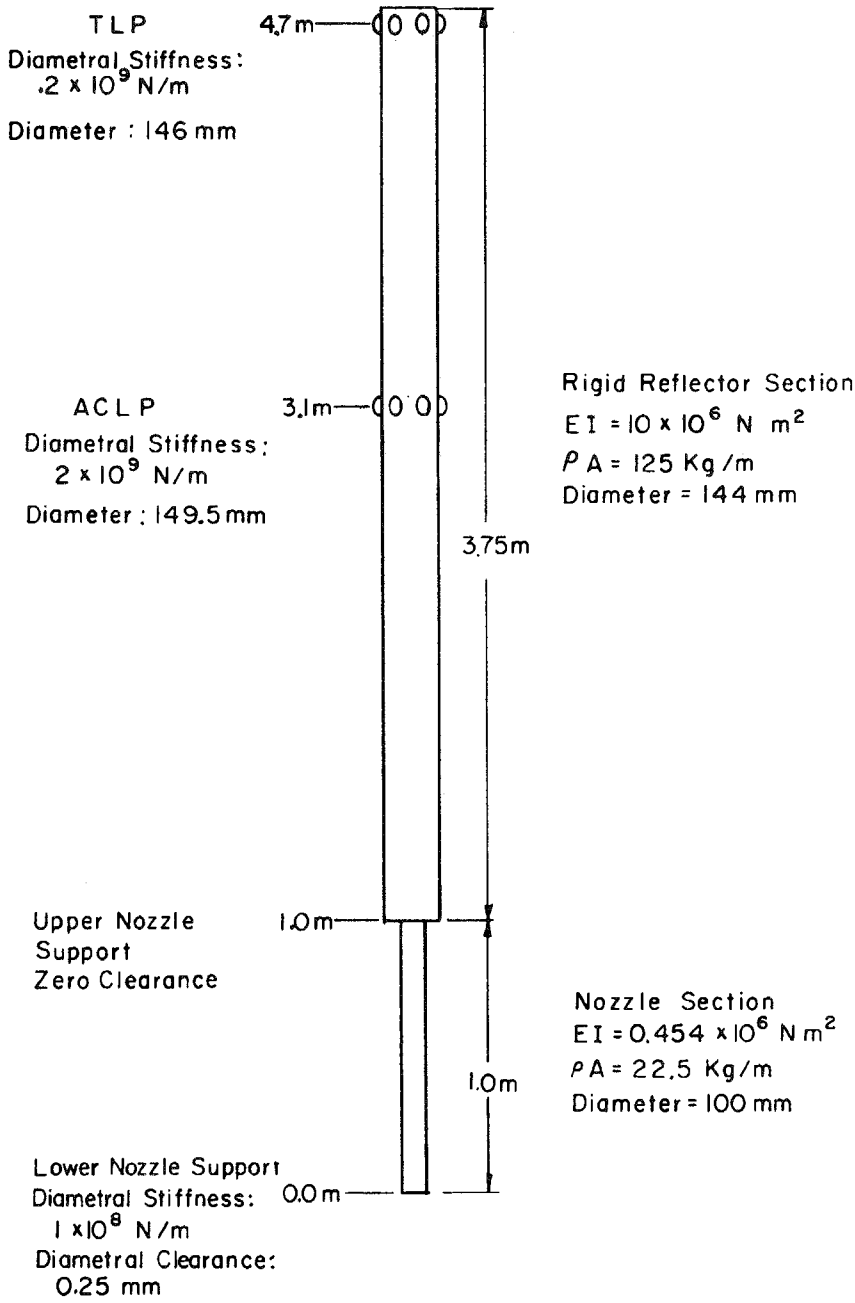

Fig. 3.2. Radial Reflection Assembly Description for Design D-2

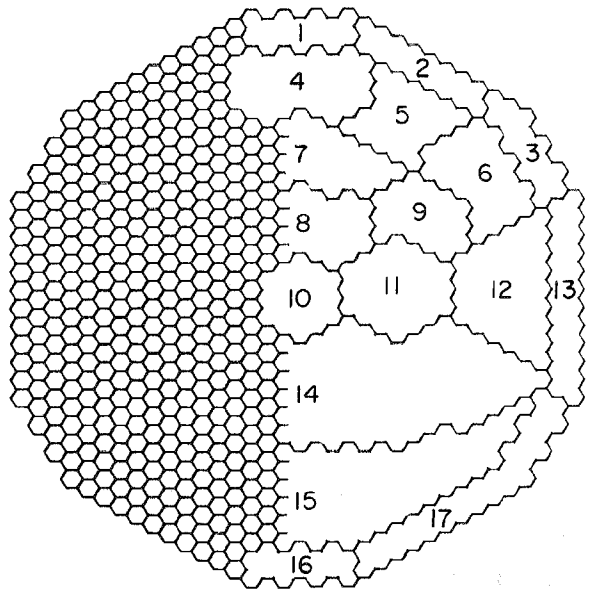

Fig. 3.3. Cluster Model for Use in the SCRAP Computer Code

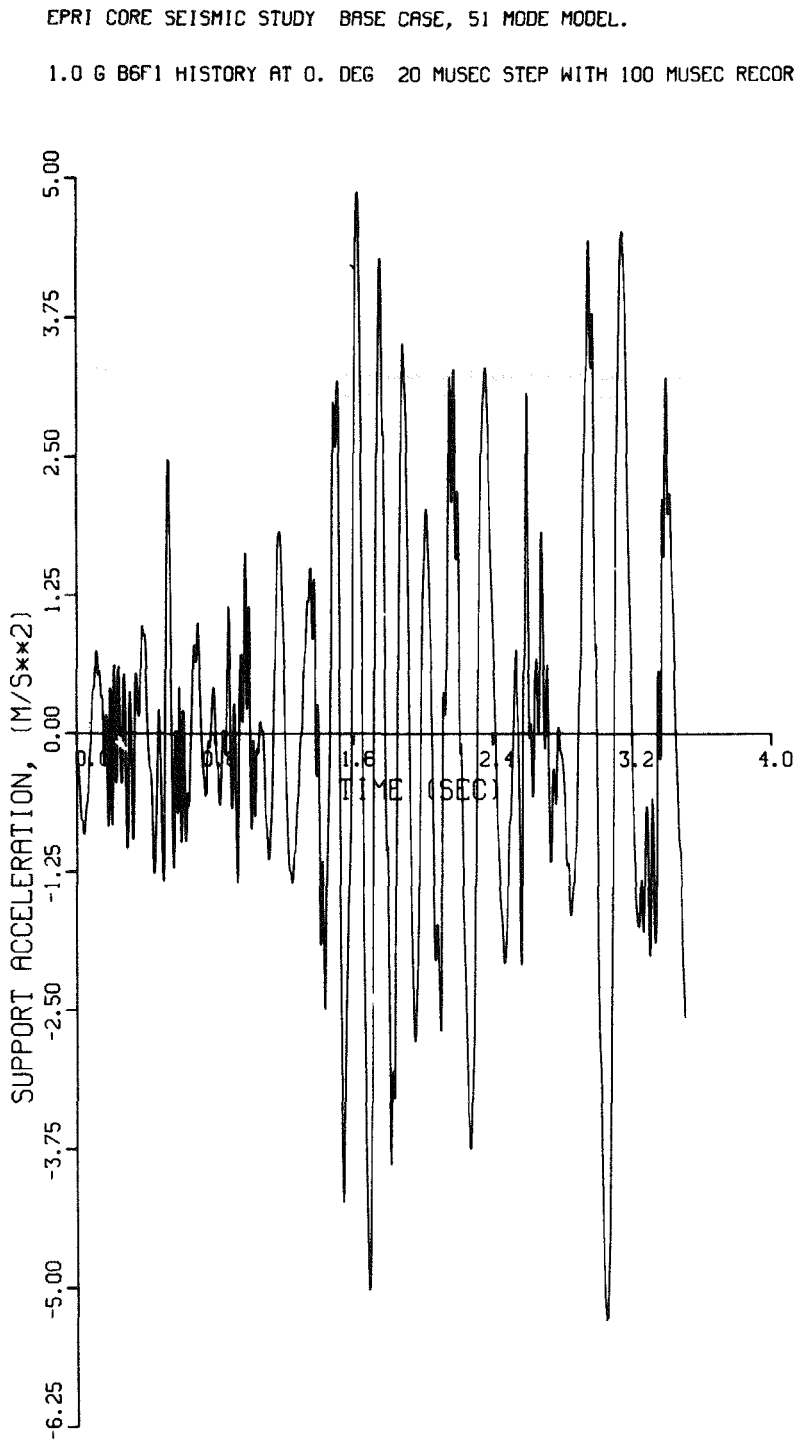

Fig. 3.4. Narrow Band, 6 Hz Center Frequency, Support Motion Time History

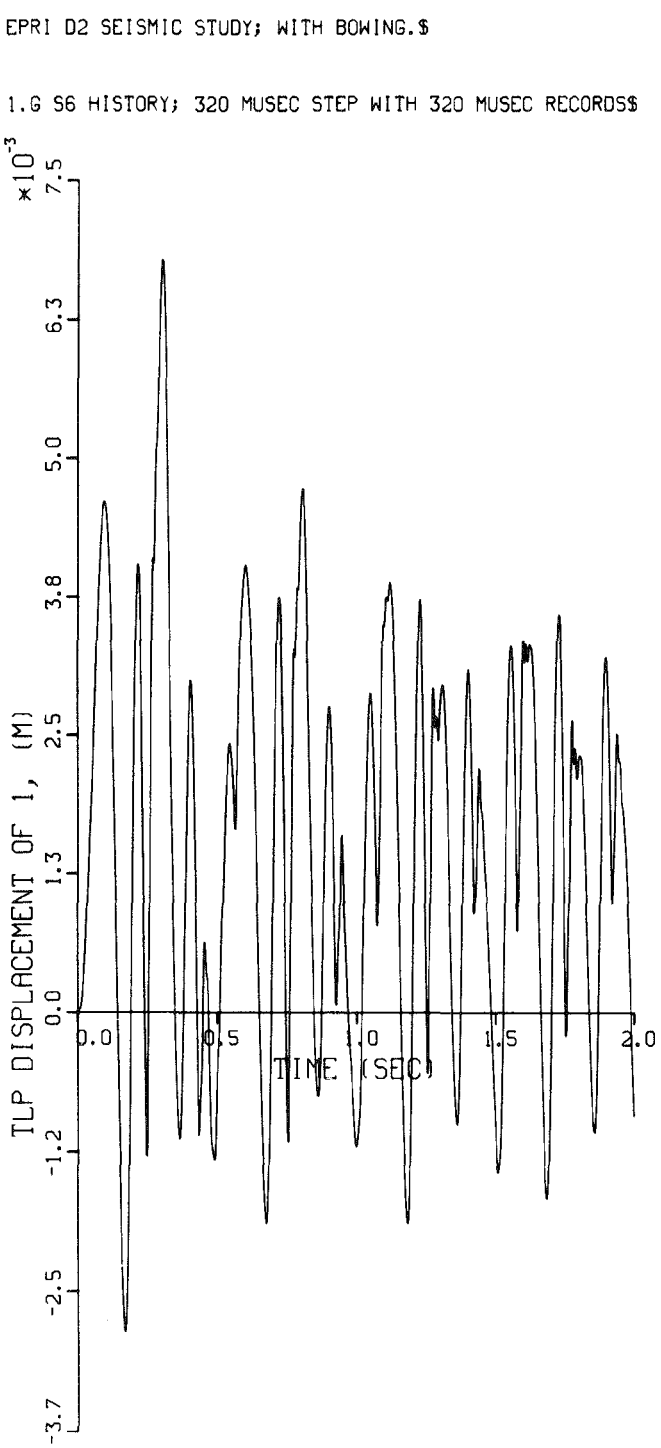

Fig. 3.5. Time History of TLP Displacement for Cluster #1

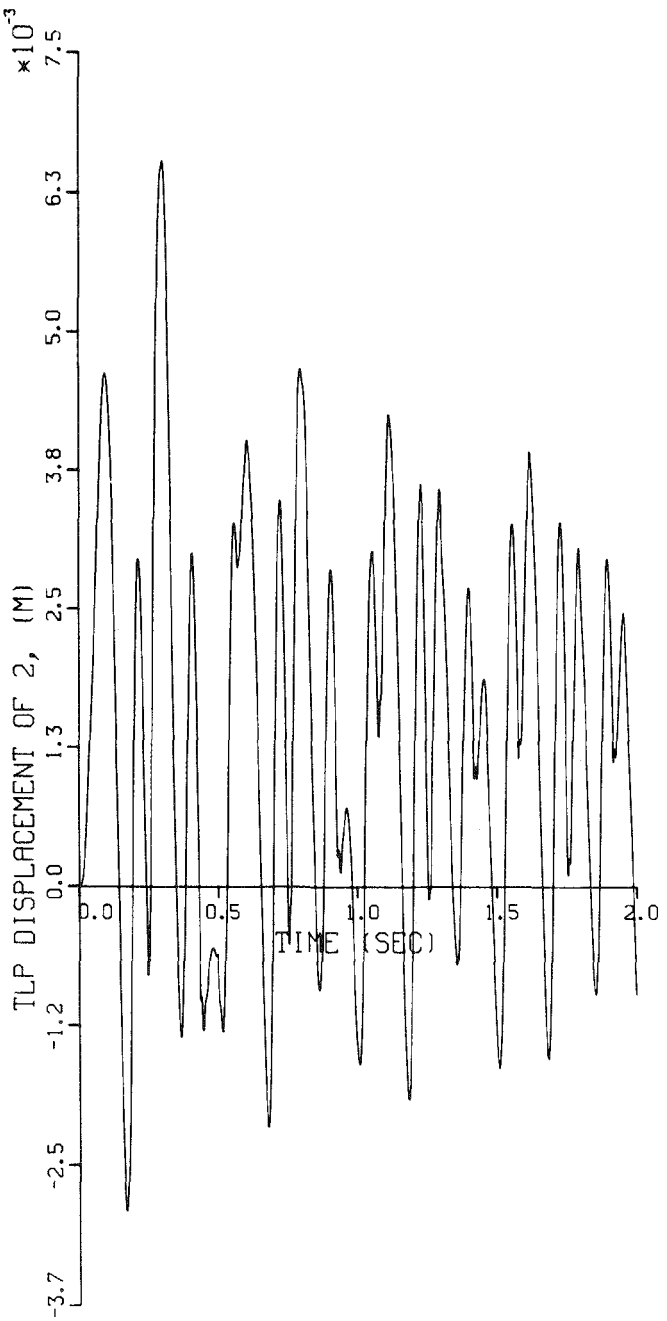

Fig. 3.6. Time History of TLP Displacement for Cluster #2

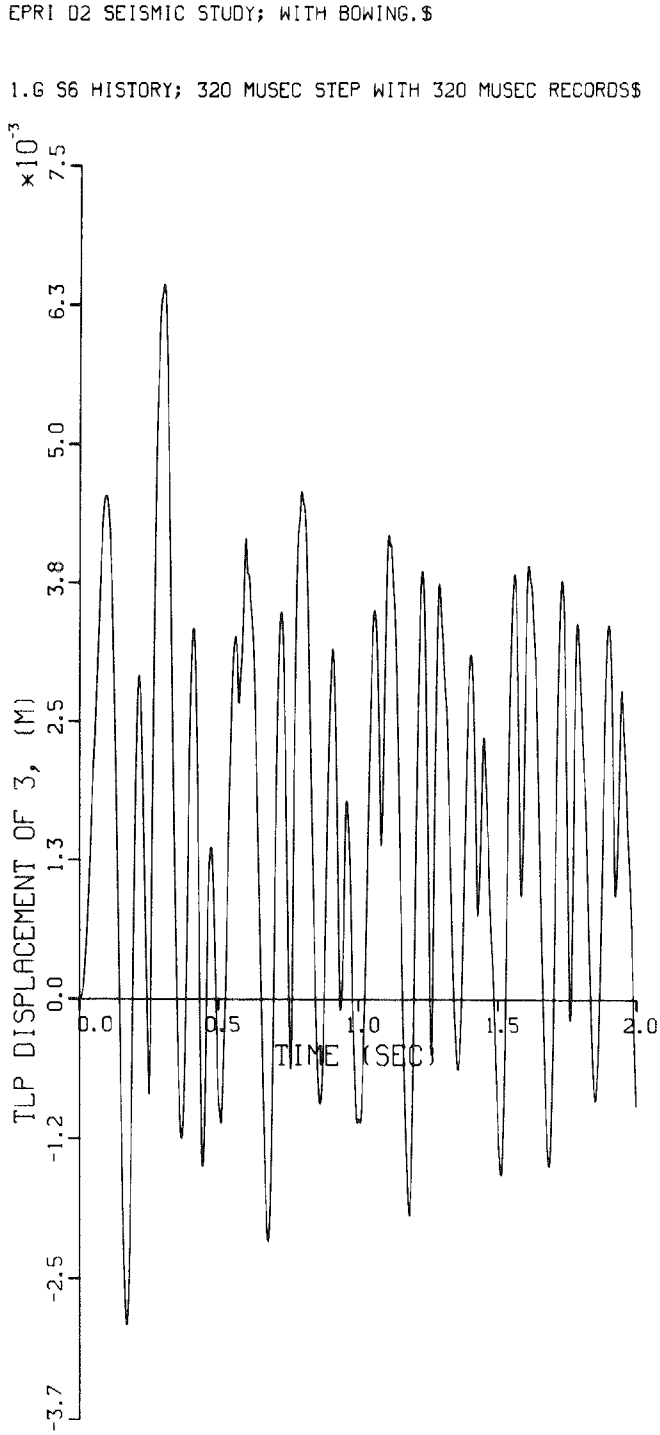

Fig. 3.7. Time History of TLP Displacement for Cluster #3

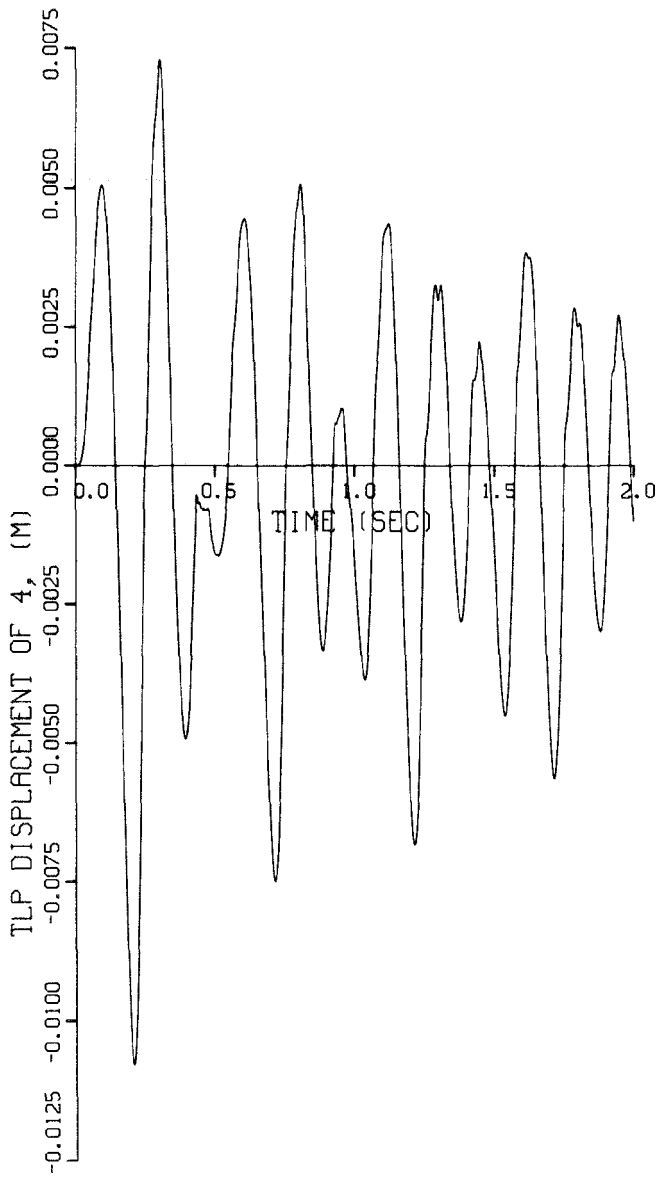

Fig. 3.8. Time History of TLP Displacement for Cluster #4

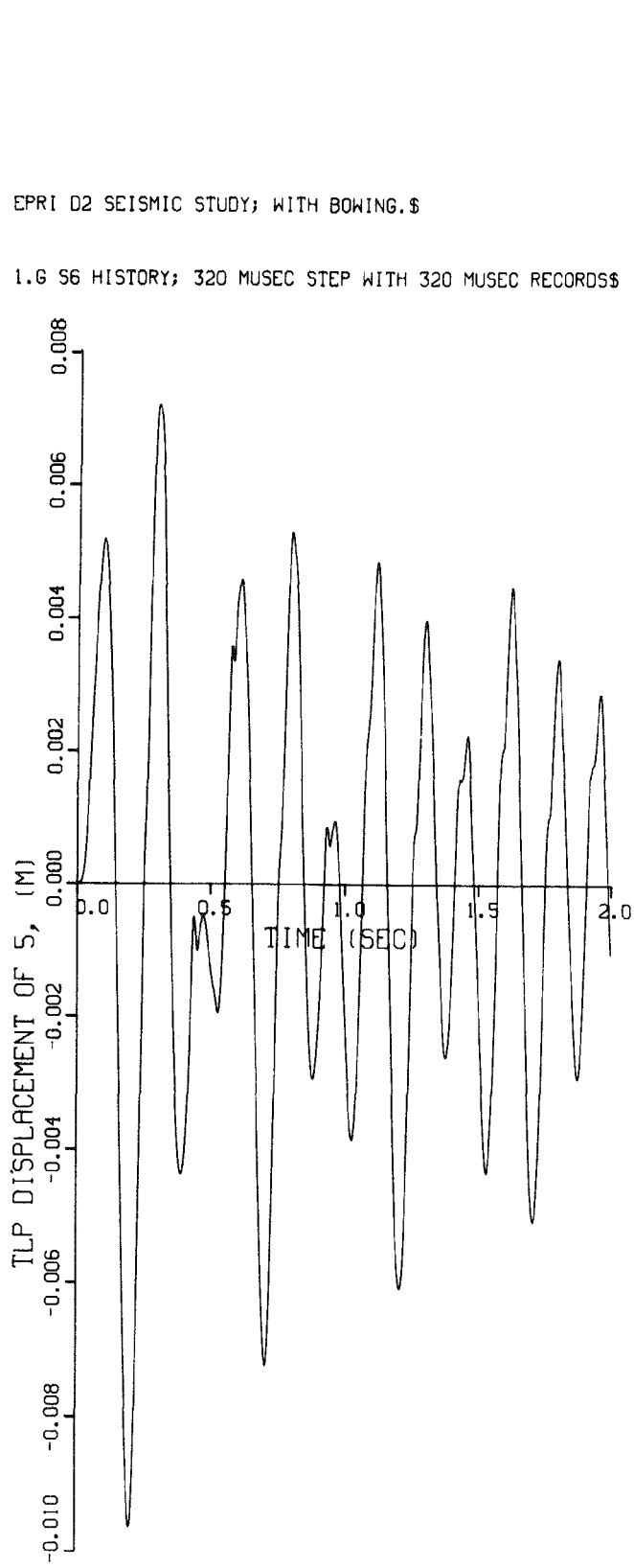

Fig. 3.9. Time History of TLP Displacement for Cluster #5

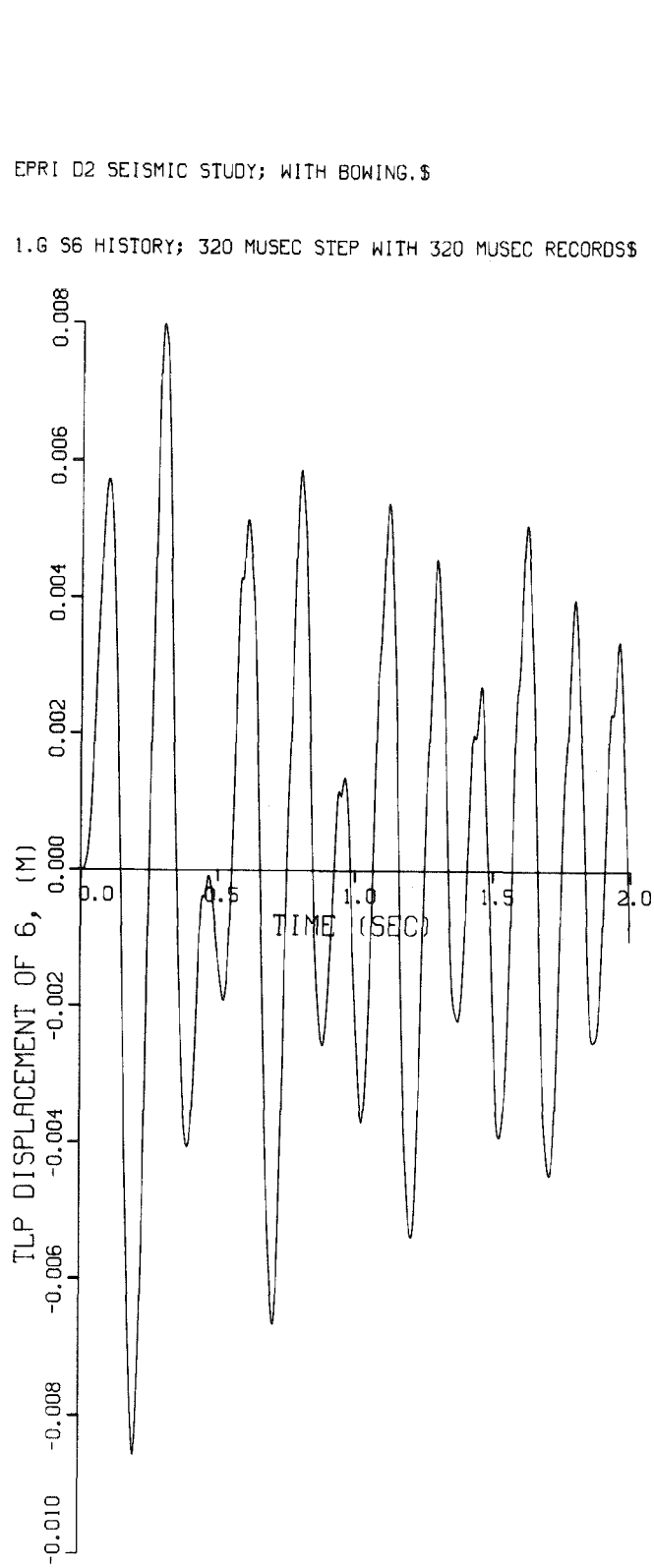

Fig. 3.10. Time History of TLP Displacement for Cluster #6

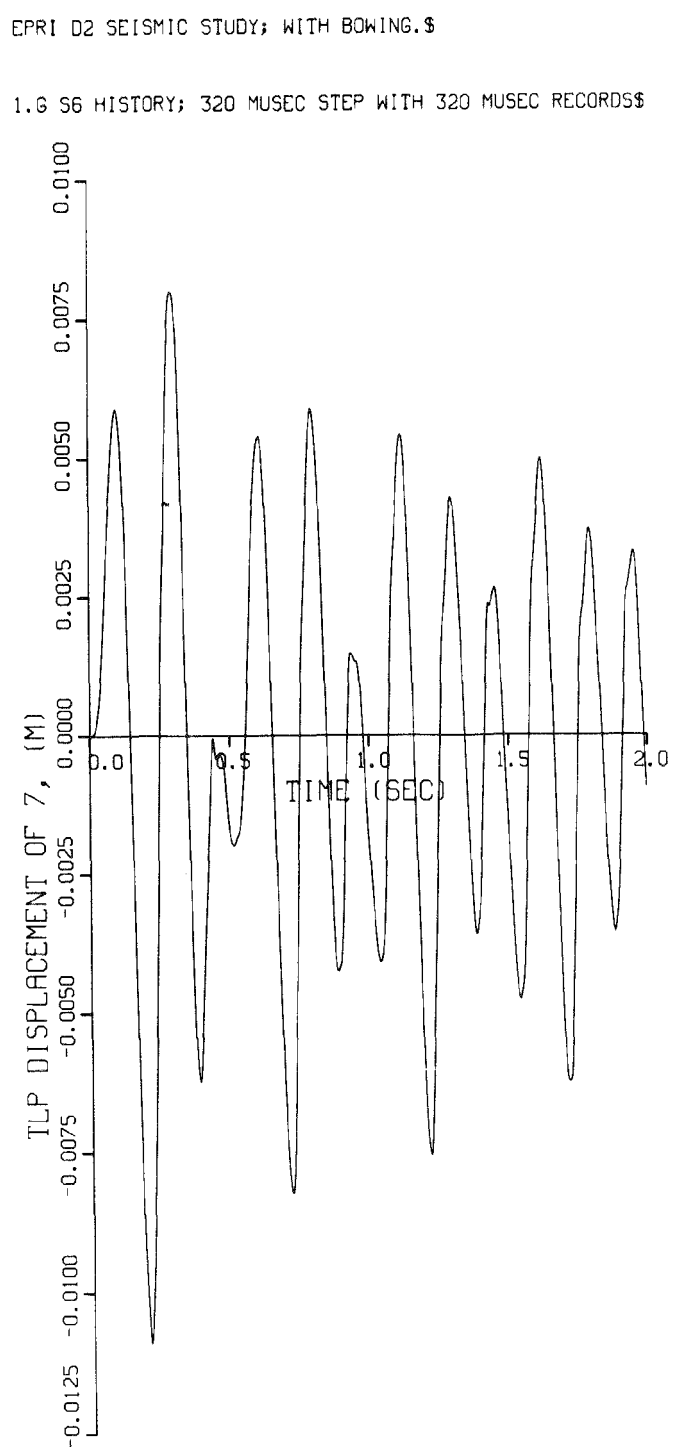

Fig. 3.11. Time History of TLP Displacement for Cluster #7

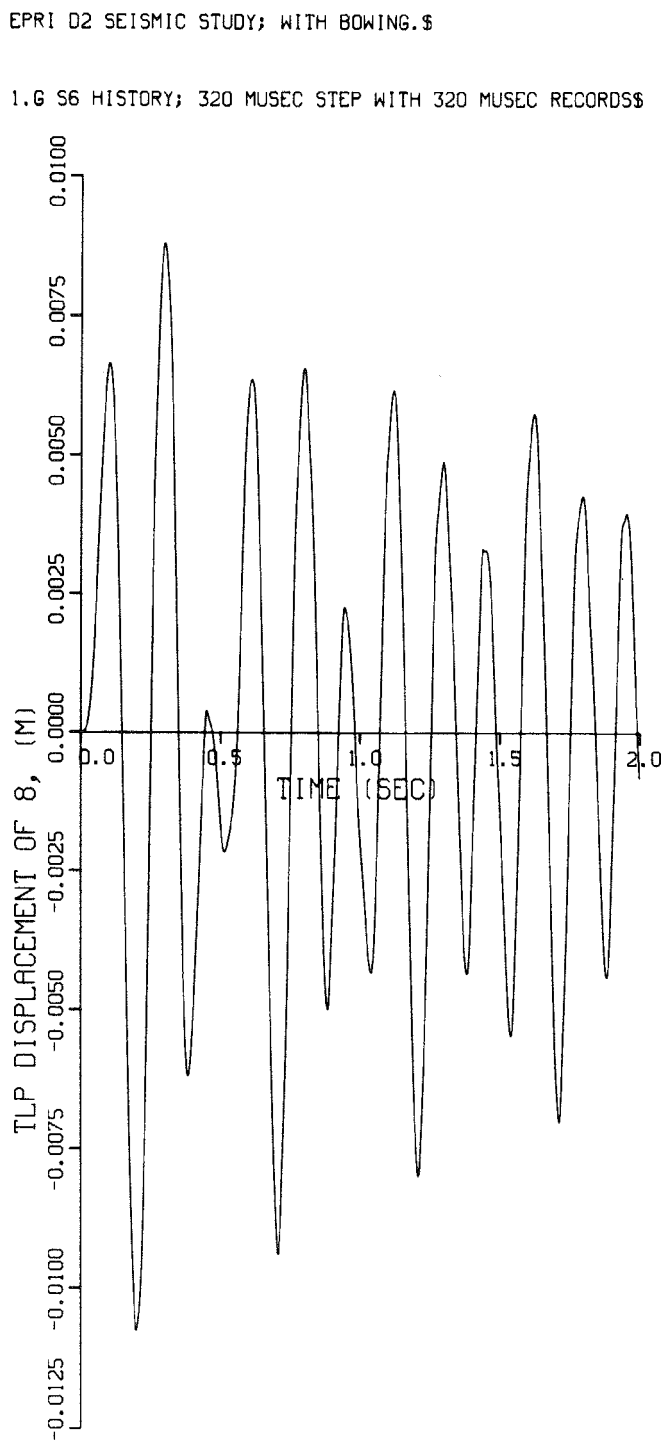

Fig. 3.12. Time History of TLP Displacement for Cluster #8

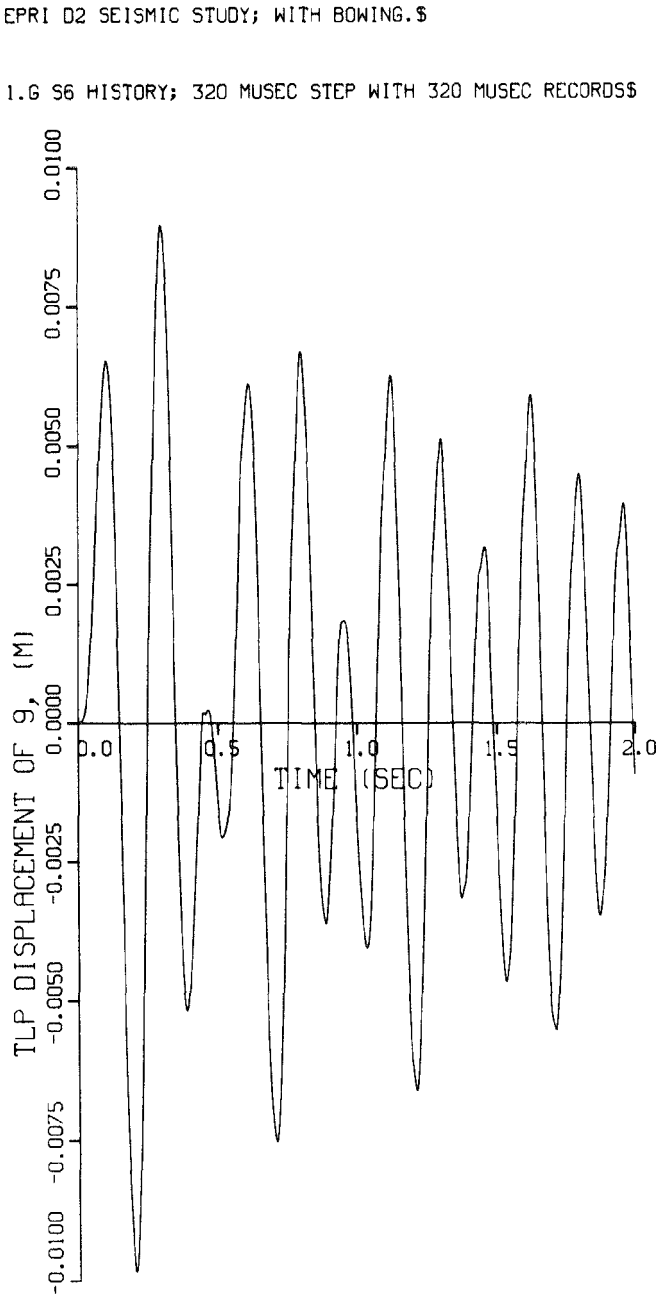

Fig. 3.13. Time History of TLP Displacement for Cluster #9

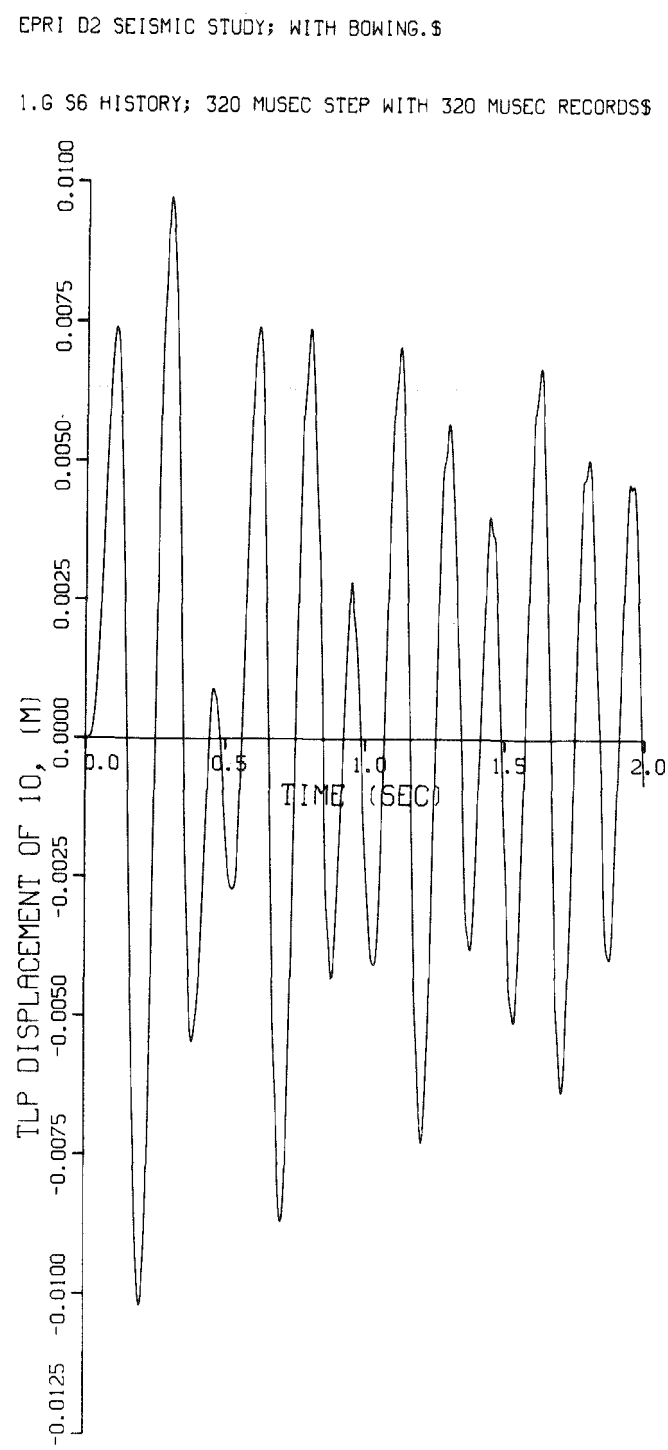

Fig. 3.14. Time History of TLP Displacement for Cluster #10

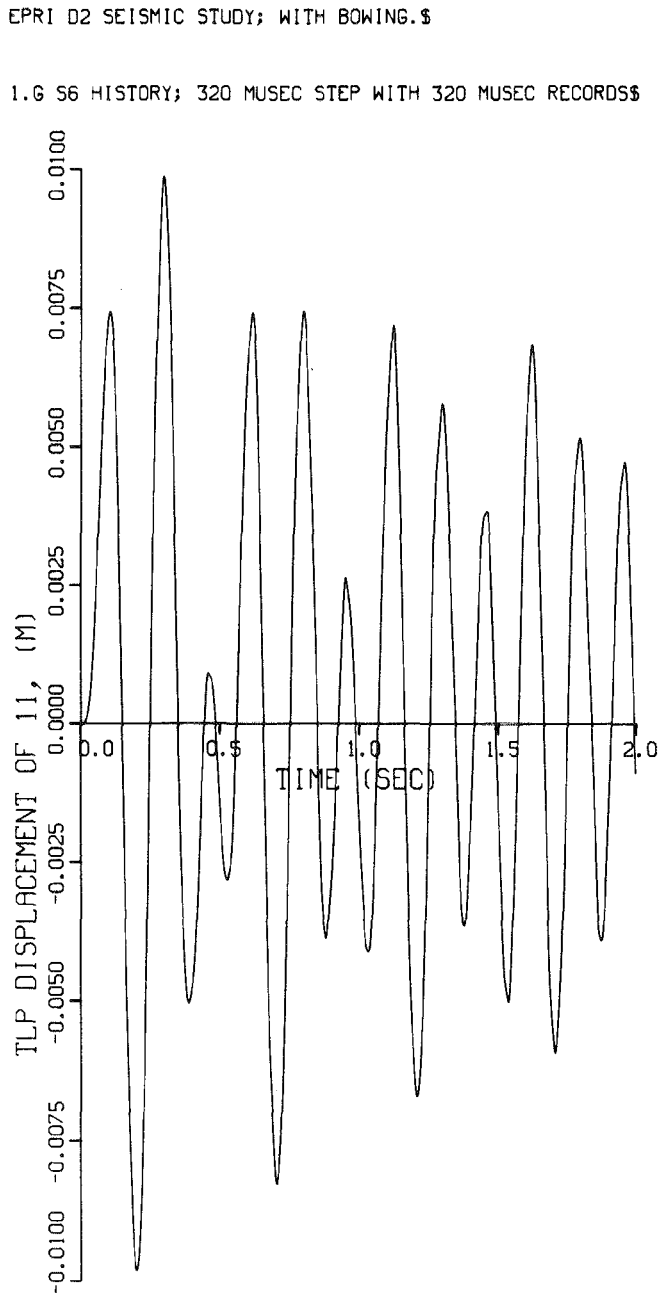

Fig. 3.15. Time History of TLP Displacement for Cluster #11

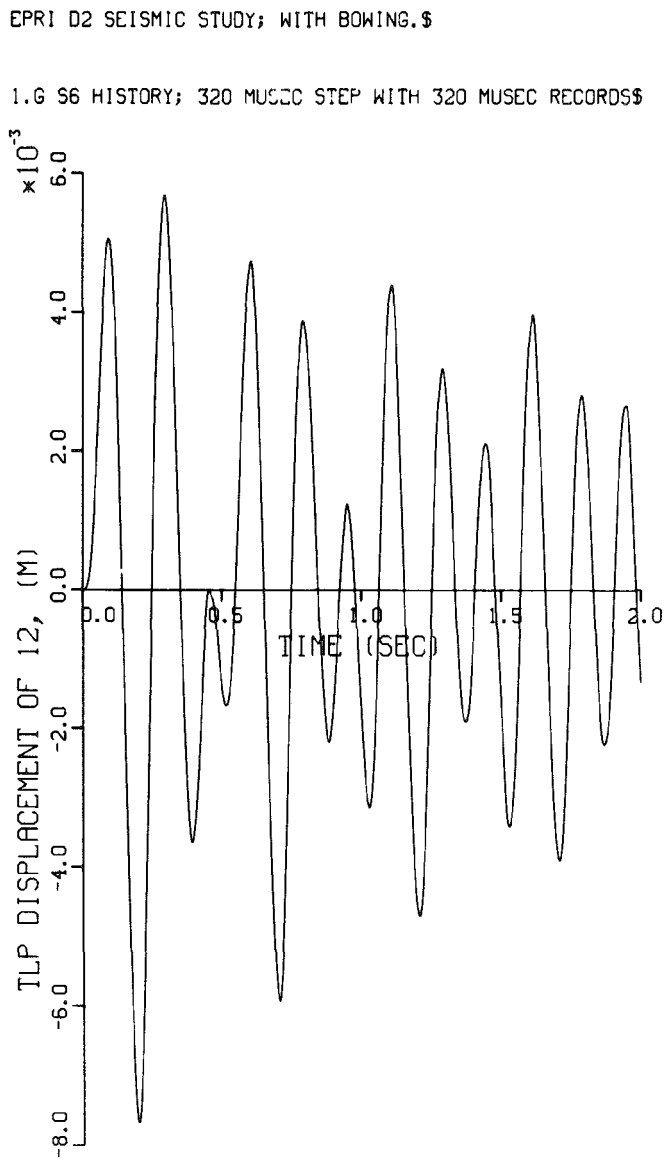

Fig. 3.16. Time History of TLP Displacement for Cluster #12

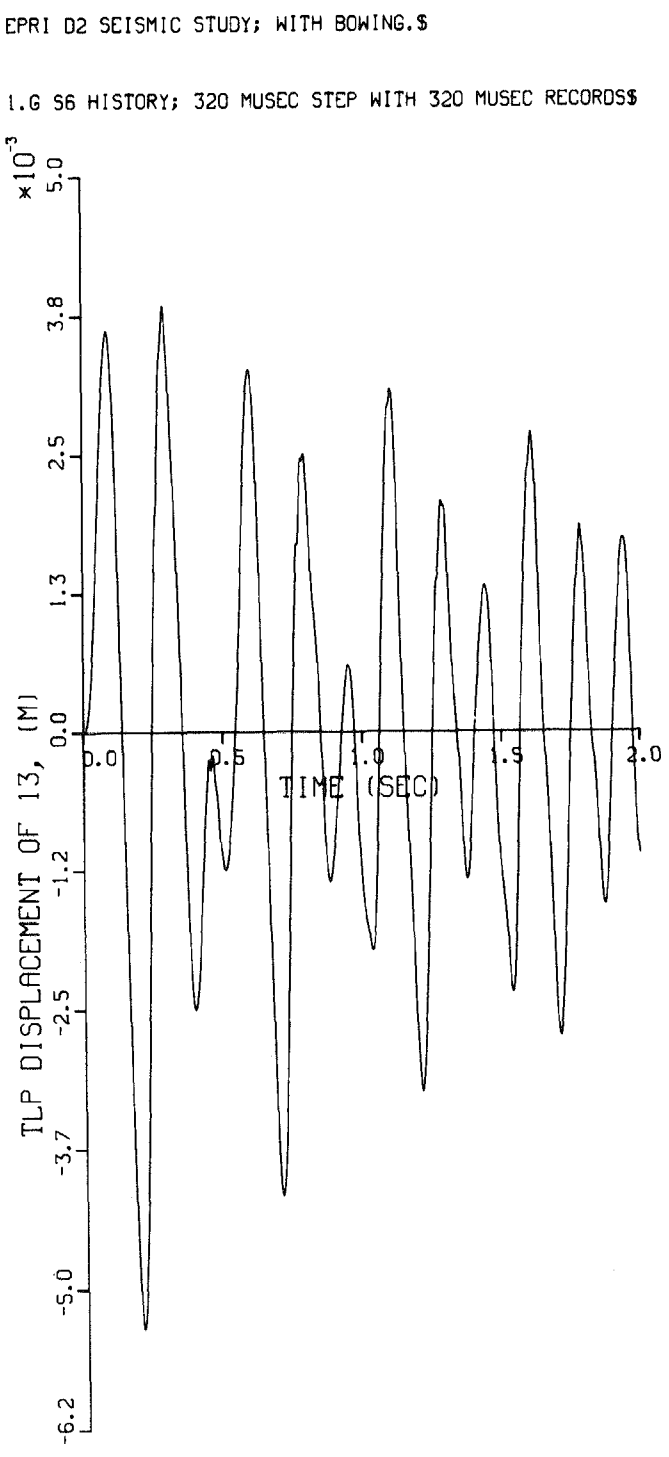

Fig. 3.17. Time History of TLP Displacement for Cluster #13

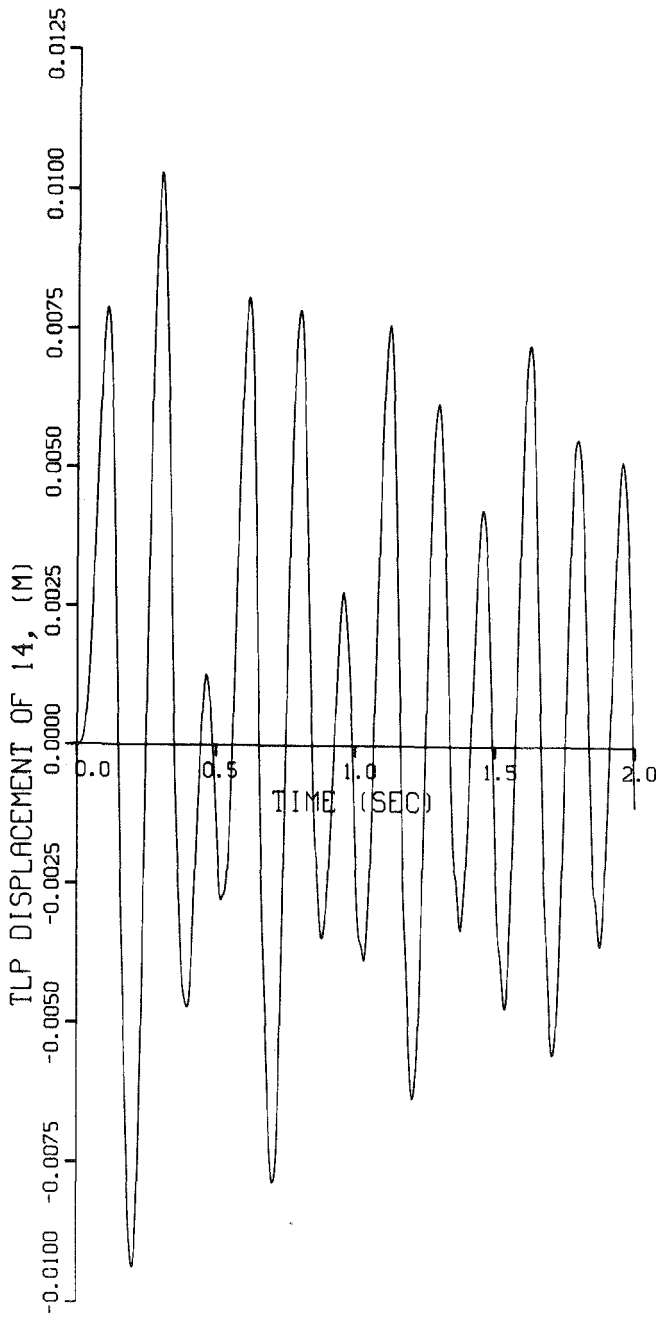

Fig. 3.18. Time History of TLP Displacement for Cluster #14

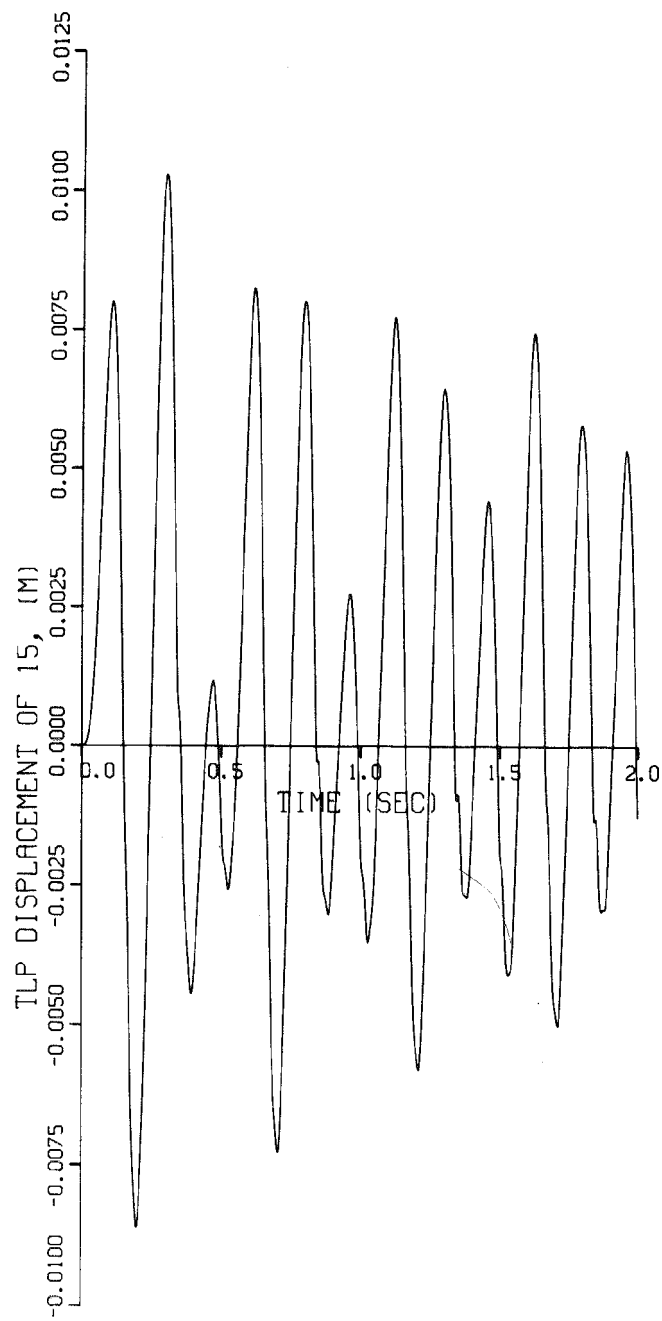

Fig. 3.19. Time History of TLP Displacement for Cluster #15

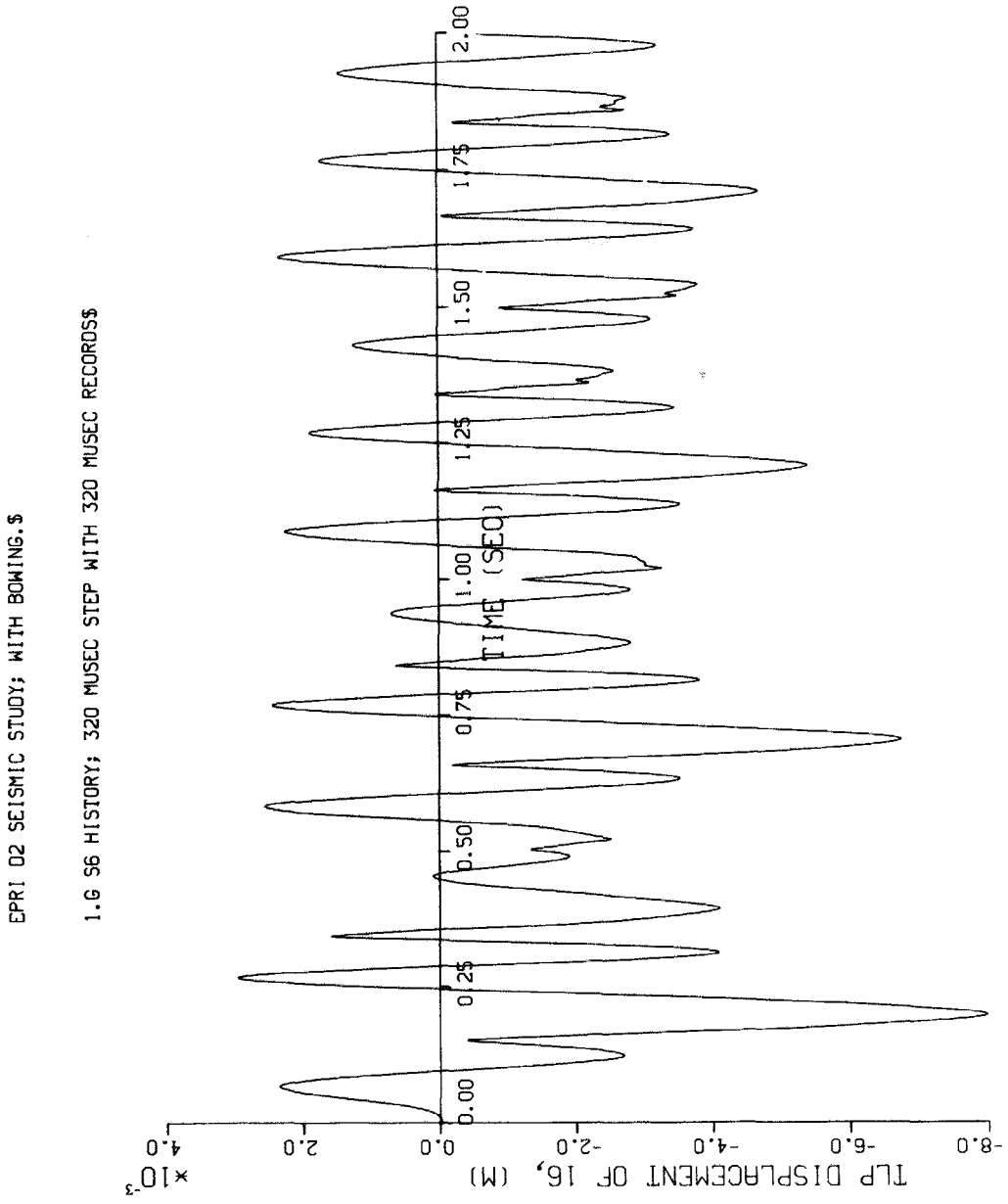

Fig. 3.20. Time History of TLP Displacement for Cluster #16

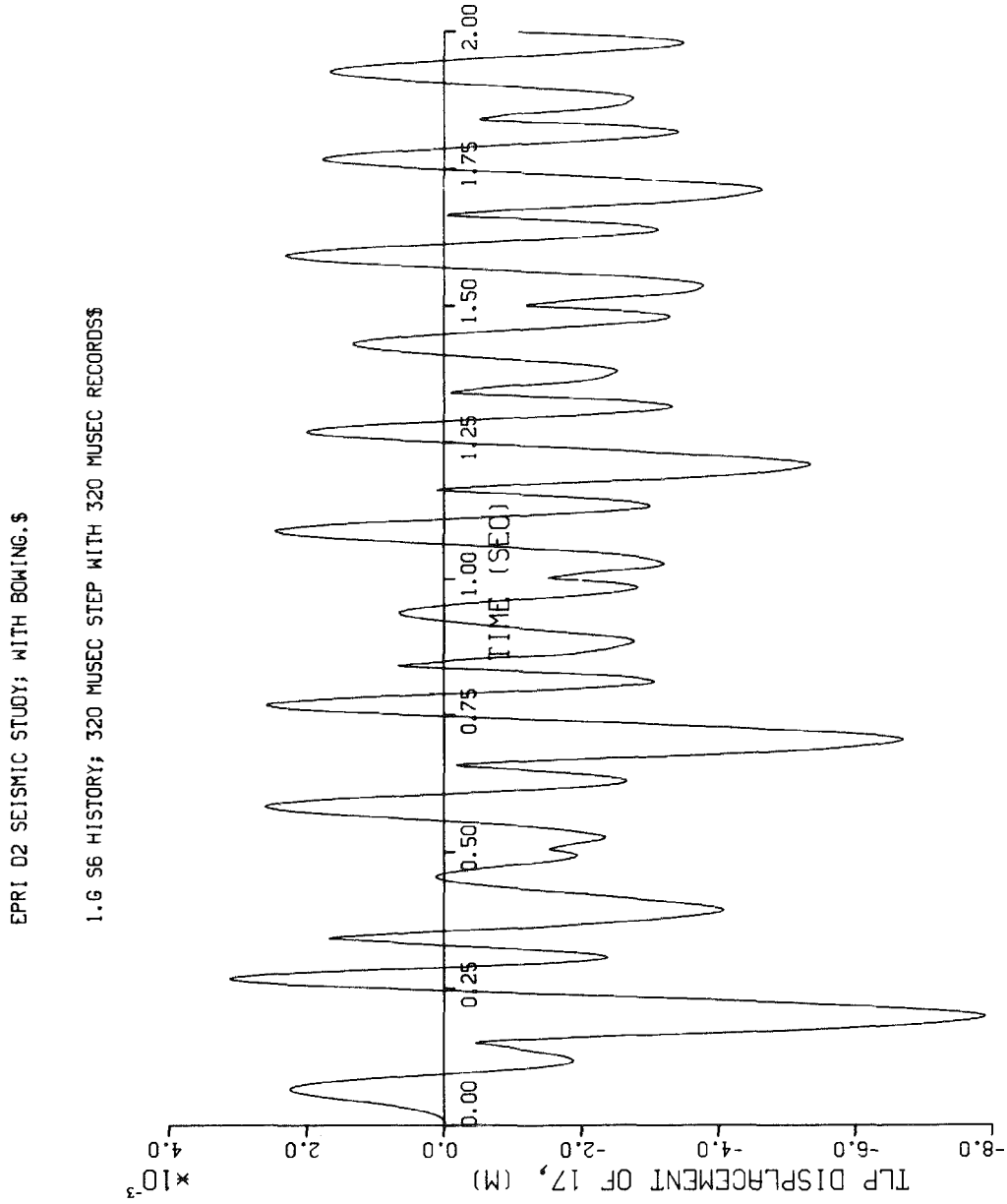

Fig. 3.21. Time History of TLP Displacement for Cluster #17

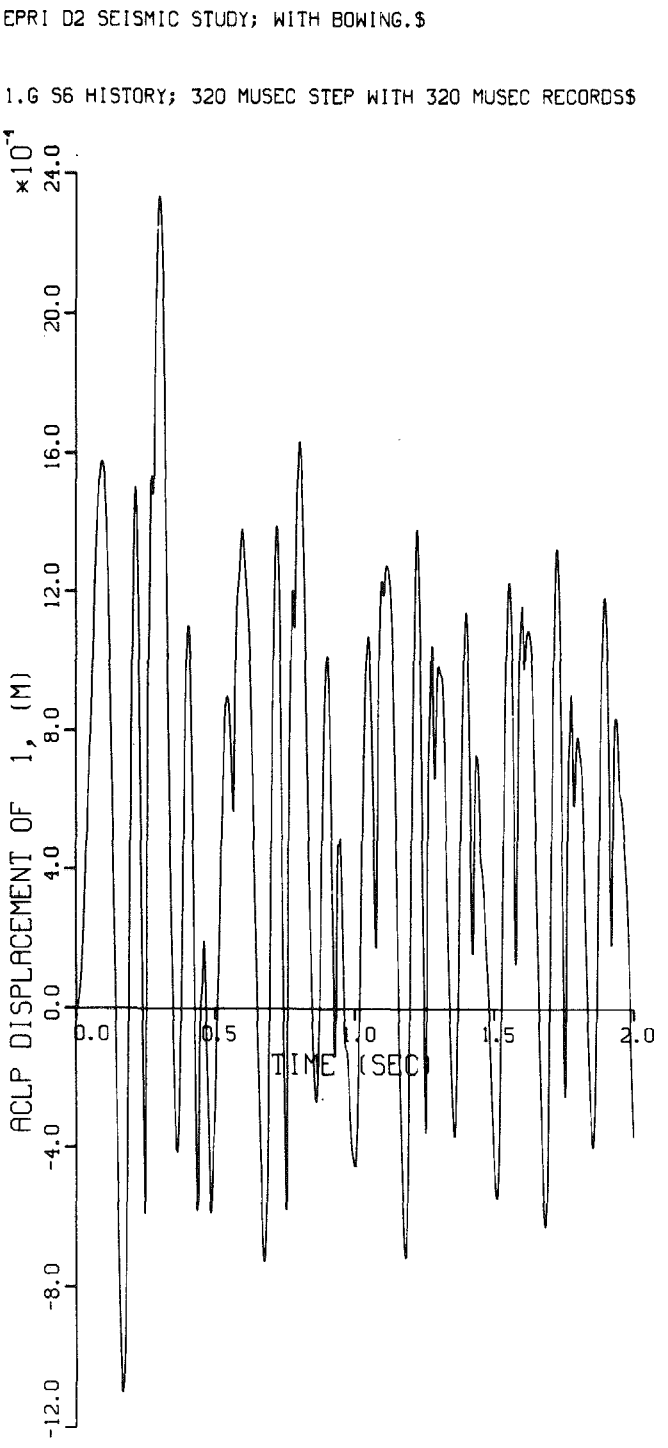

Fig. 3.22. Time History of ACLP Displacement for Cluster #1

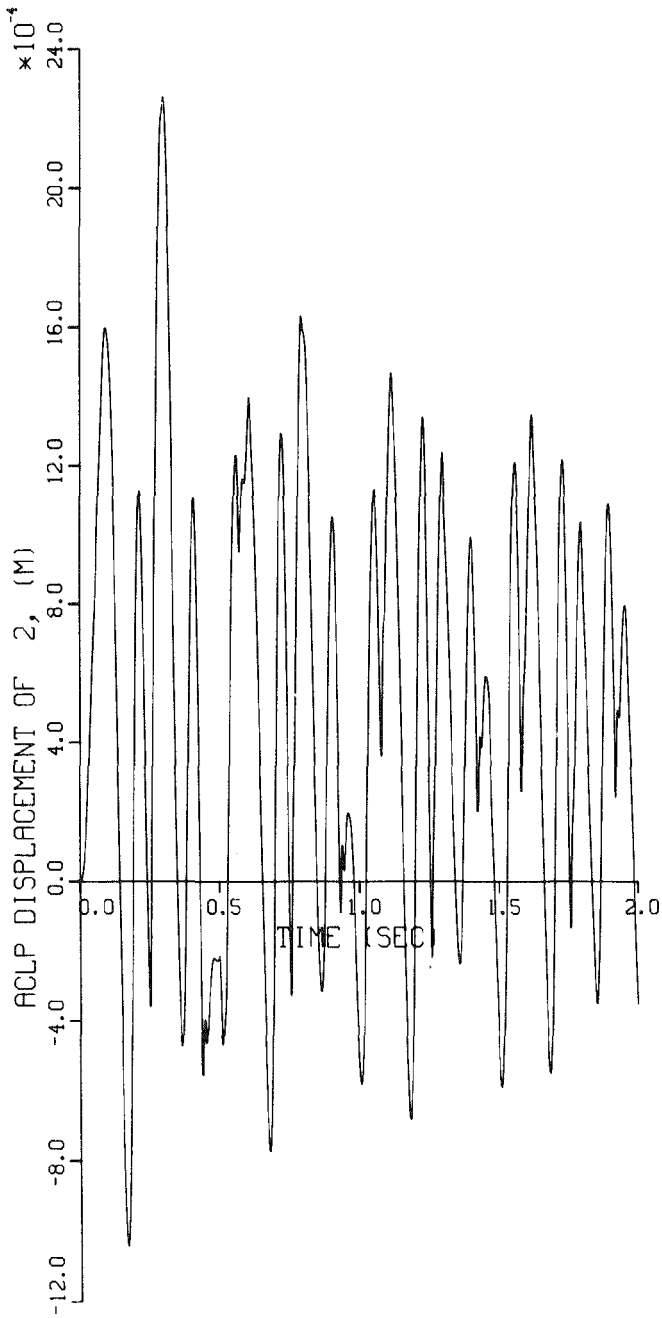

Fig. 3.23. Time History of ACLP Displacement for Cluster #2

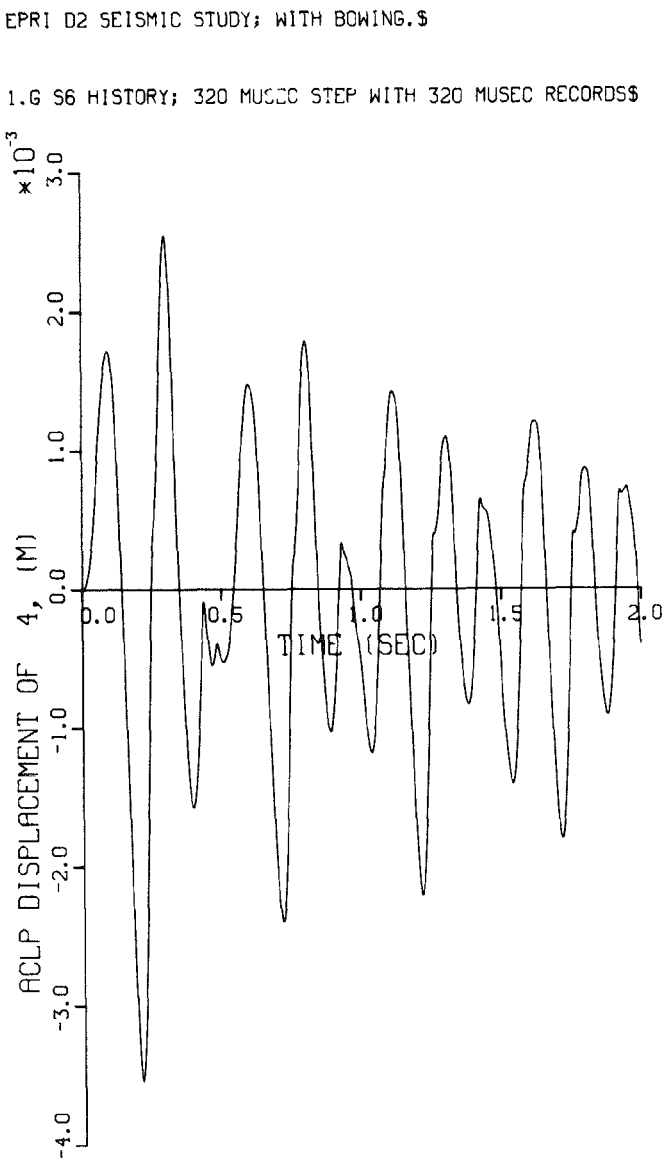

Fig. 3.24. Time History of ACLP Displacement for Cluster #4

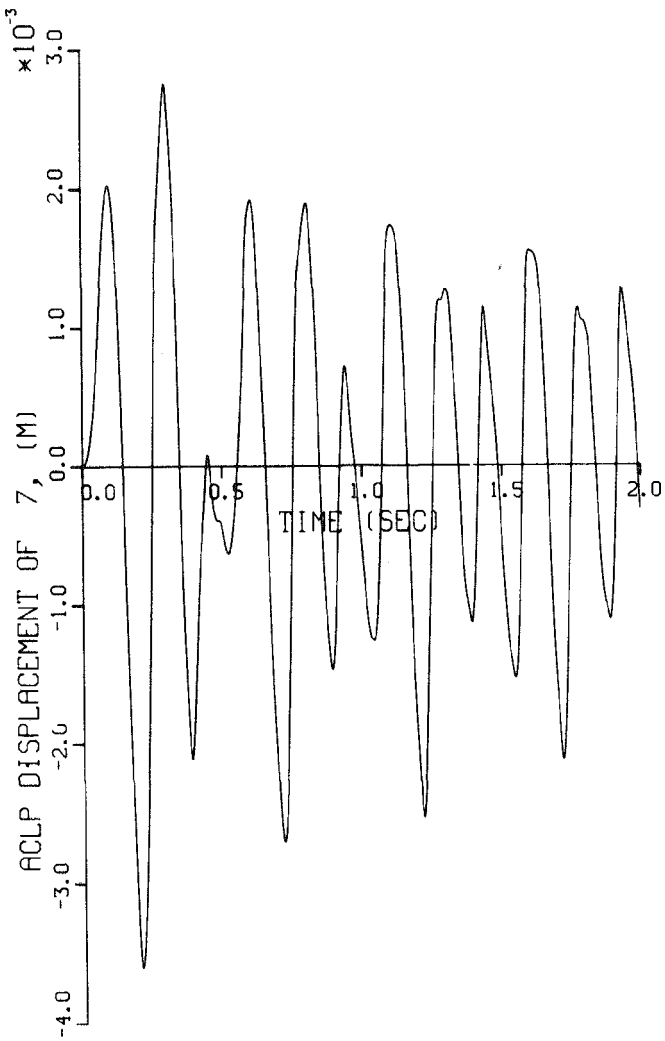

Fig. 3.25. Time History of ACLP Displacement for Cluster #7

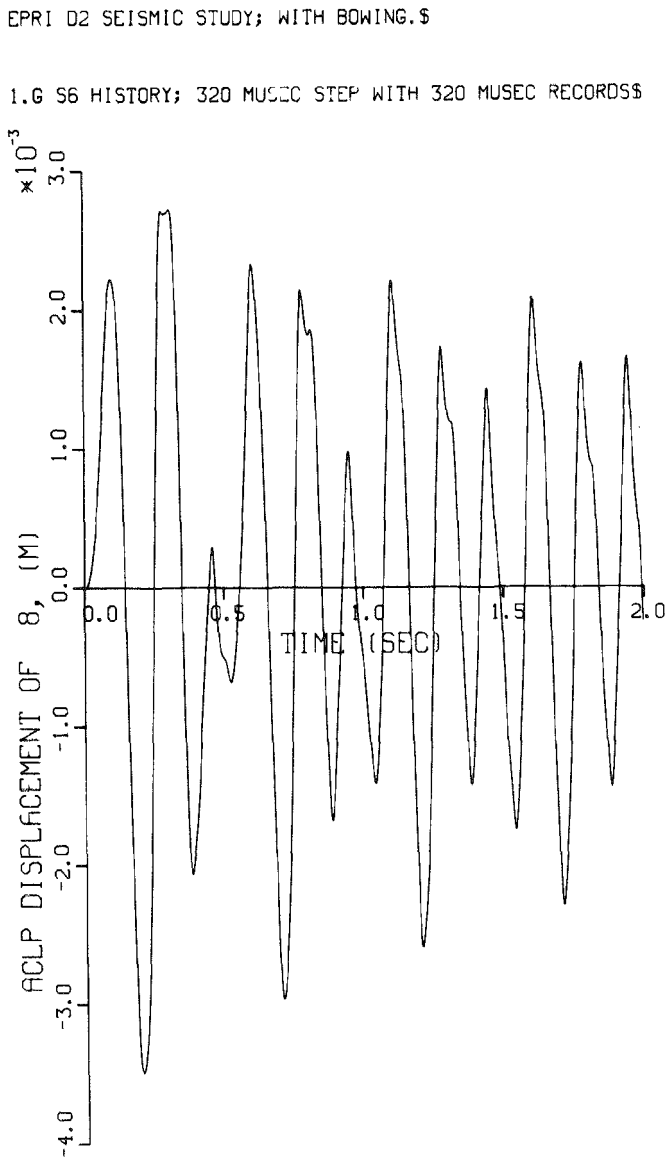

Fig. 3.26. Time History of ACLP Displacement for Cluster #8

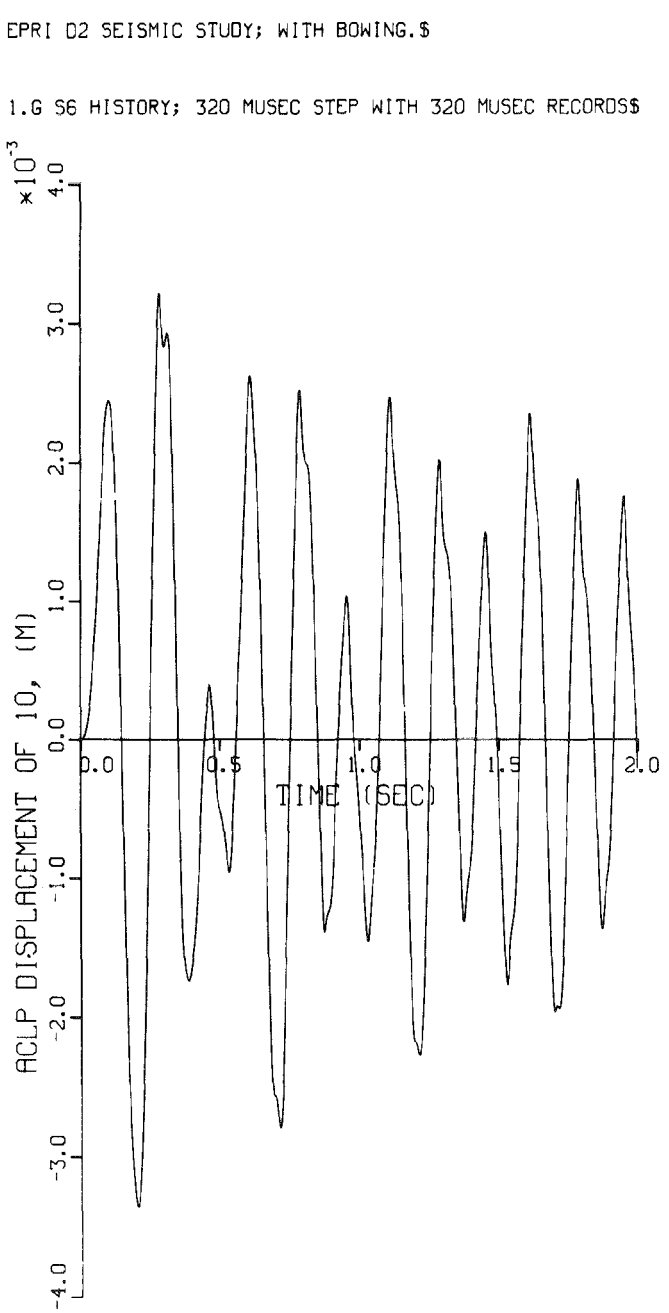

Fig. 3.27. Time History of ACLP Displacement for Cluster #10

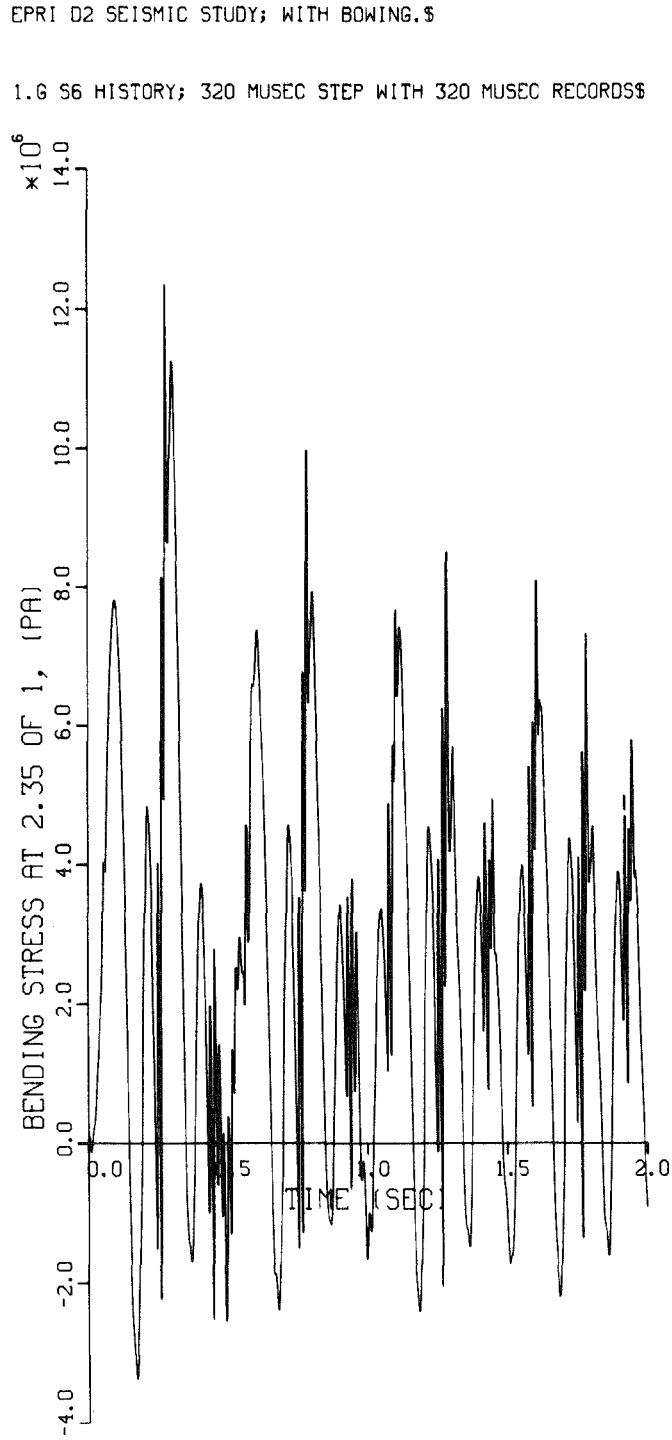

Fig. 3.28. Time History of the Bending Stresses at Mid-core for Cluster #1

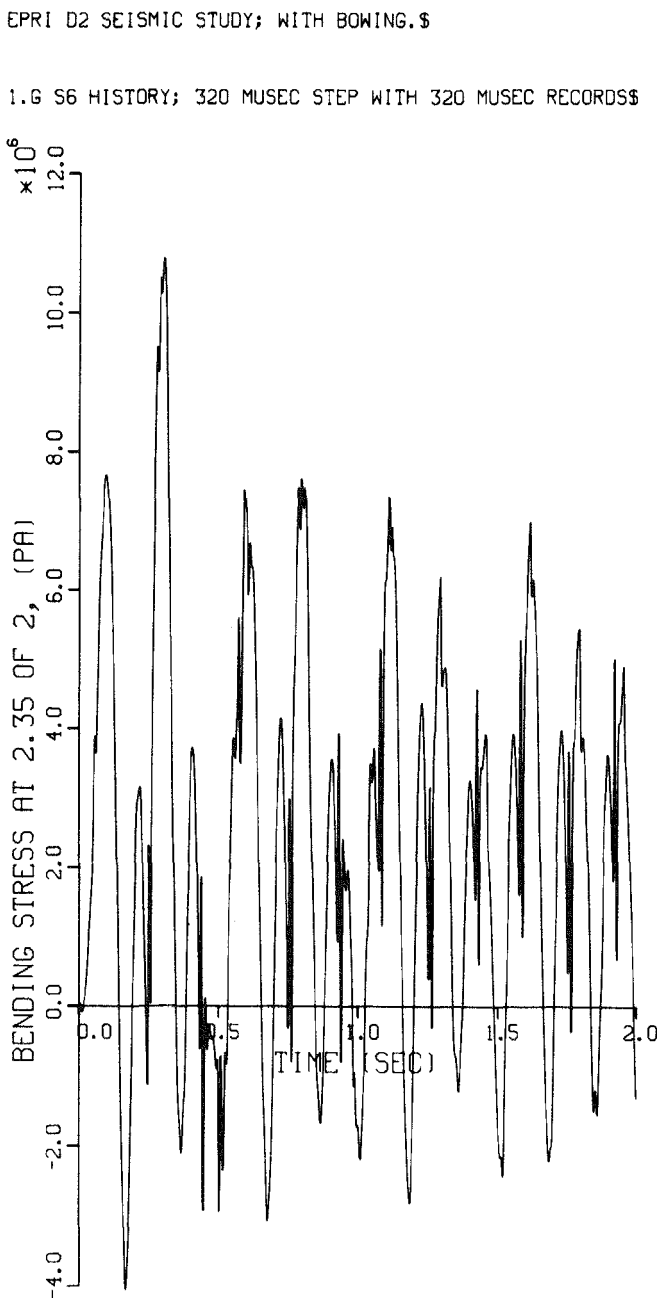

Fig. 3.29. Time History of the Bending Stresses at Mid-core for Cluster #2

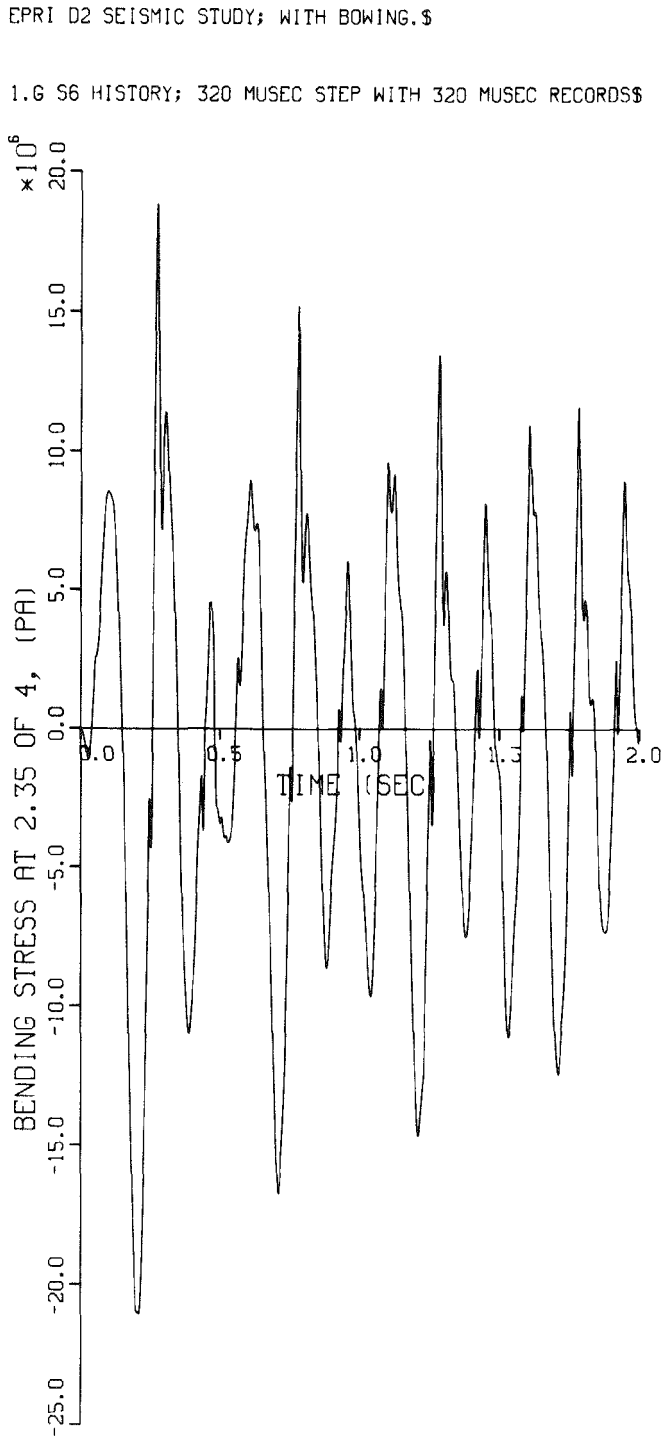

Fig. 3.30. Time History of the Bending Stresses at Mid-core for Cluster #4

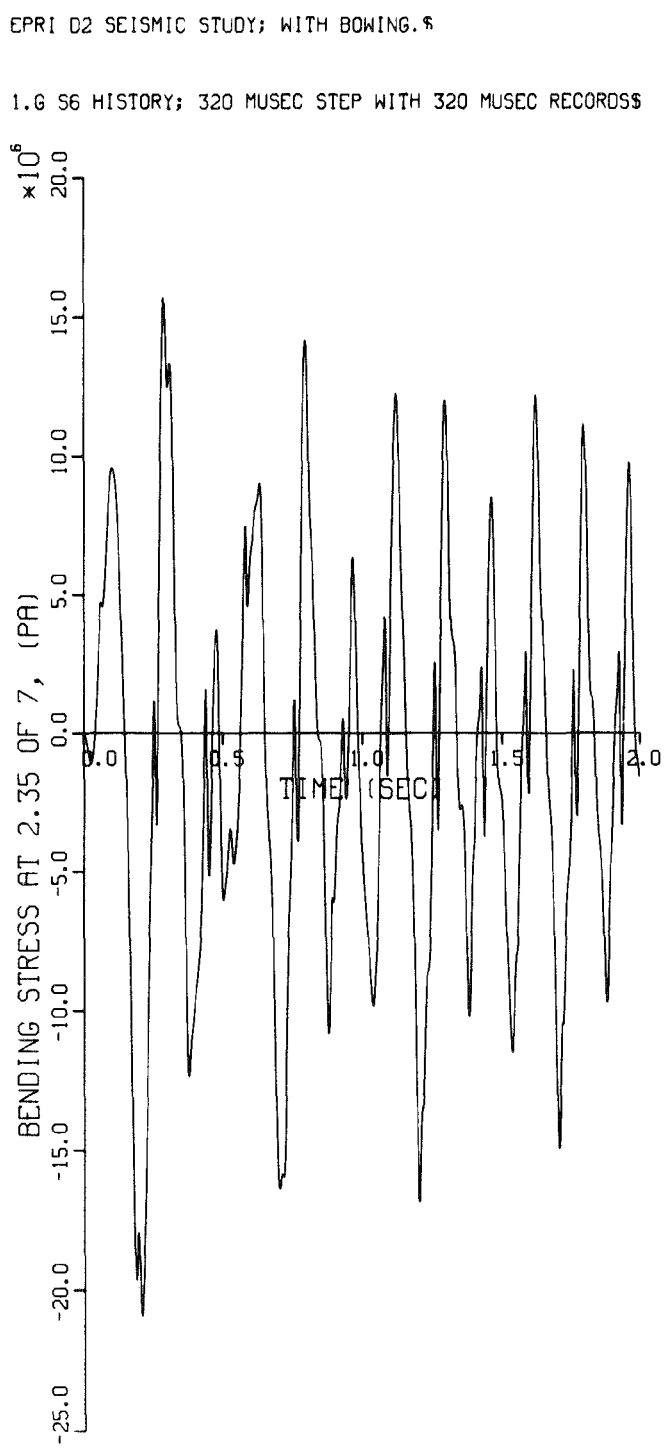

Fig. 3.31. Time History of the Bending Stresses at Mid-core for Cluster #7

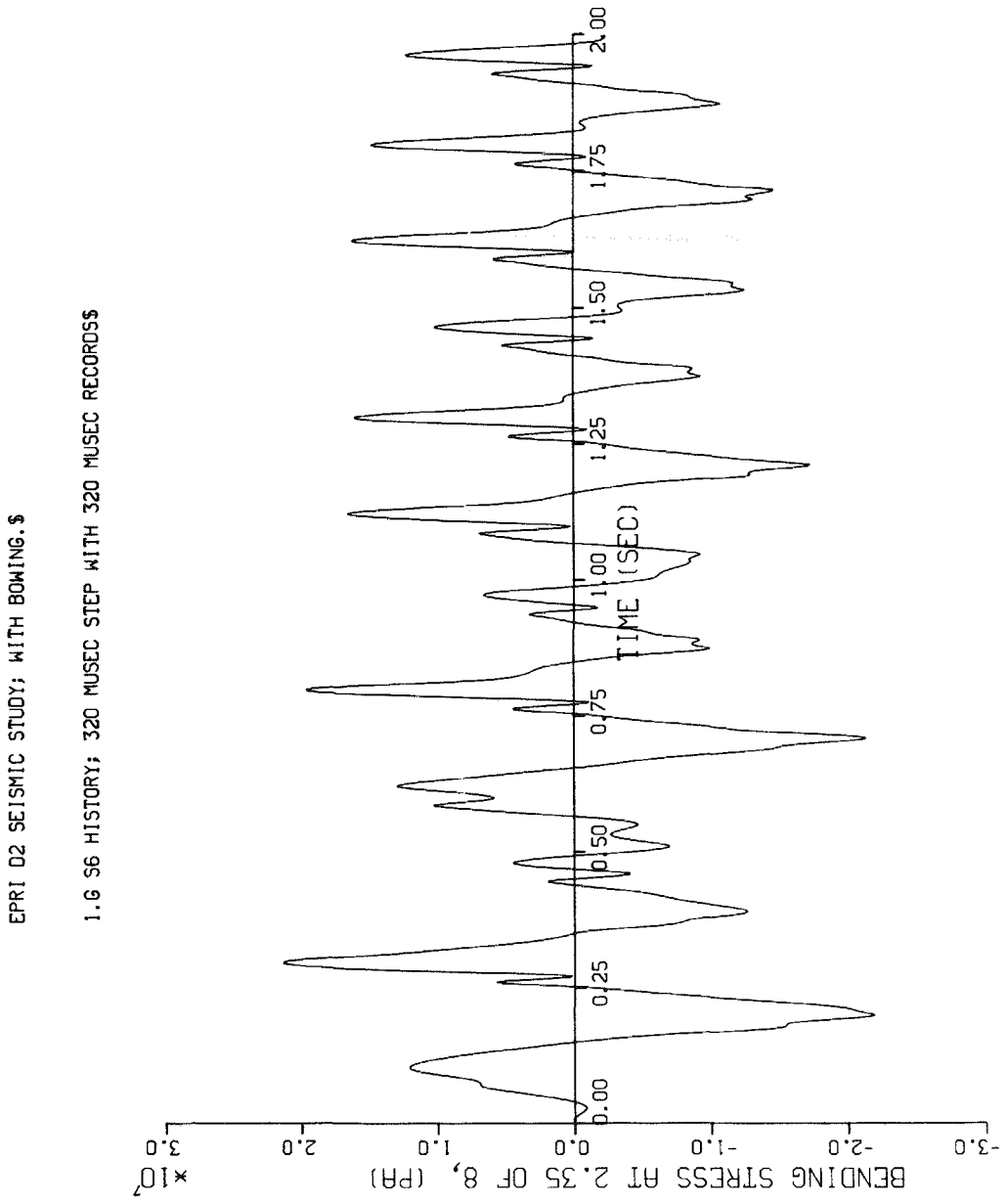

Fig. 3.32. Time History of the Bending Stresses at Mid-core for Cluster #8

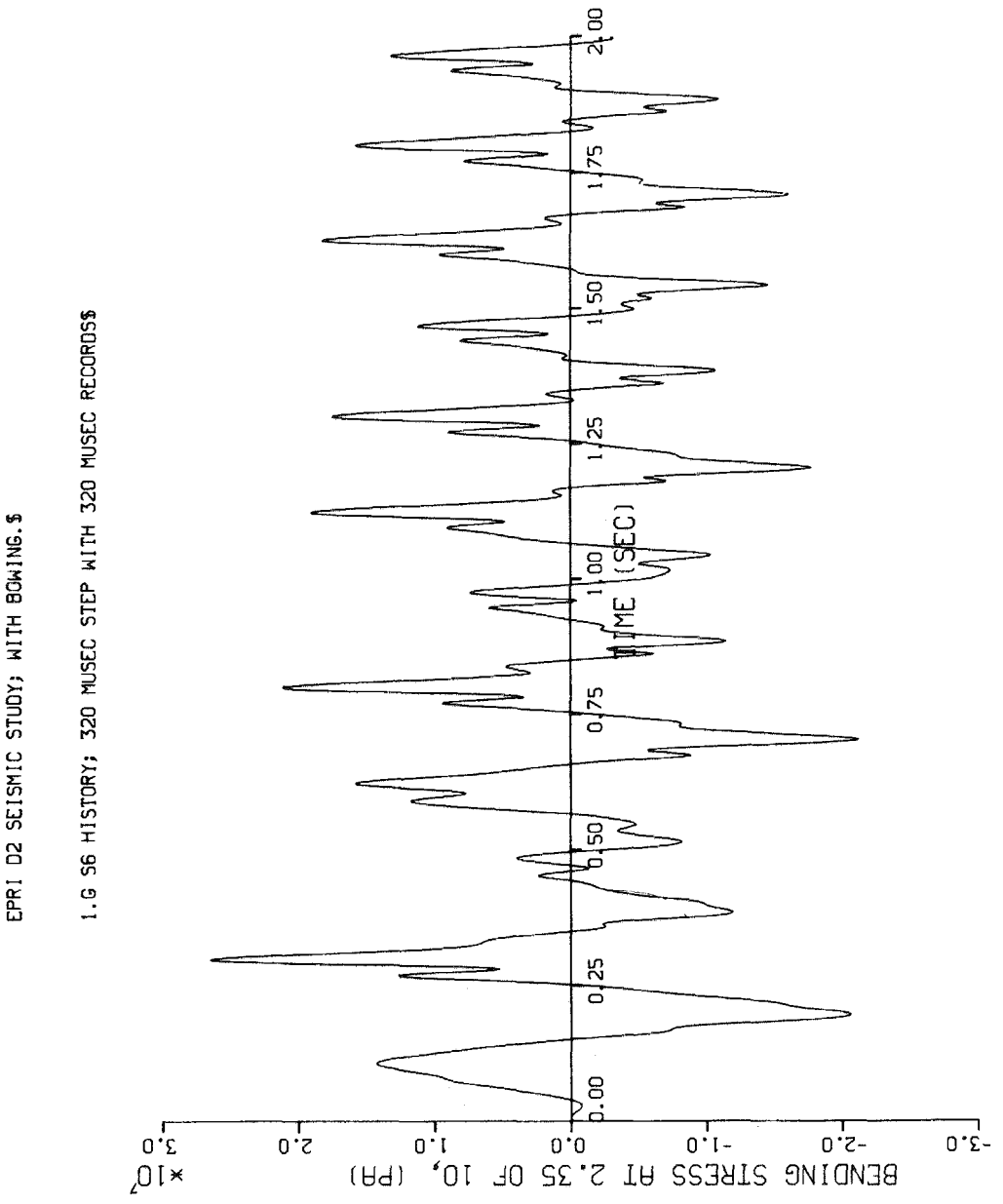

Fig. 3.33. Time History of the Bending Stresses at Mid-core for Cluster #10

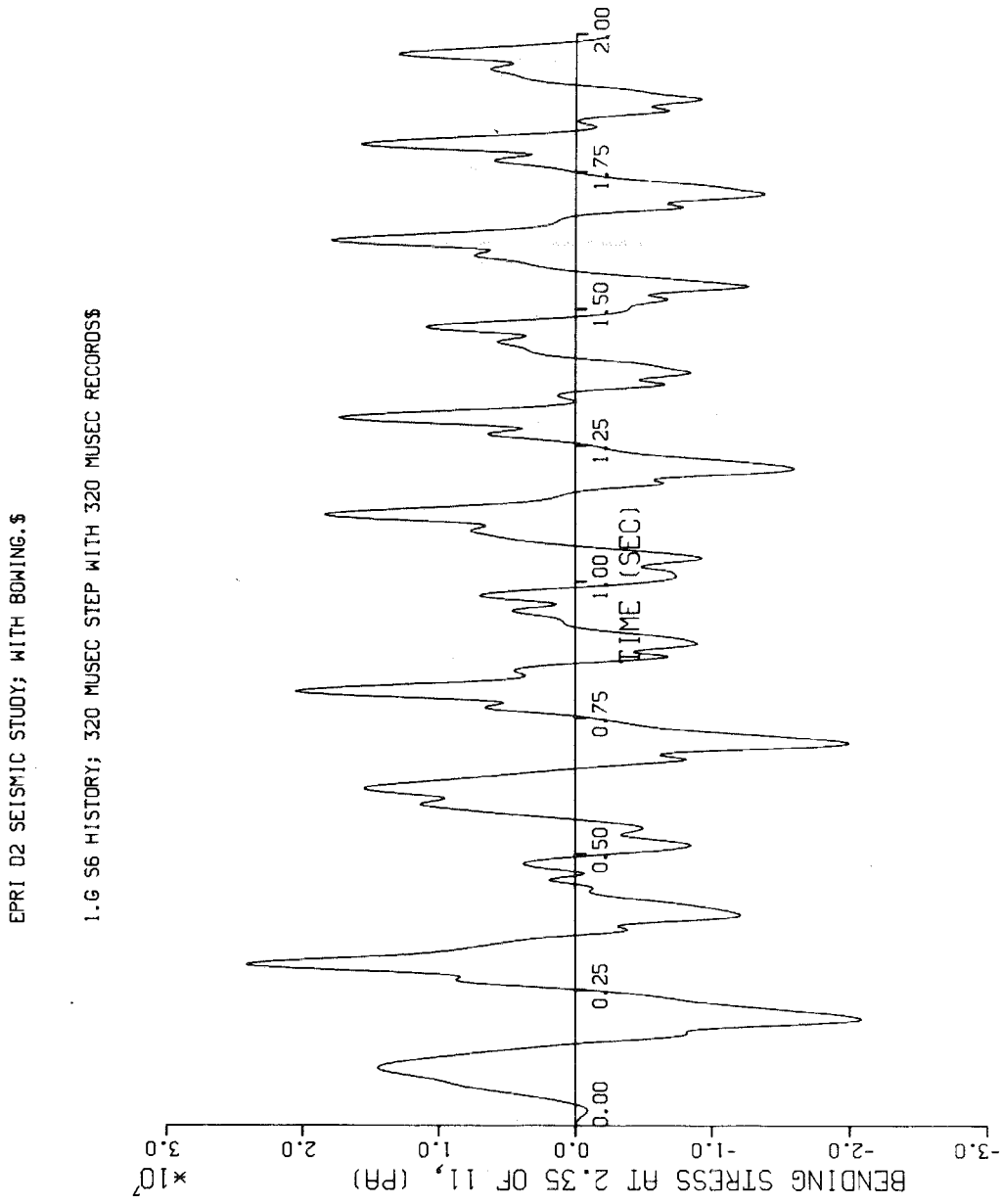

Fig. 3.34. Time History of the Bending Stresses at Mid-core for Cluster #11

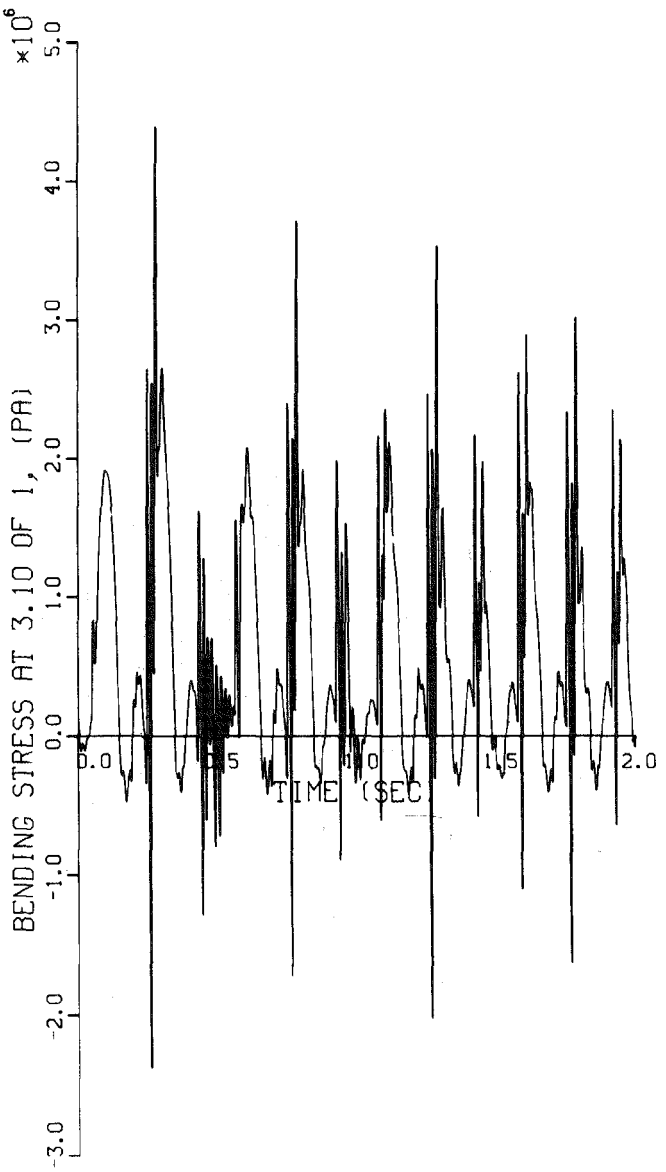

Fig. 3.35. Time History of the Bending Stresses at ACLP for Cluster #1

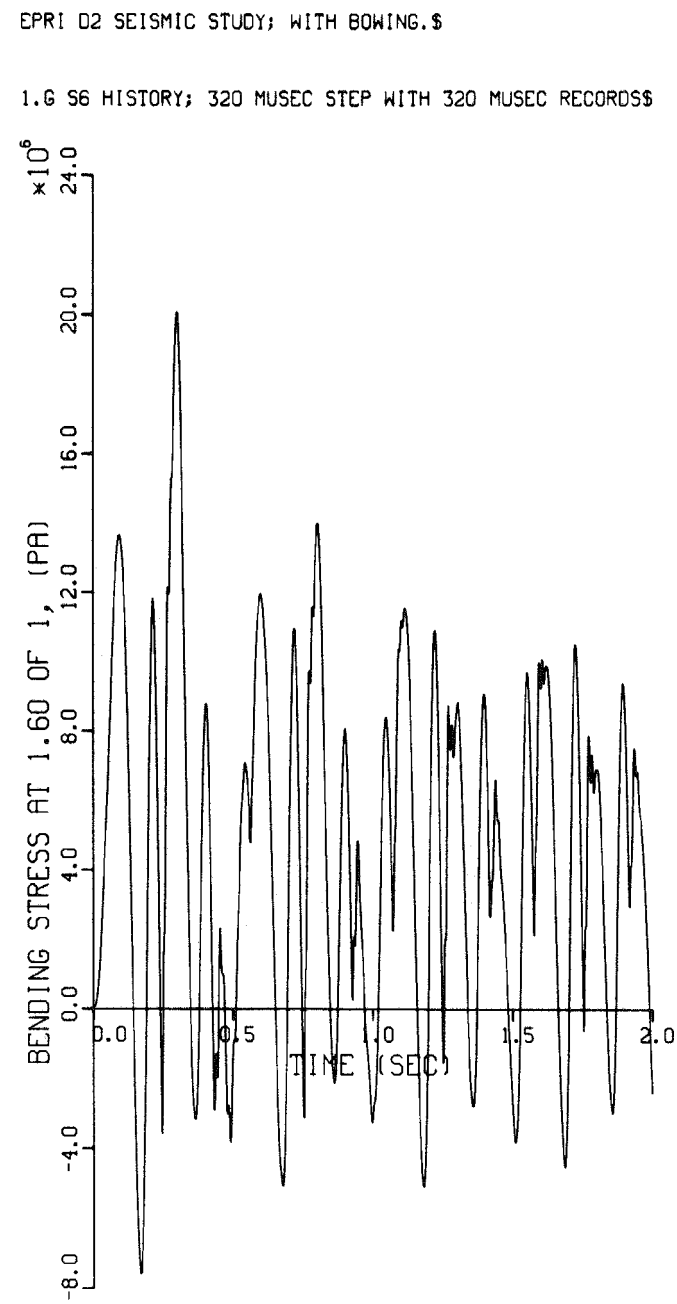

Fig. 3.36. Time History of the Bending Stresses at Lower Shield/Blanket Interface for Cluster #1

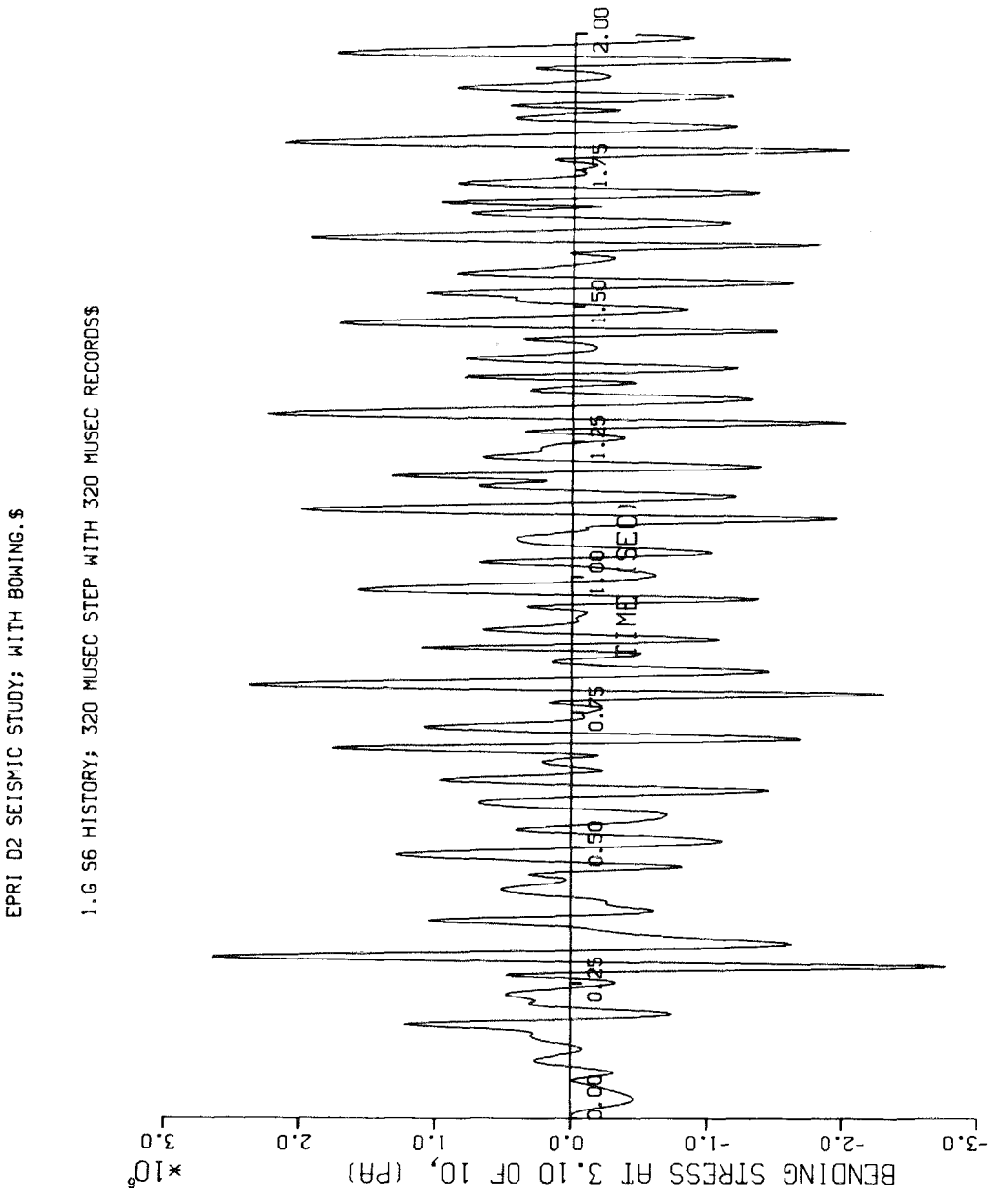

Fig. 3.37. Time History of the Bending Stresses at ACLP for Cluster #10

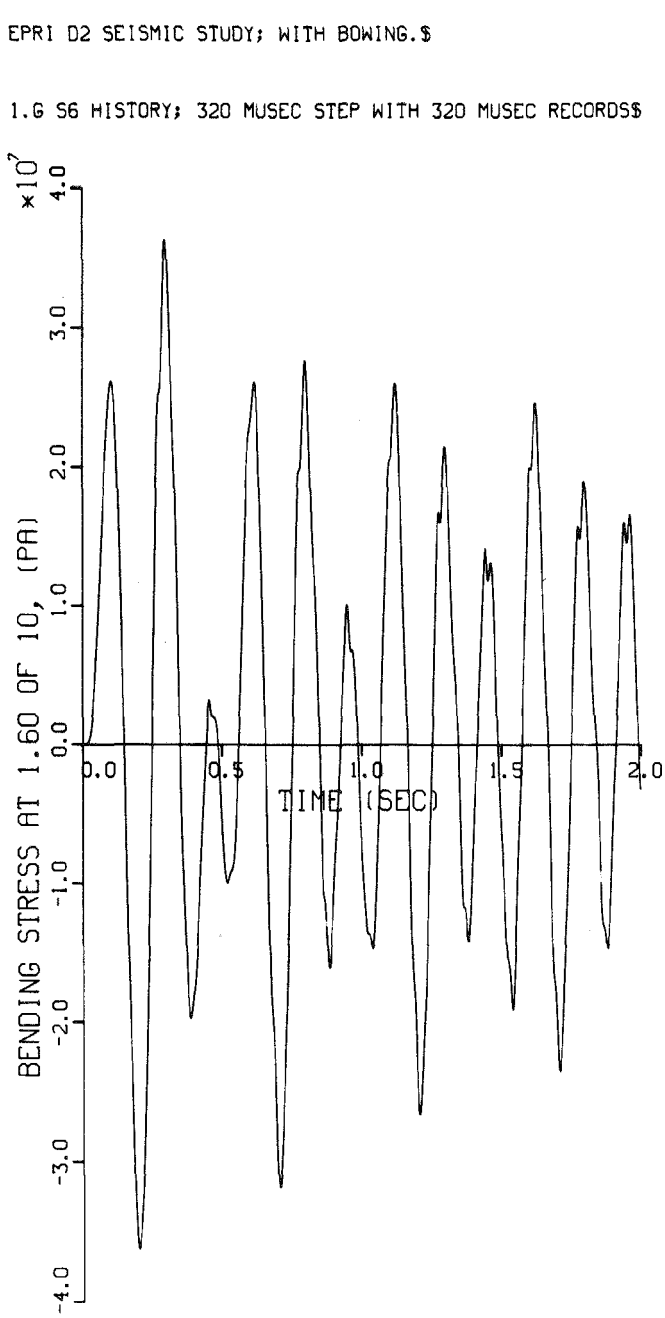

Fig. 3.38. Time History of the Bending Stresses at Lower Shield/Blanket Interface for Cluster #10

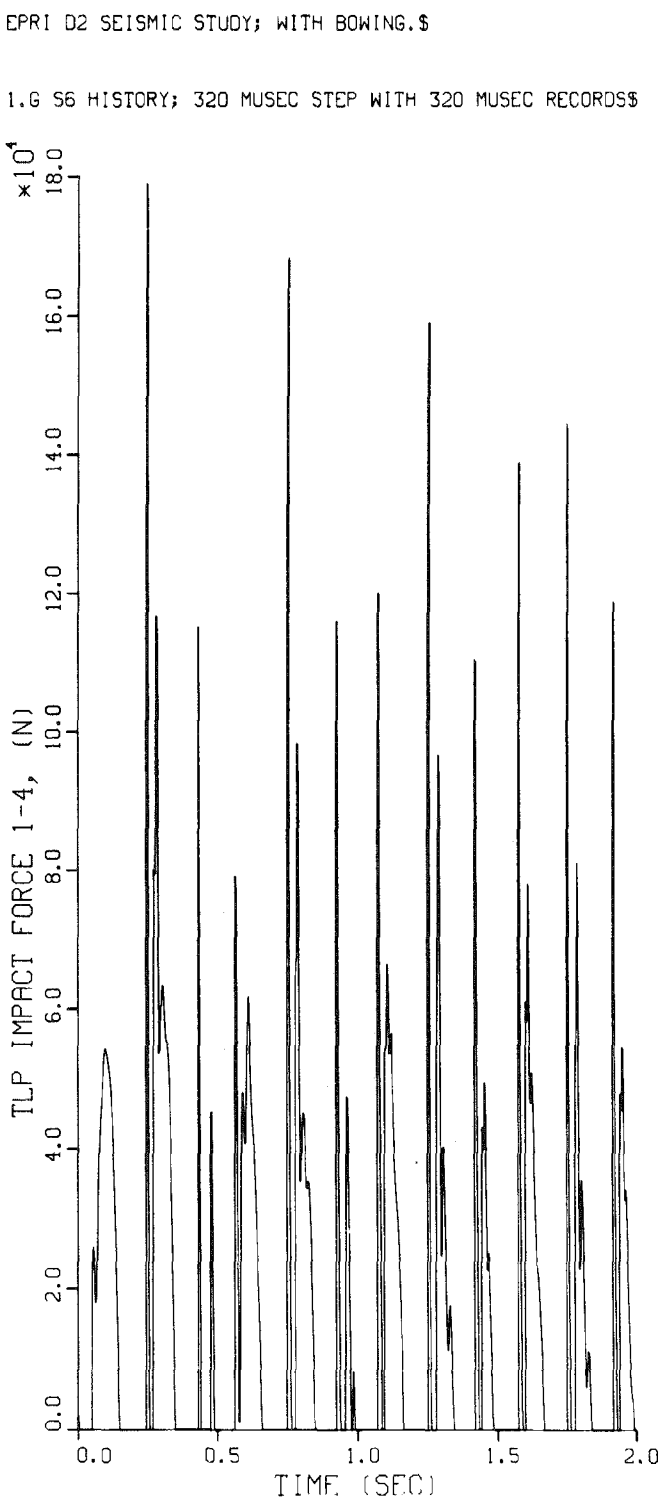

Fig. 3.39. Time History of Impact Force in the Direction of Support Motion Bewteen Clusters 1 and 4 at the TLP for 7 Faces

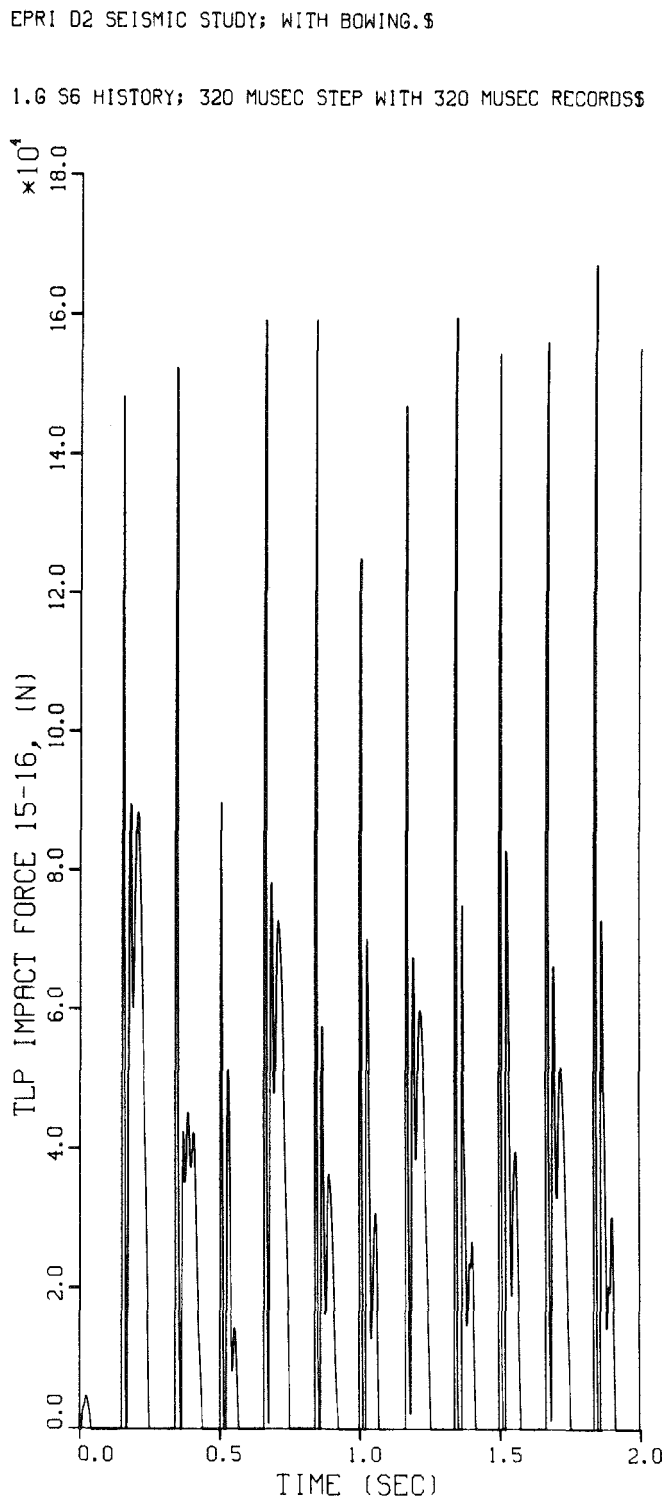

Fig. 3.40. Time History of Impact Force in the Direction of Support Motion Between Clusters 15 and 16 at TLP for 7 Faces

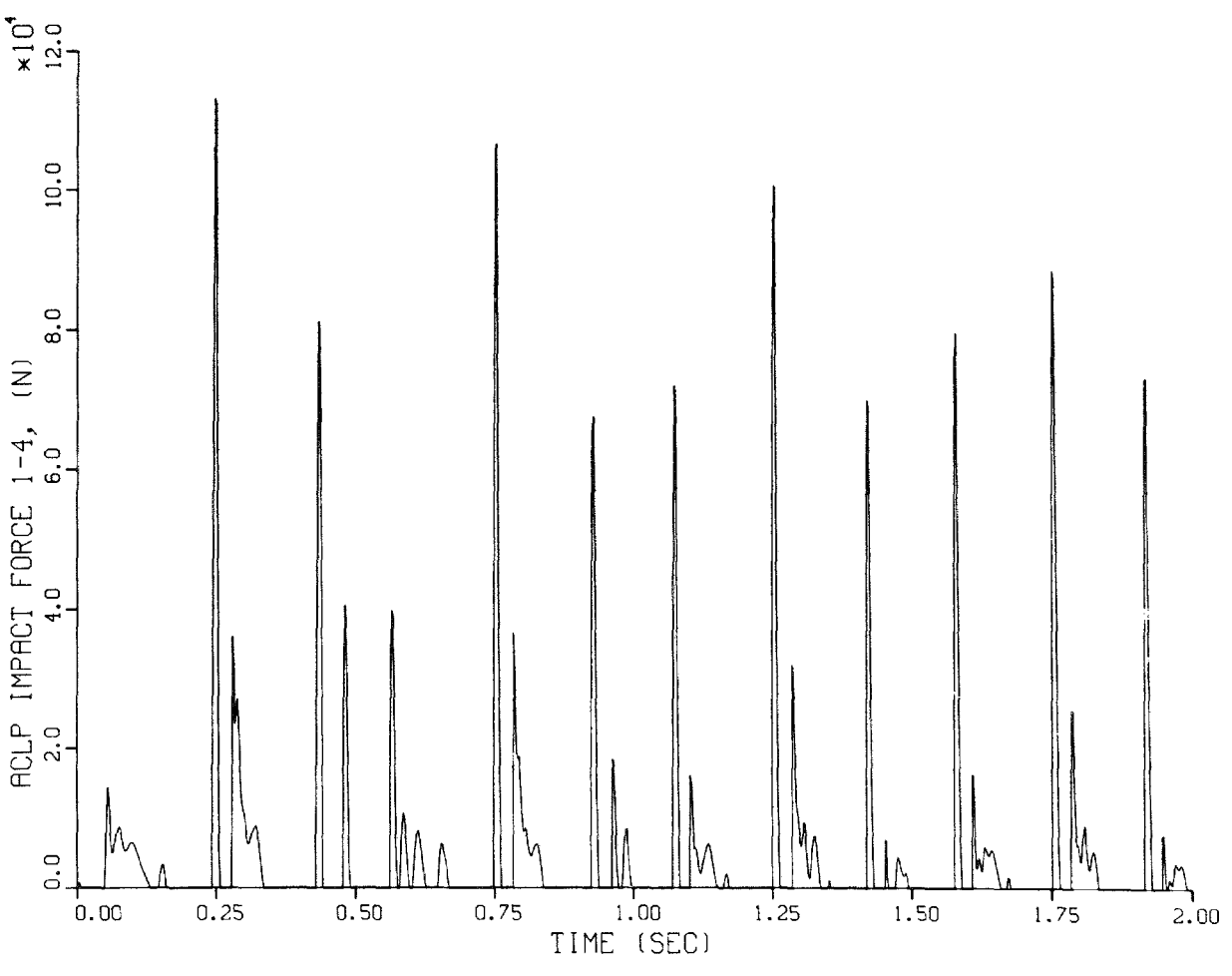

Fig. 3.41. Time History of Impact Force in the Direction of Support Motion Between Clusters 1 and 4 at the ACLP for 7 Faces

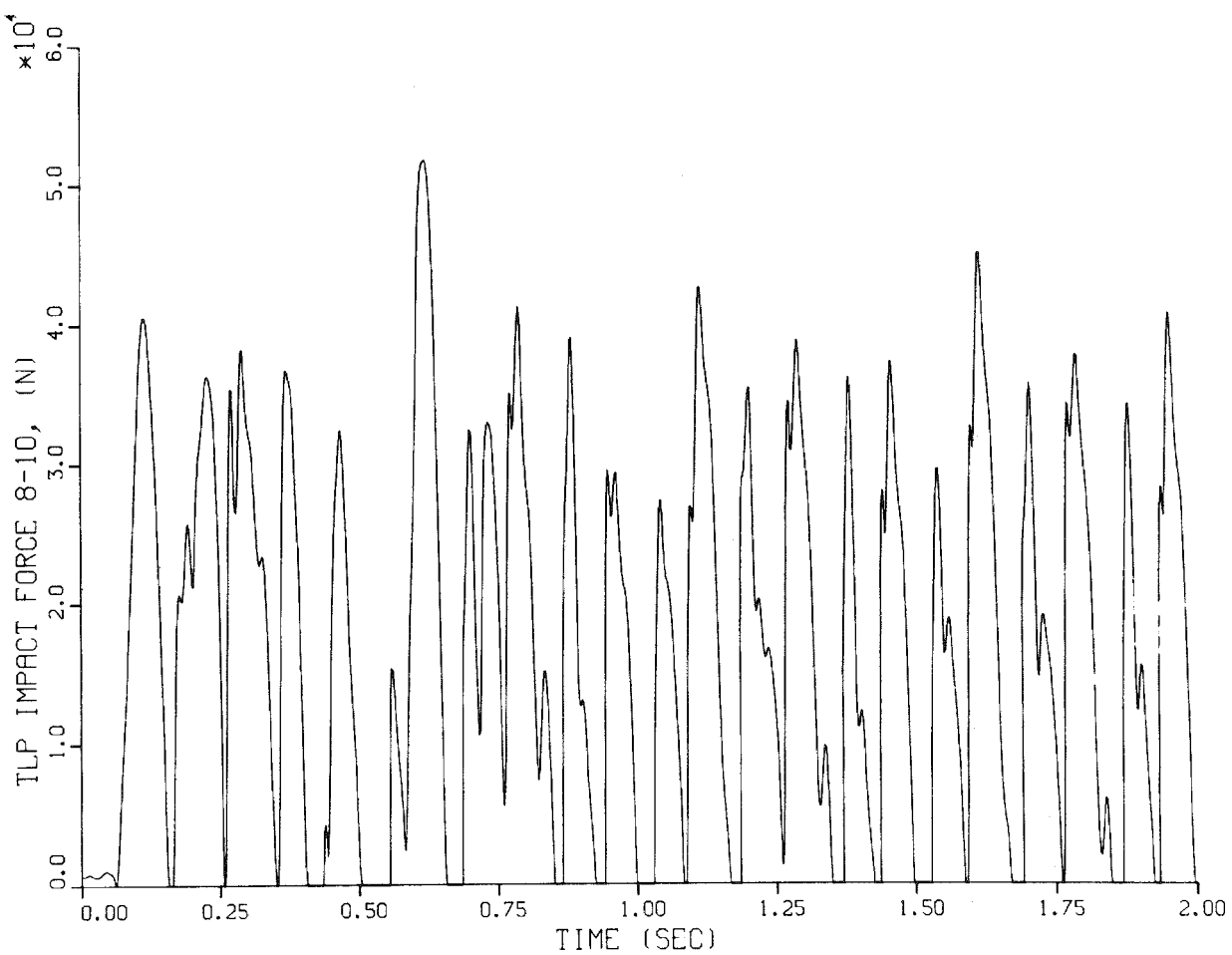

Fig. 3.42. Time History of Impact Force in the Direction of Support Motion Between Clusters 8 and 10 at the TLP for 5 Faces

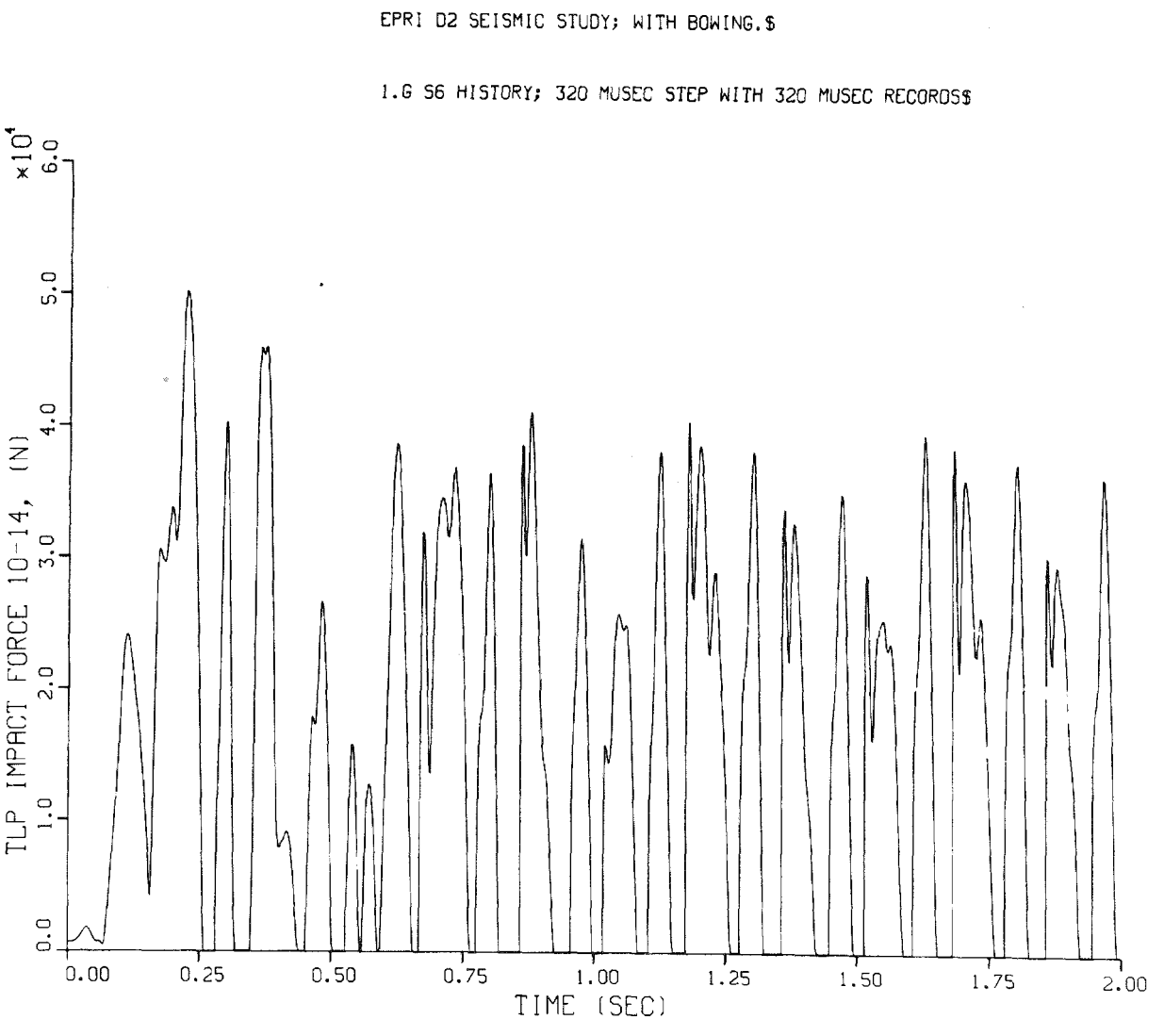

Fig. 3.43. Time History of Impact Force in the Direction of Support Motion Between Clusters 10 and 14 at the TLP for 5 Faces

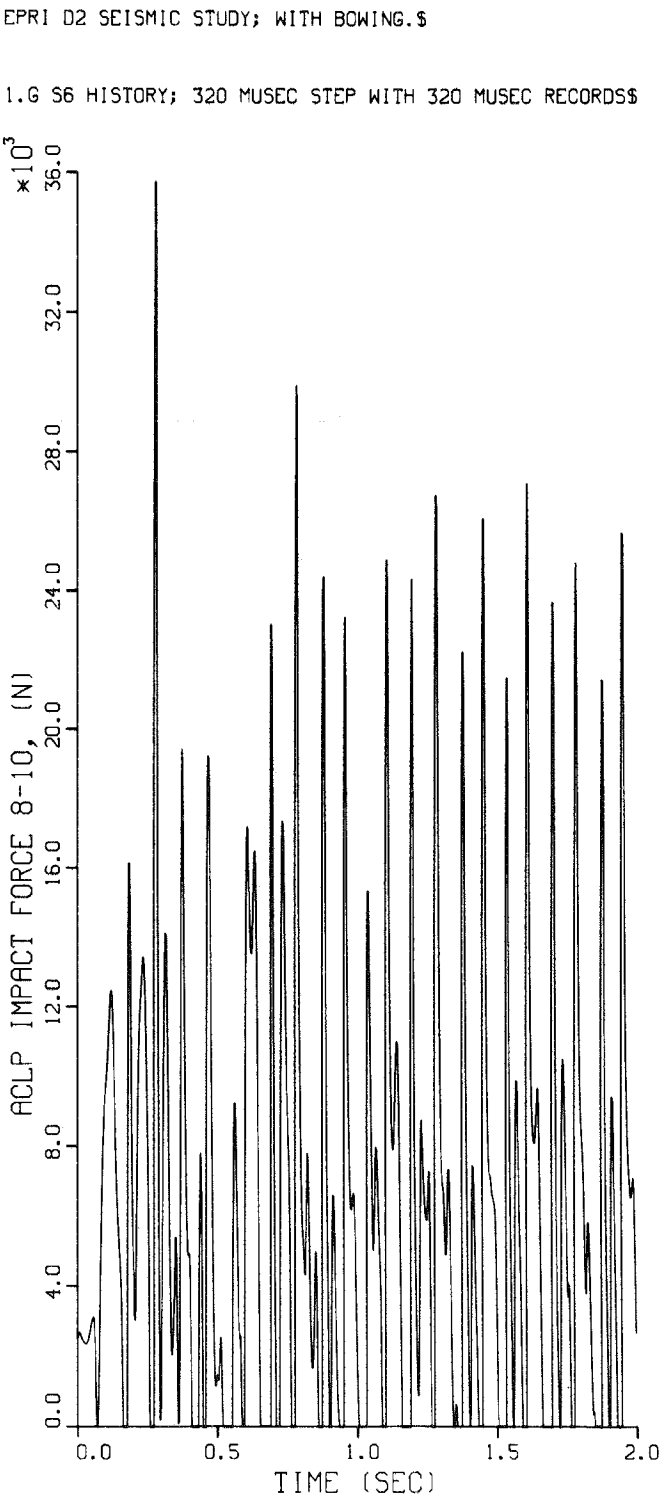

Fig. 3.44. Time History of Impact Force in the Direction of Support Motion Between Clusters 8 and 10 at the ACLP for 5 Faces

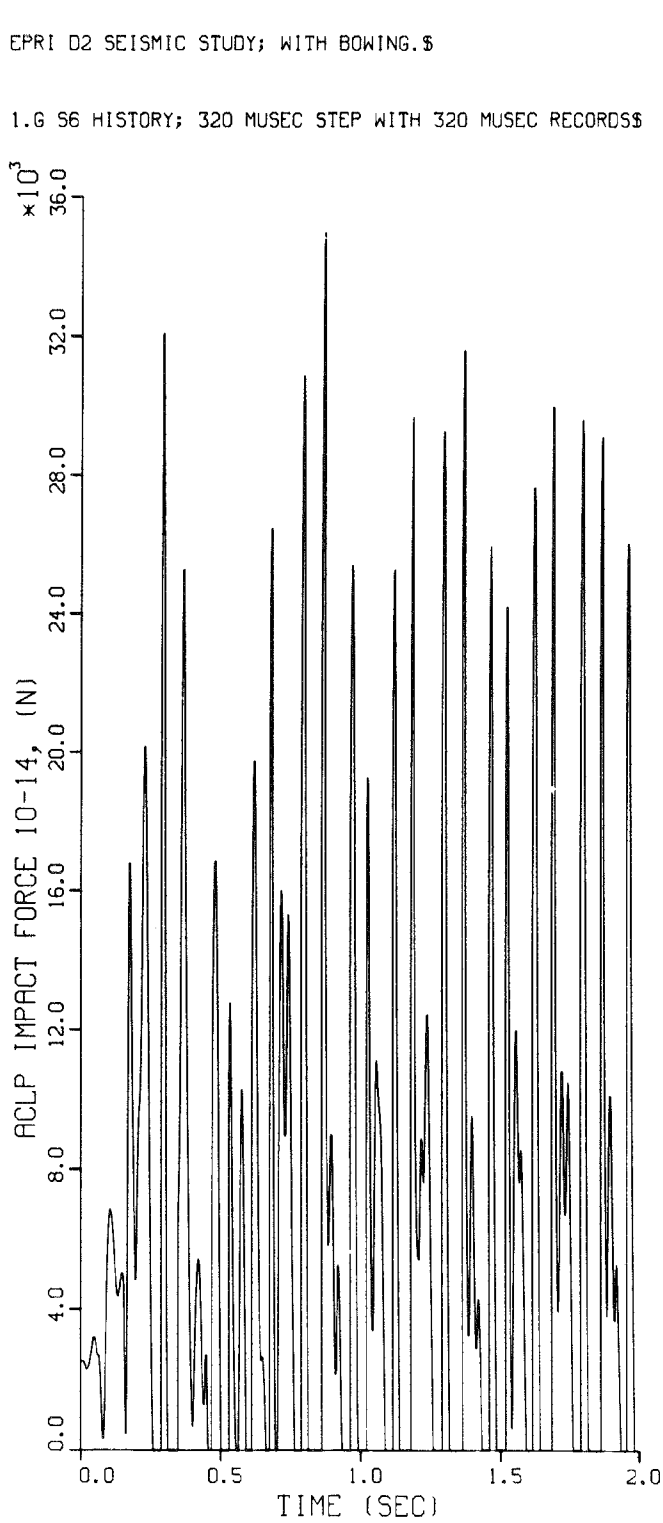

Fig. 3.45. Time History of Impact Force in the Direction of Support Motion Between Clusters 10 and 14 at the ACLP for 5 Faces

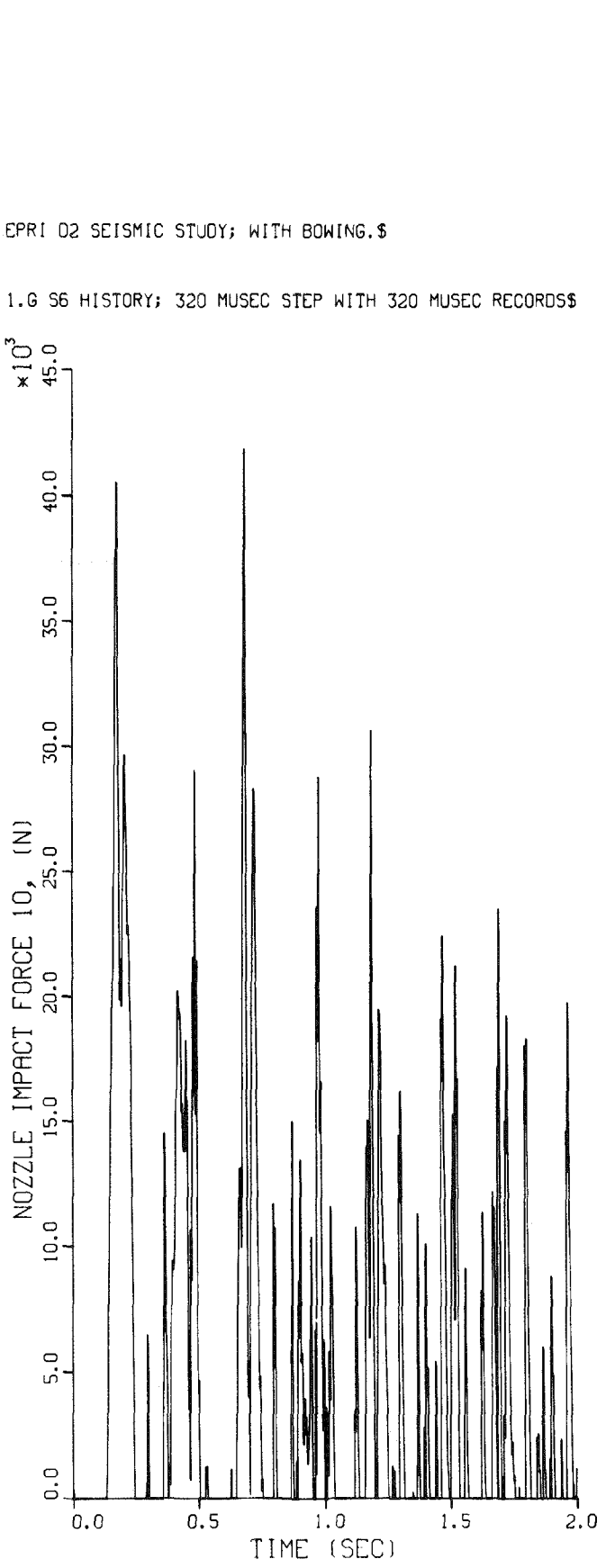

Fig. 3.46. Time History of Impact Force Between the Nozzle and Support Plate for Cluster #10 in the Direction of Cluster #1 for 19 Nozzles

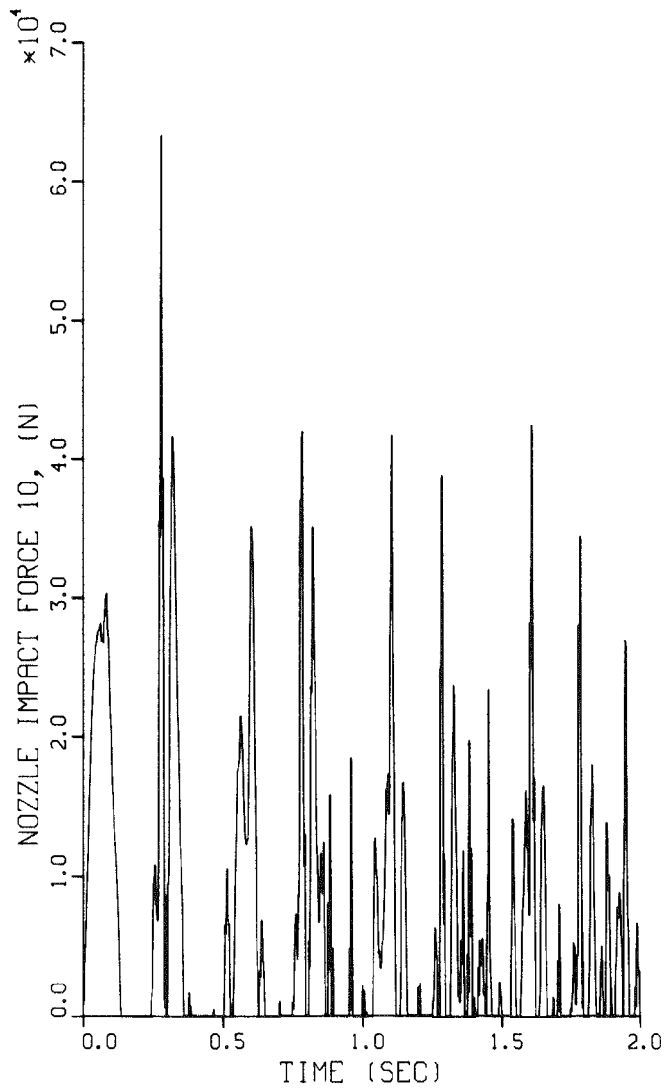

Fig. 3.47. Time History of Impact Force Between the Nozzle and Support Plate for Cluster #10 in the Direction of Cluster #16 for 19 Nozzles

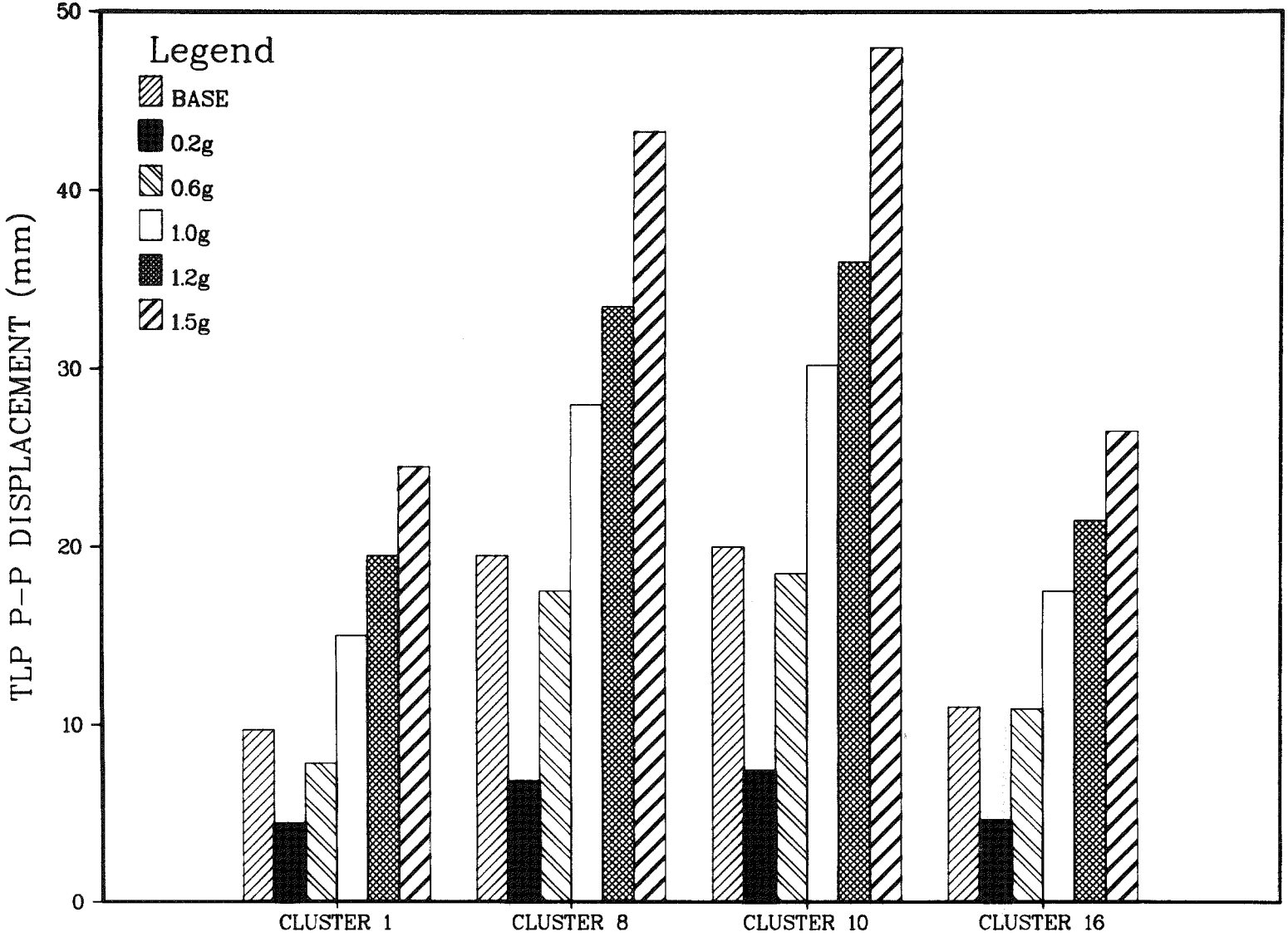

Fig. 3.48 Support Motion Amplitude Dependence of TLP Maximum Peak to Peak Displacement for Four Clusters

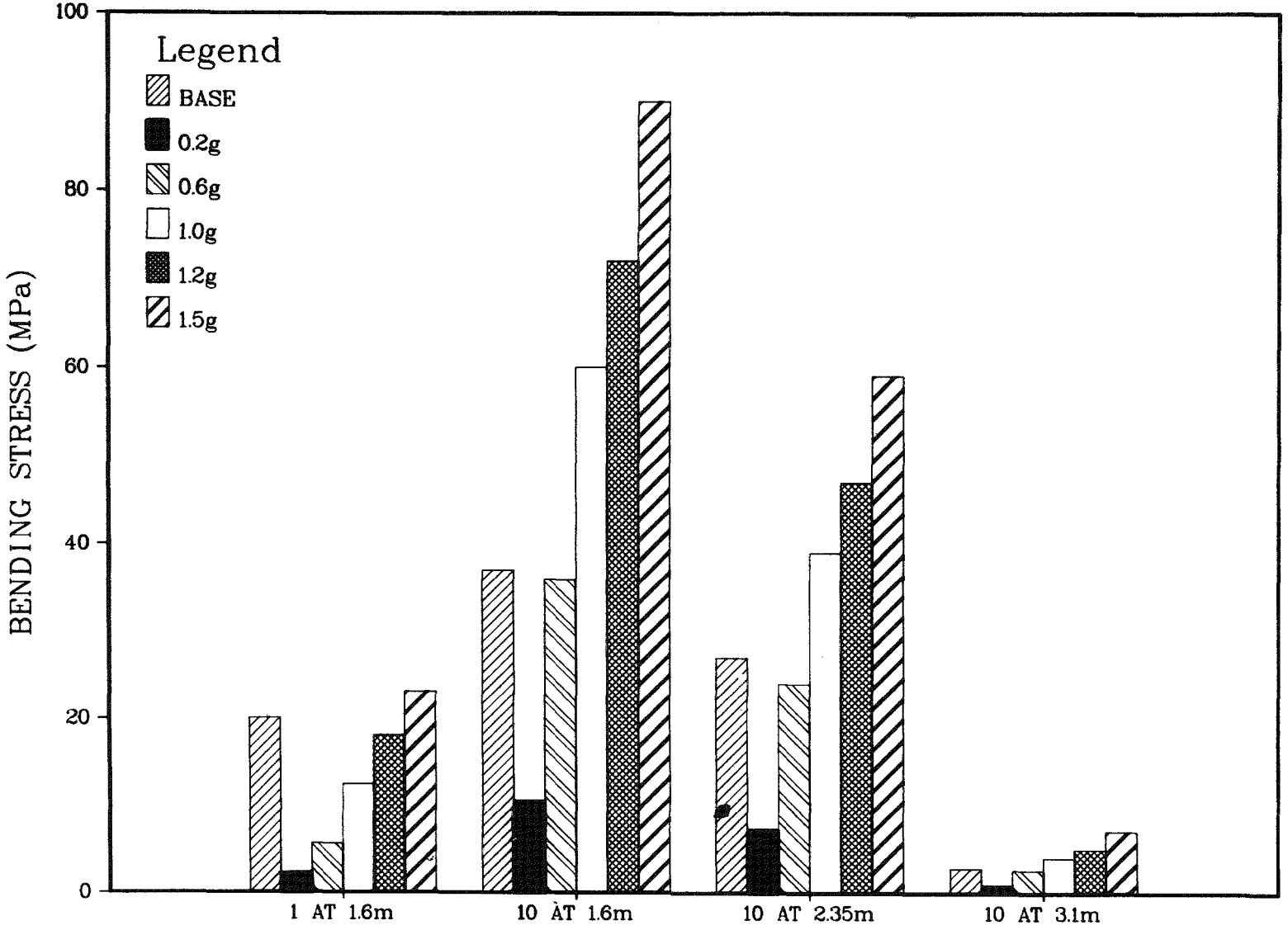

Fig. 3.49. Support Motion Amplitude Dependence of Peak Bending Stress at Mid-core for Four Clusters

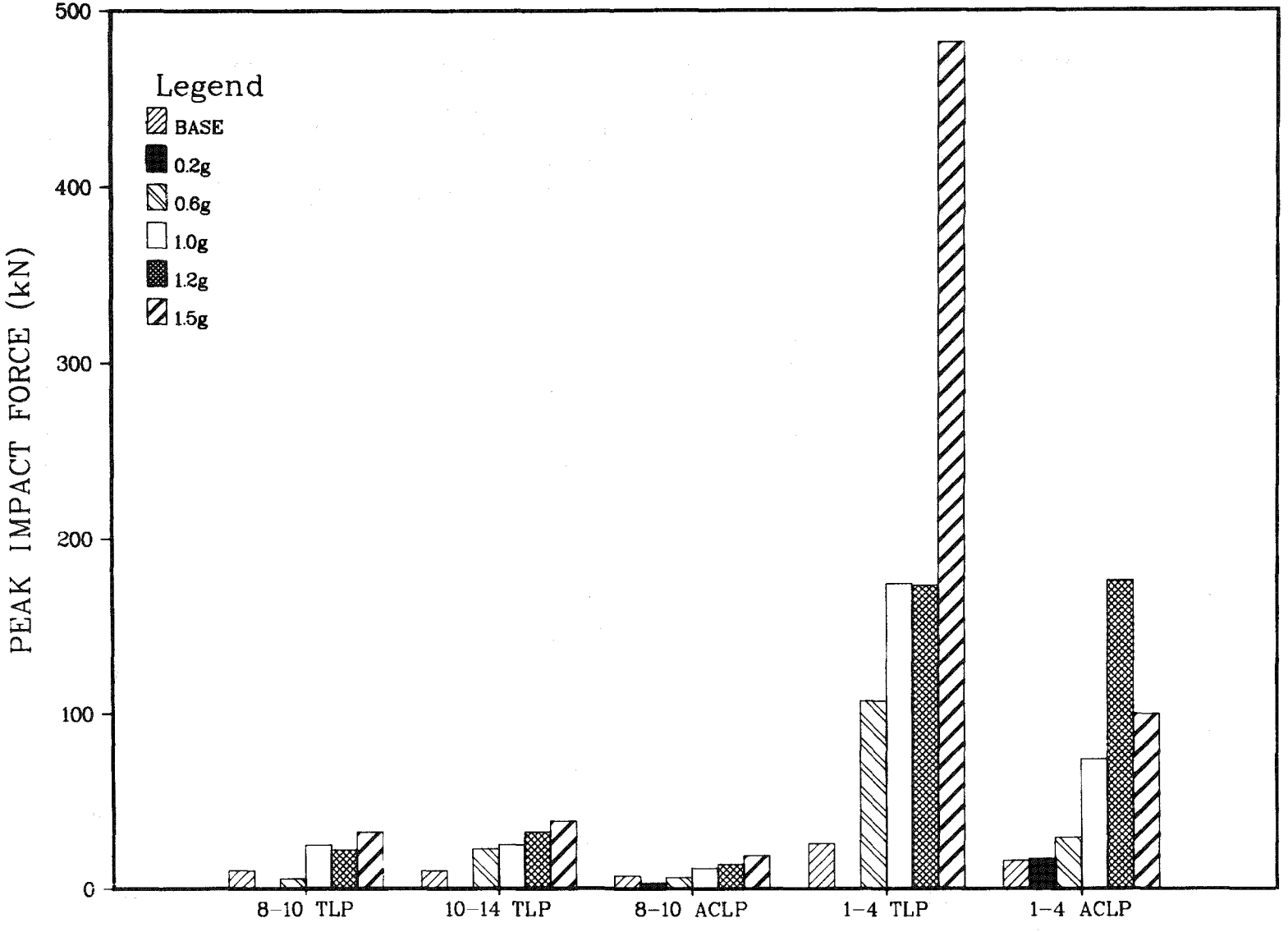

Fig. 3.50. Support Motion Amplitude Dependence of Peak Impact Force in the Support Motion Direction at Five Locations

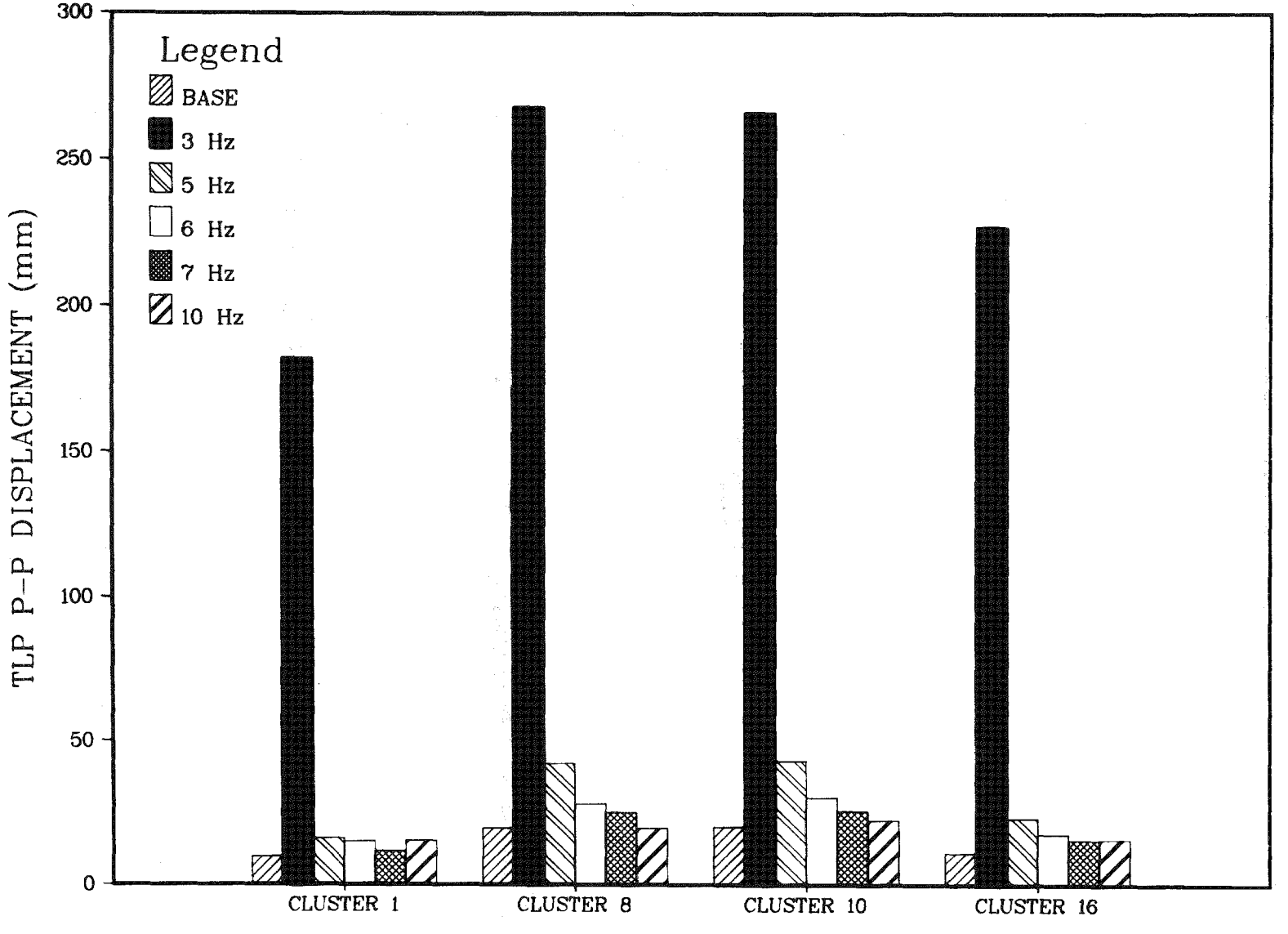

Fig. 3.51. Support Motion Frequency Dependence of TLP Maximum Peak to Peak Displacement for Four Clusters

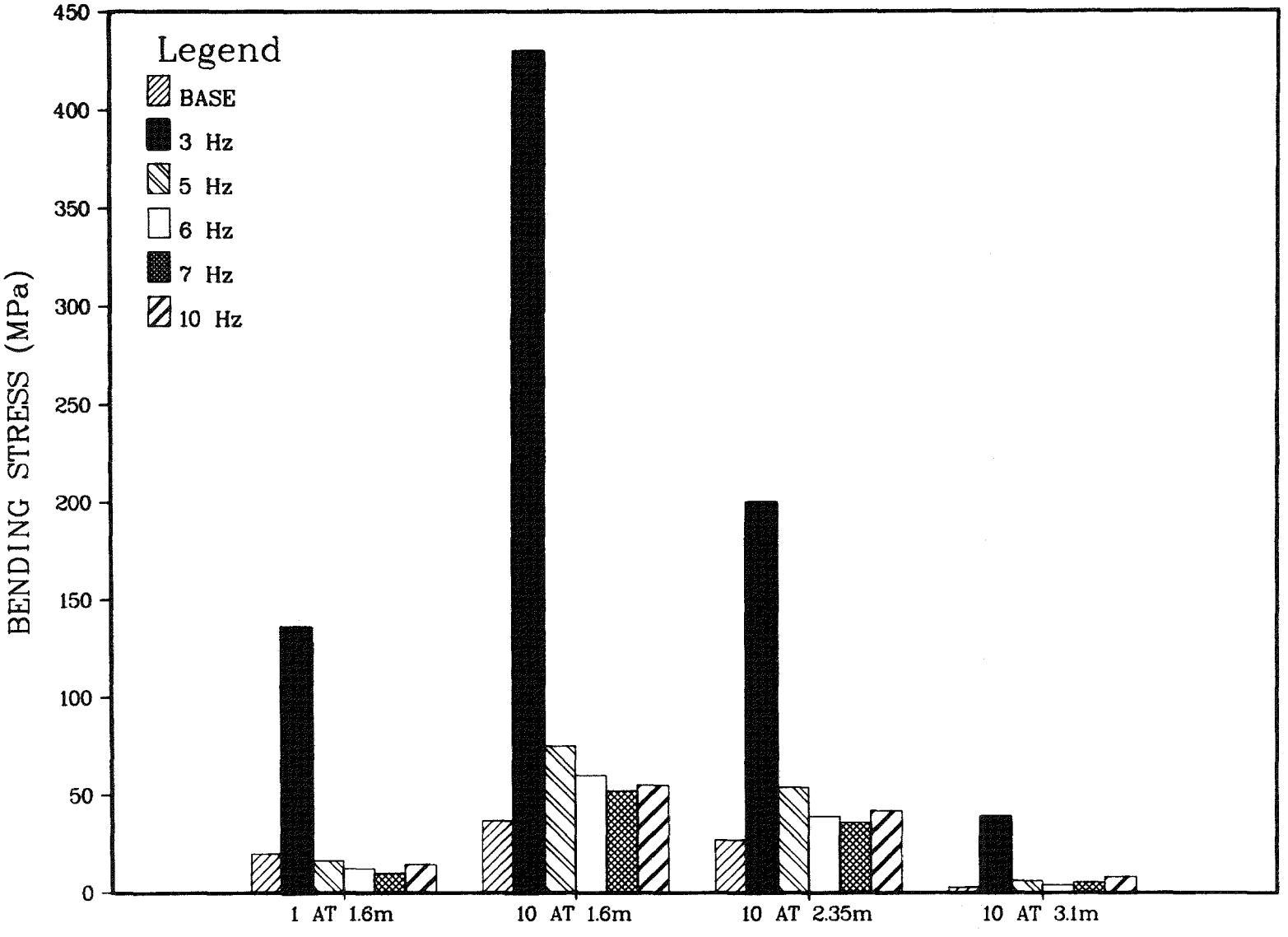

Fig. 3.52. Support Motion Frequency Dependence of Peak Bending Stress at Mid-core for Four Clusters

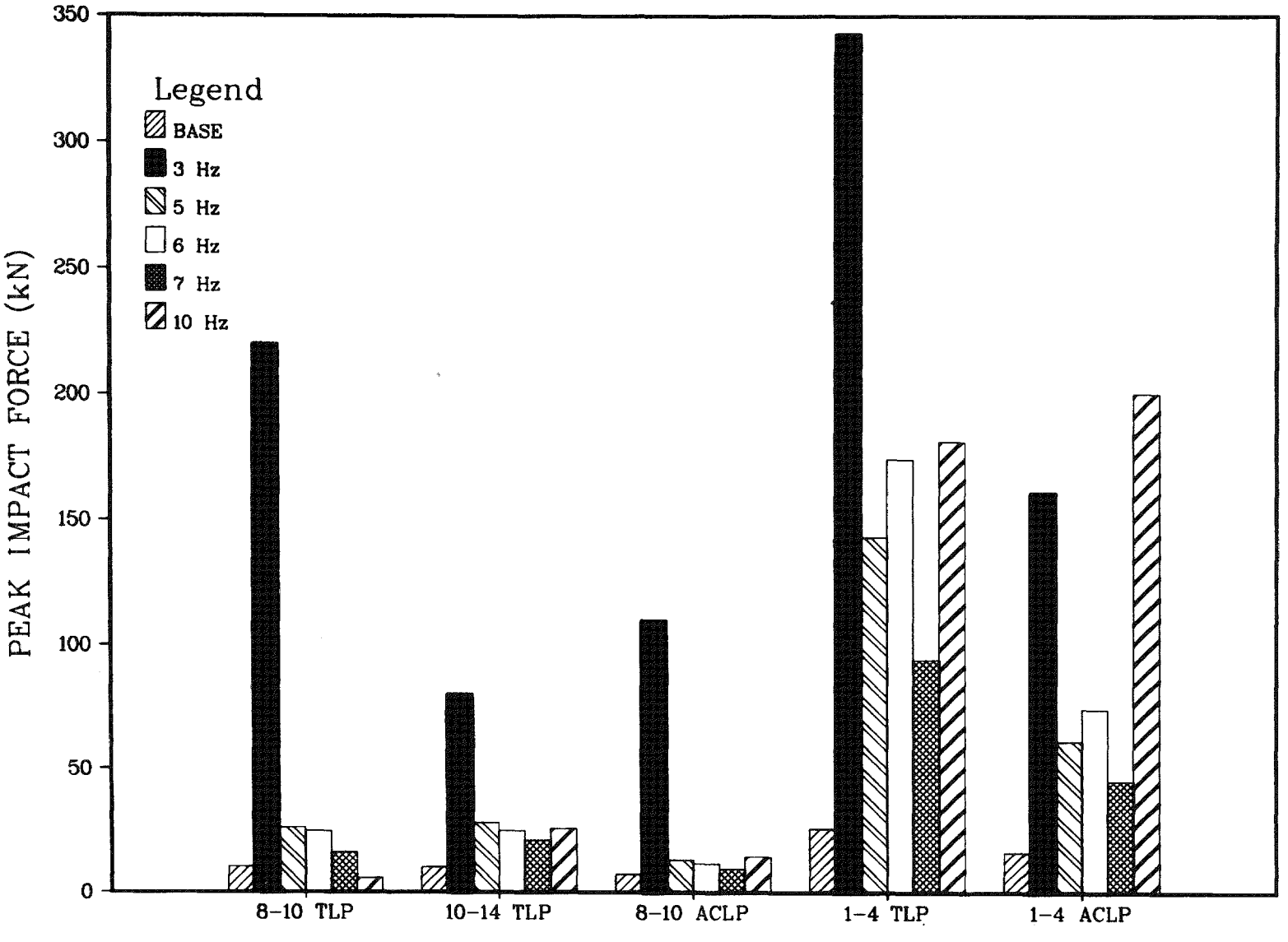

Fig. 3.53. Support Motion Frequency Dependence of Peak Impact Force in the Support Motion Direction at Five Locations

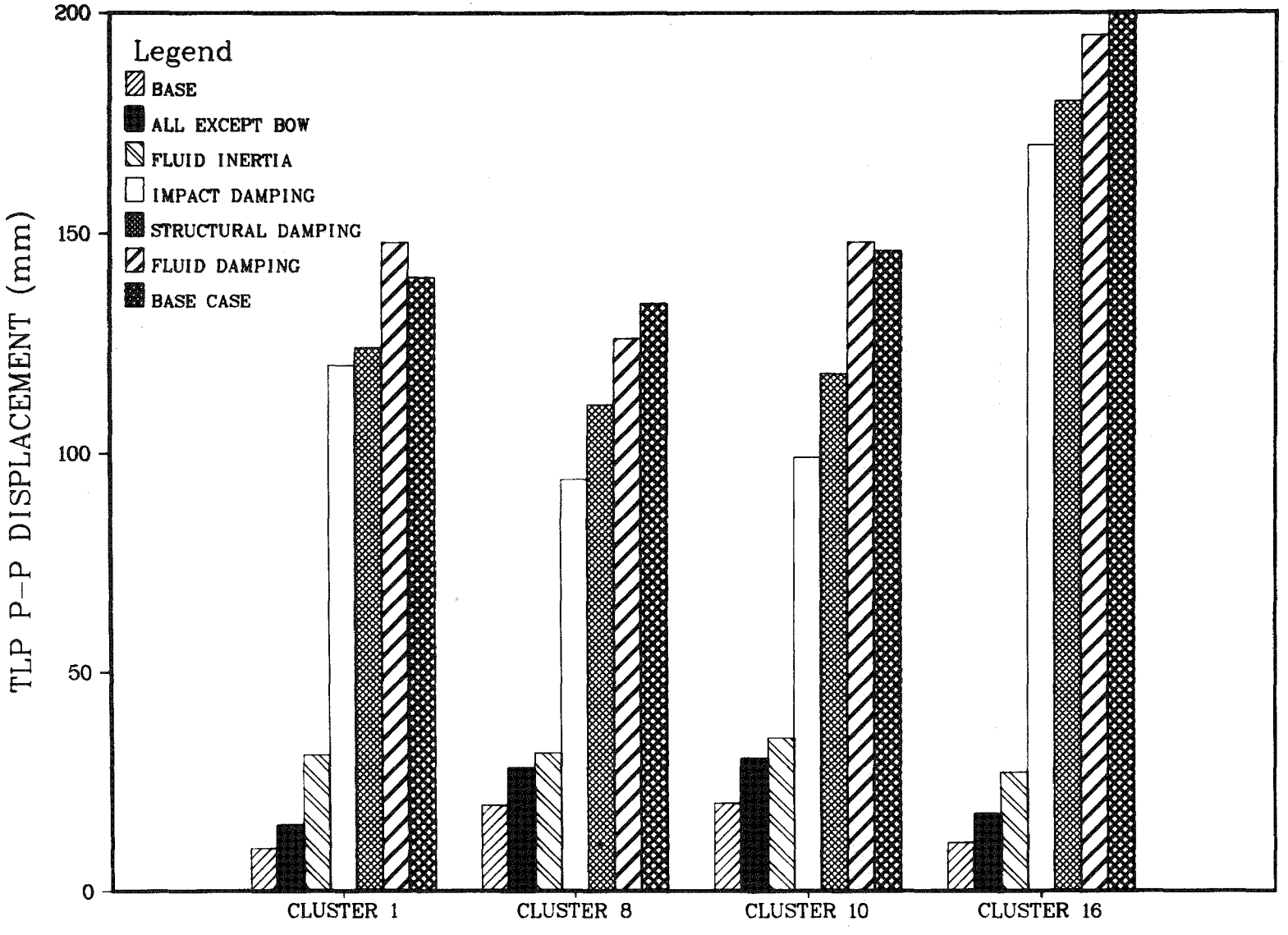

Fig. 3.54. Model Dependence of TLP Maximum Peak to Peak Displacement for Four Clusters

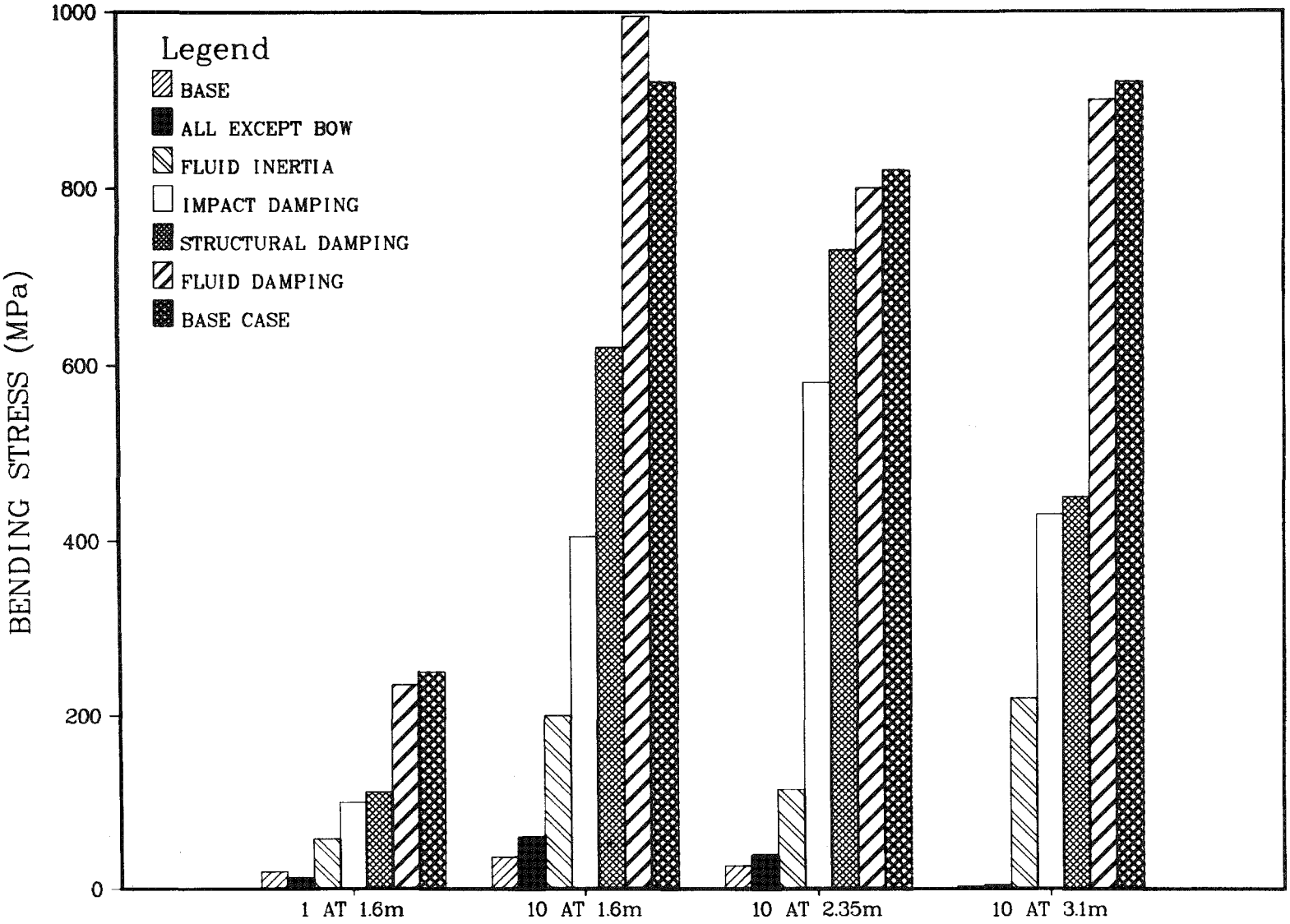

Fig. 3.55. Model Dependence of Peak Bending Stress at Mid-core for Four Clusters

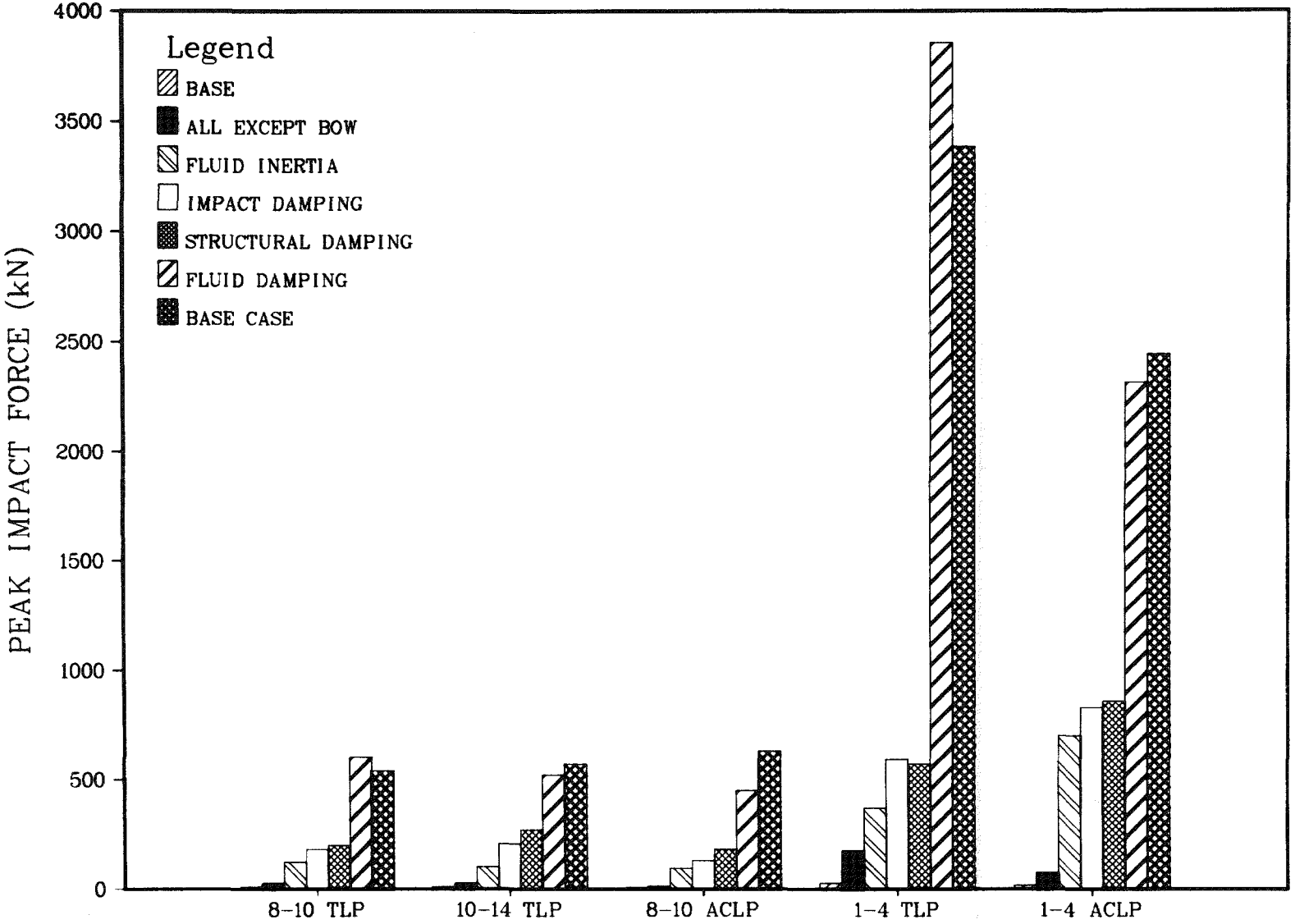

Fig. 3.56 Model Dependence of Peak Impact Force in the Support Motion Direction at Five Locations

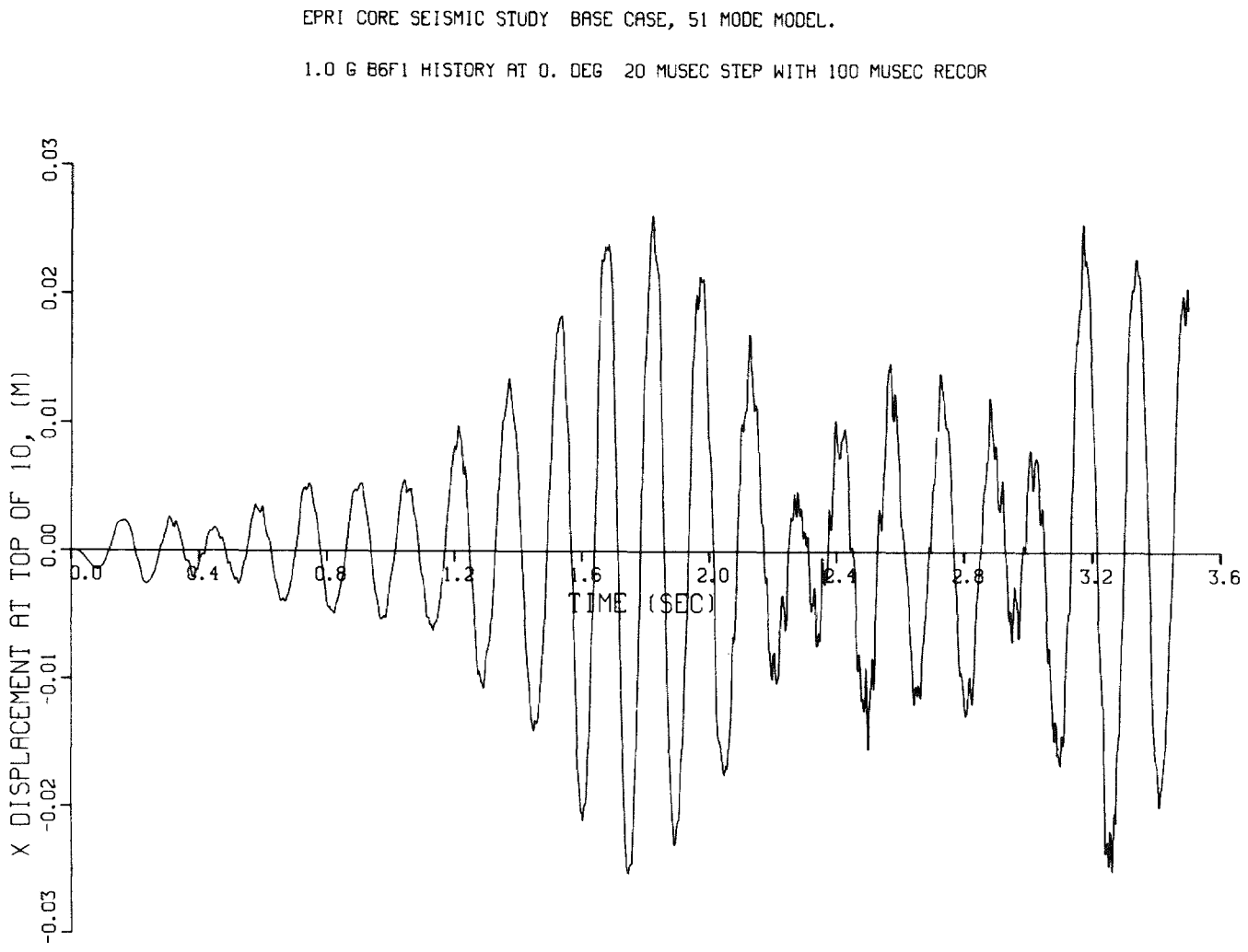

Fig. 3.57. TLP Displacement History for Design D-1 Subject to Narrow Band Support Motion (Fig. 3.4)

4.0 REFERENCES

1. B. K. Cha, P. J. Fulford, P. R. Huebotter, J. T. Madell and G. A. McLennan, "Conceptual Design Study of an Advanced Core Restraint System," ANL-CT-76-52, (August 1976).

2. J. F. de Paz and J. T. Madell, "Core Restraint Performance of Large Heterogeneous Reference Core," ANL-AFP-37, (June 1977).

3. "Conceptual Design of a 1000 MWe Heterogeneous Oxide LMFBR" (DRAFT), Science Applications, Inc., (May 1980).

4. G. A. McLennan, "NUBOW-3D (Inelastic): A FORTRAN Program for the Static Three-Dimensional Structural Analysis of Bowed Reactor Cores Including the Effects of Irradiation Creep and Swelling," ANL-CT-78-19, (March 1978).

5. "CRBRP Core Restraint System - Implementation of Design Requirements," WARD-D-0180, (July 1979).

6. Private Communication, W. P. Barthold (SAI), January 1980.

7. D. Paloms and J. Savary, "Control Rod Mechanisms for Fast Reactors," ANL-TRANS-1029, (July 1975).

8. T. J. Moran, "SCRAP - Theory and Modeling Considerations," ANL-CT-79-49, (July 1979)

9. T. J. Moran, "SCRAP - Input, Output, and Source Listings," ANL-CT-79-48, (July 1979)

10. C-I. Yang and T. J. Moran, "Calculations of Added Mass and Damping Coefficients for Hexagonal Cyclinders in a Confined Viscous Fluid," Flow Induced Vibrations, ASME, New York, (June 1979).

11. W. P. Barthold and C. P. Tzanos, "Conceptual Design of A 1000 MWE Heterogeneous Oxide LMFBR" EPRI NP-1616.

12. E. Hutter and R. V. Batch, "Hardware Concepts for a Large Low-Energetics LMFBR Core", EPRI NP-1617.

Appendix A

IRRADIATION CREEP AND SWELLING CORRELATIONS

The irradiation induced creep and swelling correlations used in the analysis were based upon PRLCDS projected properties for improved 316 stainless steel. The correlations were taken from Appendix I.B of the "Ground Rules and Criteria for the Conceptual Design Study, Task 1.0, Proliferation Resistant Fuel Cycles".

The Creep Correlation

The creep strain rate $\dot{\varepsilon}$ is assumed to be proportional to the stress σ and the flux ϕ.

$$\dot{\varepsilon} = C(T,\phi t)\ \sigma\phi$$

The coefficient C of proportionality depends upon the temperature T, and irradition history measured by the accumulated fluence ϕt at time t, and is given by

$$C = \left(\Lambda/\tau_{tr}\right) \exp\left(-\phi t/\tau_{tr}\right) + DRG + B_o$$

where R is a function of temperature (°C)

$$R = 7\times10^{-25} \exp(.0419 + 1.498\Delta + .122\Delta^2 - .332\Delta^3 - .441\Delta^4)$$

where

$$\Delta = (T-500)/T$$

Also, G is a function of the fluence (n/cm^2)

$$G = 1 - \exp(-\phi t/\Omega)$$

The neutron flux ϕ has dimensions (n/cm^2-sec).

The constants have the following values,

$$\Lambda = 10^{-8}\ (psi^{-1})$$

$$\tau_{tr} = 0.2 \times 10^{22} \ (n/cm^2)$$

$$D = 2 \times 10^{-5} \ (psi^{-1})$$

$$B_o = 3 \times 10^{-30} \ (psi^{-1} \ cm^2/n)$$

Also,

$$\Omega = 0.753 \ \tau$$

where

$$\tau = 9 \times 10^{22} \ (n/cm^2)$$

The total creep strain is obtained by integration at constant stress and flux

$$\varepsilon = \sigma\phi \int_0^1 C(T,\phi t) \ dt$$

so that

$$\varepsilon/\sigma = A \left[1-\exp\left(-\phi t/\tau_{tr}\right)\right] + \left[DR \ (1 - \Omega G/\phi t) + B_o\right] \phi t$$

The Swelling Correlation

The stress-free swelling, or fractional volume change is

$$S_o = (v - v_o)/v_o$$

where v is the swelled volume from some initial state v_o. A fractional density change is defined as

$$S = -\left(\rho - \rho_o\right)/\rho_o$$

where ρ is a density. Hence, if v is a specific volume, then

$$S_o = S/(1 - S)$$

The correlation for S used in the analysis was

$$S = 0.01 \ R \ \left[\phi t + \alpha^{-1} \ \ln\left(\frac{1 + \exp(\alpha(\tau-\phi t))}{1 + \exp(\alpha\tau)}\right)\right]$$

where

$$\alpha = 0.75 \times 10^{-22} \ (cm^2/n)$$